Microcavities for atom chips

Michael Trupke

Thesis submitted in partial fulfilment of the requirements for the degree of Doctor of Philosophy of the University of London and the Diploma of Membership of Imperial College.

Imperial College London

University of London

October 2007

Abstract

Microcavities for atom chips

Michael Trupke

This thesis describes the development and implementation of fibre-coupled, micron-scale optical resonators for the detection and manipulation of neutral atoms. The resonators are intended for integration with atom chips. The latter are micro-fabricated devices which enable the cooling, trapping, guiding and manipulation of atoms by means of optical, magnetic and electric fields. The fields are generated in part using micro-fabricated features on the surface of the chips. Optical cavities are among the most important tools in the study of the interactions between light and matter. They allow the observation of fundamental processes in quantum optics, based on the enhanced coupling of atomic transitions to light fields. Our resonators have mode volumes which are two orders of magnitude smaller than those used in typical cavity quantum electrodynamics experiments. Together with their high quality factors, this leads to large enhancement factors, rendering them ideal for the detection and manipulation of atoms on chips. They are scalable and directly fibre-coupled, both of which are qualities of interest for their implementation in quantum information-processing applications. In the thesis, the optical characteristics of the resonators are explained, as well as the basic principles of the interaction of atoms with their light field. The setup used for the test implementation of the devices is presented, together with early experimental results. These include the detection of atoms via their effect on the cavity reflection spectrum, and the detection of enhanced atomic fluorescence into the cavity mode. The thesis concludes with an outlook on further experimentation, possible improvements of the devices themselves, and a view on their integration with existing atom chip technology.

Contents

List of Figures

Chapter 1

Introduction

Three of the defining scientific and technological developments of our times meet on the stage set for this work: Quantum mechanics, silicon micro-fabrication and fibre-optic communications each play a lead role in the microcavities described herein. The bulk of the thesis is dedicated to the description of the optical properties of these microcavities, and to the interaction of atoms with their light field. This introduction is aimed at providing a brief overview of the context for the experiment within the fields of atomic physics and quantum optics. Many of the developments within these fields were made possible by the advent of laser-cooling, magnetic guiding and magneto-optical trapping, which are summarised in Section 1.3. It has since then been possible to miniaturise many experiments in these fields by performing them on micro-fabricated devices called atom chips (see Section 1.4.1). Their description leads into a motivation of the principal design choices made for the devices.

1.1 Context of the experiment

During the last three decades, the study of cold atoms has developed into one of the most active fields in theoretical and experimental physics. The interaction of atoms with light is both an indispensable tool and an area of rapid growth of this study. The most fundamental building block of this interaction is the coupling of an atomic transition between two quantum levels to a single, quantised mode of the electromagnetic field. The theoretical development of this interaction was initiated, as one of his many seminal contributions to modern physics, by Paul Dirac in 1927 [1]. That first seed soon brought one of the major successes of early quantum electrodynamics (QED), namely the correct derivation of the emission rate of an atom in free space by Wigner and Weisskopf in 1930 [2]. The "spontaneous" emission

rate was in fact shown to be stimulated by the vacuum: Weisskopf and Wigner derived it from the coupling of the atom to the 'empty' vacuum-field modes (i.e. modes devoid of excitation), thereby underpinning one of the most controversial aspects of the theory, namely the presence of a minimum energy in the modes of the electromagnetic field even in the absence of excitation. This energy emerges from the description of the modes as quantum simple harmonic oscillators and is proportional to the frequency of a given mode, $E(\omega) = \hbar\omega/2$ (see e.g. [3]).

To study the interaction of light and matter, it is desirable to analyse the simplest

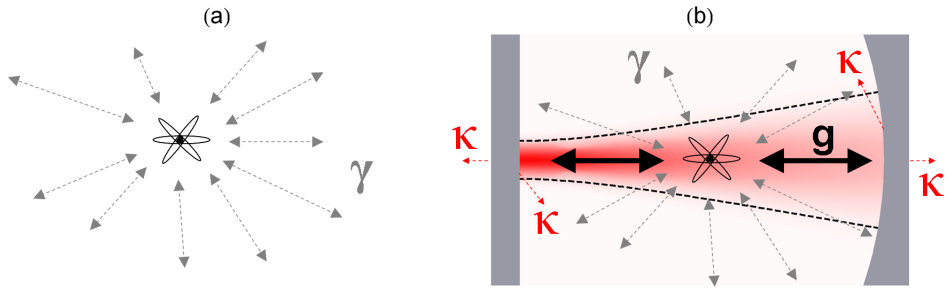

Figure 1.1: (a) an atom in free space will couple to all modes of the vacuum, leading to a decay γ of the excited-state population over time.(b) In a cavity, the atom can have a large coupling rate g to the mode of the resonator, and therefore interact strongly with it. The interaction will still be damped by free-space decay of the atom and by a decay κ due to losses from the cavity mode via transmission or scattering at the mirrors.

of all models mentioned above, namely the coupled system of one atom and one radiation mode. This is known as the Jaynes-Cummings model [4]. However, while conceptually simple, a number of challenges stand in the path between this ideal model and its experimental realisation. Firstly, as empty space itself is filled with vacuum radiation modes, it would be necessary to isolate the atom from these, and no technically feasible realisation for this approach has yet been found. What has however been achieved with enormous success is to enhance the coupling to one mode so strongly that all other modes become weak, even negligible, by comparison. This is known as the "strong-coupling"-regime, and has been approached or reached in many research groups using a variety of approaches. A comparison between an atom in free space and an atom coupled to a cavity mode is sketched in Figure 1.1. These include two-mirror (Fabry-Pérot type) resonators to which neutral atoms, Rydberg atoms or ions are coupled, whispering-gallery-mode resonators coupled to atoms or quantum dots, micropillar cavities with embedded quantum

dots, and microwave-stripline resonators (see, for example, [5, 6, 7] and references therein). All of these techniques have in common the confinement of the light mode to small volumes. This is motivated by the fact that the coupling rate g between an atom and a mode increases with the energy density in the mode, $g \propto \sqrt{E(\omega)/V}$. A large coupling rate is however only one of the requirements for strong coupling. The interaction between the atom and the light mode will still be damped, and therefore decreased, by the coupling of the atom to the modes of the vacuum. This is quantified by the atom's amplitude decay rate γ. Furthermore, the light will escape from the region to which it is confined, thereby ending the interaction with the atom. The light must therefore be confined for as long as possible by at least two mirrors, or by making it propagate on a closed path, as is done in whispering-gallery resonators [5]. In the case of two mirrors, the light can be lost by transmission, absorption or scattering at the mirrors. To achieve long damping times it is therefore desirable to implement smooth, high-reflectivity mirrors. The damping time $1/\kappa$ of the cavity field is defined as the time within which the amplitude of the field is expected to reach a fraction $1/e$ of its initial value.

To achieve interaction between atoms and the light field confined to the cavity, it is necessary in the first place to bring the atoms into the strong part of the resonator light field. In early experiments, this was achieved by directing a collimated beam of thermal atoms from an oven between the mirrors (see e.g. [8]). More recently, transport mechanisms have been successfully implemented which allow the controlled loading of atoms into the cavity using magnetic [9, 10, 11], optical [12] and electrostatic [13, 14] tools. Once the atoms are in the cavity, a number of astounding effects can be observed. Firstly, since the atomic decay rate depends on the coupling to the electromagnetic modes, this decay can be enhanced (as proposed by Purcell in 1947 [15]) or suppressed (as proposed by Kleppner in 1981 [16]) in the cavity. This is described in more detail in Chapter 5. Furthermore, the absorption of light by the atoms is also modified compared to free space, so that atoms can be detected and manipulated with far greater accuracy in a cavity. This has led to the real-time detection of single atoms [17] and the generation of single photons on demand [18]. The ability to count atoms is as such a very alluring prospect, as currently most atomic physics experiments rely on far less precise methods such as camera images to determine the size of a cloud of trapped atoms, for example. Single-atom detection is furthermore a prerequisite of many protocols in the much-hyped field of quantum computing, simulation and communications [19]. Some of these applications require the internal and motional states of the atoms to remain undisturbed by the detection process. This is indeed possible with microcavities

[20]. The possibility of generating single photons on demand is also based, in the more ubiquitous protocols (such as [18]) on the presence of a single atom in the cavity. It is possible to produce a non-local superposition of the internal states of two atoms in two cavities by performing measurements on the single photons they emit, or by detecting macroscopic signals from two atoms in one cavity [19]. This "entanglement" forms the basis of quantum computation (QC). Most QC protocols involving atoms in cavities require the accurate positioning of atoms in the field of the resonator. On atom chips, this is achieved by acting on the magnetic dipole of the atoms, as described below in Section 1.3. First though, a brief description of our atom of choice.

1.2 Rubidium

The discovery of Rubidium is commonly attributed to Robert Bunsen and Gustav Kirchoff, who encountered the element in 1861 during the course of a spectrographic study of the mineral lepidolite, from which it is still commercially extracted. It is the twenty-third most abundant element in the earth's crust. Rubidium has only one stable isotope, ^{85}Rb, with a natural abundance of 72.17 %. ^{87}Rb is the second most abundant isotope at 27.17 %. While it is radioactive, its half-life of 5×10^{11} years still gives ample time for atomic physics experiments to be performed. This isotope is also used in Rubidium-Strontium geological dating. ^{82}Rb is commonly used in cardiac tumor diagnosis, as its chemical similarity with Potassium guarantees that it will reach the cardiac muscular tissue rapidly. Its short half-life of 1.3 minutes ensures that long-term radiation exposure is avoided. These applications notwithstanding, Rubidium has arguably found its greatest prominence with atomic physics experiments. The reasons for its popularity in this field are easily stated: it is a hydrogen-like atom with only one free electron, giving it a simple level scheme (see Fig. 1.2). Its electronic transition frequencies are within reach of inexpensive diode laser systems. Because of its abundance, ^{85}Rb is often chosen over ^{87}Rb. However, when the experiment involves Bose-Einstein condensation, the negative scattering length of ^{85}Rb leads to the undesirable implosion of the cloud. ^{87}Rb, by contrast, has a positive scattering length and Bose-Einstein condensation was demonstrated, for the first time ever in a dilute atomic gas, with this isotope in 1995 [21]. A number of optical and magnetic cooling and trapping steps need to be implemented to achieve the necessary high densities and low temperatures needed to reach condensation.

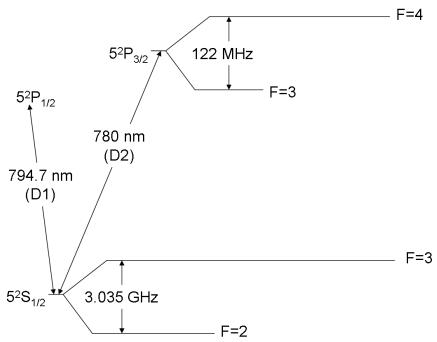

Figure 1.2: Scheme of the levels relevant for our experiment in Rubidium 85.

1.3 Magnetic and Optical potentials

1.3.1 Light forces

The force which acts upon atoms in the presence of a light field can be divided into two parts: the scattering force and the dipole force [22]. The dipole force is a conservative force proportional to the gradient of the intensity of the light field, and arises from stimulated scattering processes. Practical descriptions of this force can be found, with increasing depth, in the author's MSc report, reference [22] and reference [23]. The scattering force results from the exchange of momentum between the photons and the atoms during incoherent scattering. The magnitude of this force acting on a two-level atom is given by

$$\vec{F}_{scatt} = \hbar\vec{k}\gamma_{scatt} \text{ where } \gamma_{scatt} = \gamma\frac{I/I_{sat}}{1+((\Delta_{AL}-\vec{k}.\vec{v})/\gamma)^2+I/I_{sat}}. \tag{1.1}$$

Here $\vec{k}$ is the wavevector of the light, and $\Delta_{AL} = \omega_L - \omega_{eg}$ is the detuning of the light from the resonant frequency of the atomic transition. When the intensity I is much smaller than the saturation intensity I_{sat}, the scattering force increases linearly. In the limit of infinite intensity, the force saturates at $\vec{F}_{max} = \hbar\vec{k}\gamma$. The bracketed term in Eq. 1.1 indicates that the force will depend on the detuning and on the Doppler shift $-\vec{k}.\vec{v}$ of the light frequency perceived by a moving atom. This effect forms the basis of laser cooling. A spectrally narrow, red-detuned beam will appear resonant to an atom moving opposite to the light wavevector with the appropriate velocity. The momentum change of the atom during an absorption process in this setting will always be opposed to its direction of motion, while the emission process averages to zero. The net momentum change therefore leads to a deceleration of

the atom. However, once it has slowed down, the atom is no longer resonant with the light beam and scatters at a decreased rate. The atom is therefore cooled in that direction. Applying red-detuned laser beams from six directions, i.e. from both directions on three orthogonal axes in space, leads to cooling in all directions. This setting is known as '3D-optical molasses'. In this configuration, the atoms are cooled along all three axes. The scattering processes, though rare, do not fully cease: An atom close to rest will still experience random momentum jolts as it scatters light from any of the beams. While the atoms in 3D-molasses are cooled, they are not trapped because the force acting upon them is not a function of position. The addition of magnetic fields lifts the degeneracy of the Zeeman sub-levels, and can give rise to the position-dependent force required for a trap.

1.3.2 Magneto-Optical traps

Most experiments in which few or single neutral atoms are to be observed and manipulated require the atoms to have low kinetic energies. The cold atom source of choice in most experiments is the magneto-optical trap (MOT), a combination of inhomogeneous magnetic fields and suitably polarised red-detuned laser beams that lead to the stable confinement of atoms [22].
Let us consider a hypothetical atom with ground and excited state quantum numbers $J_g = 0$ and $J_e = 1$. An external magnetic field B in the z-direction B will split the upper level into three levels M_e=0 and M_e=1 through the Zeeman shift,

$$\Delta E = M_e g_e \mu_B B \tag{1.2}$$

Here, g_e is the Landé factor, μ_B is the Bohr Magneton and M_e is the projection of the angular momentum J_e onto the z-axis. The lower level does not split in this imaginary atom. In an absorption or emission process the total angular momentum of the atom and the photon must be conserved, leading to the following selection rules:
σ^+- polarised light is only allowed for $M_g = 0 \rightarrow M_e = 1$ transitions,
σ^--polarised light is only allowed for $M_g = 0 \rightarrow M_e = -1$ transitions, and
π-polarised light is only allowed for $M_g = 0 \rightarrow M_e = 0$ transitions. The polarisations must also be defined with respect to the local magnetic field direction. In a MOT, atoms are trapped by a clever arrangement of the magnetic field and beam polarisations. In the toy model above, this can be achieved by setting $B = z$. For an atom at a position $z > 0$, the sub-level with $M_e = -1$ will be shifted to a lower energy, that is towards the red. Now we apply a red-detuned, σ^--polarised beam

pointing in the negative z-direction, and a σ^+-polarised beam with the same detuning from the other side. The atom will then preferentially be pushed towards the origin because the $M_g = 0 \rightarrow M_e = -1$ transition, which is closest to resonance, can only be driven by the σ^--beam. The laser detuning and Doppler shift still lead to a slowing effect as above. Therefore the atoms are cooled as in molasses, but also collected at the origin. With the right configuration of polarisations and a quadrupole magnetic field, such a trap allows the confinement of atoms in three dimensions. The beams can be, for example, six separate beams as in the 3D-molasses described above. The same effect can be achieved with four beams if two of them are reflected on a mirror so as to propagate towards each others' sources. This is the type of MOT is known as a reflection MOT. It is common to most atom chip experiments, where the chip itself serves as the mirror, and indeed it is also the type used in this experiment. An even simpler configuration can be achieved in a concave-pyramidal mirror. In the simplest case with an opening angle of 90°, one incoming circularly-polarised beam is sufficient to produce all required beams for confinement in the opening.
At this point, a Rubidium MOT generally has already been cooled to a mean temperature of a few hundred μK. Once atoms have been collected in the trap, they can be cooled further by switching off the magnetic fields and increasing the detuning of the laser beams. In doing so, the scattering rate of the atoms decreases, but the main source of cooling is found in effects of the spatial dependence of the polarisation vector on the population distribution in the Zeeman sub-levels. These effects are commonly summarised under the term 'Sisiphus cooling'. These mechanisms allow the cooling of the atoms to temperatures on the order of tens of μK.

1.4 Chips and microcavities

1.4.1 Magnetic guides on atom chips

Once the atoms have been cooled to these low temperatures, they can be loaded into magnetic guides and traps, for example on atom chips. These are devices with micro-structured surfaces designed to produce magnetic and/or electric fields, which enable the trapping, cooling and manipulation of atomic clouds and single atoms [24]. Typically atom chips have dimensions of a few cm^2. An example of an atom chip is shown in Figure 1.3 (a). On chips with current-carrying wires, the wires have typical widths of 1 to 100 μm and thicknesses of 1 to 10 μm, and can carry currents on the order of 1 to 10A. This makes it possible to form strong and

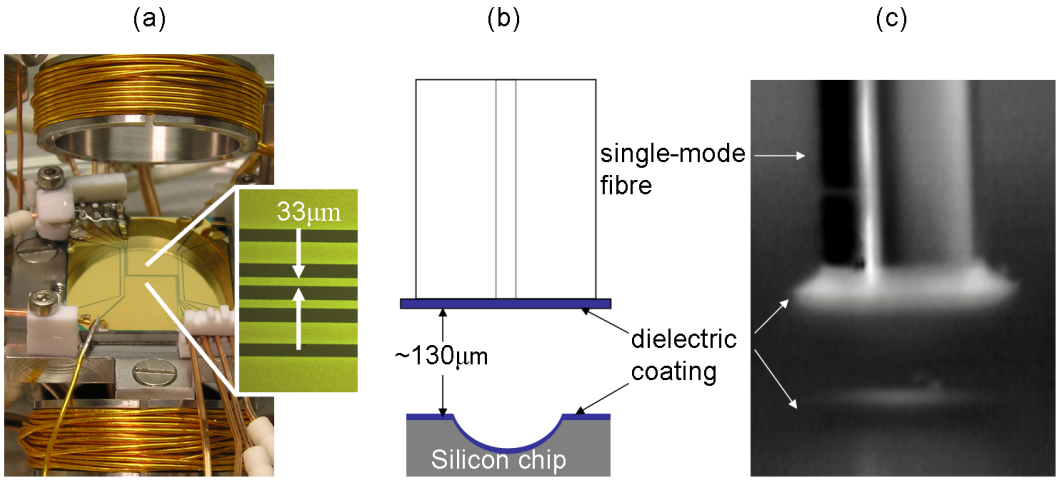

Figure 1.3: (a) An atom chip currently in use at the Centre for Cold Matter. The chip is gold-coated to provide the reflective surface for a reflection MOT. The large coils at the top and bottom of the photograph are used to create the quadrupole field for the MOT. The inset shows a magnified image of the central section of the current-carrying wires. (b) and (c) show a schematic diagram and a photograph of a microcavity of the type developed in the work for this thesis.

tight traps, with trap frequencies on the order of 10 kHz and trap depths on the order of 1 mK. Similar trap characteristics have been obtained with micro-patterned permanent-magnetic surfaces [25]. There are a number of motivating factors behind this quest for miniaturisation. From a purely technical point of view, the high magnetic-field gradients which can be created effortlessly on a chip are hard to produce using macroscopic coils or other means, because of the small scale of the features on atom chips. Looking further into the future, being able to perform high-precision measurements using such a small device means that in principle the devices could become as ubiquitous as traditional computer chips if they were able to fulfil a practical need. Furthermore, chips based on silicon offer the possibility of integrating standard electronic circuits onto the same surface, bringing them a further step closer to a complete "lab-on-a-chip". Two very practical applications of atomic physics which have already been demonstrated on a chip are the realisation of clocks and magnetometers [26]. There are also more futuristic proposals, for example the realisation of quantum computation schemes using atoms on chips [27]. The magnetic fields are produced by current-carrying wires or permanently magnetised surfaces and couple to the magnetic dipole moment of the atoms. The force acting upon atoms in such a trap derives from the gradient of the potential from Eq. 1.2. The field of a single wire on the chip, to which a uniform bias field

is added parallel to the surface of the chip, creates a zero of the magnetic field above the wire, surrounded by a region of approximately quadrupole asymmetry. Atoms in a weak-field-seeking state will be attracted and held in this region. At a zero of the magnetic field, the weak- and strong-field-seeking states of the atom are degenerate, so a transition may occur which would lead to repulsion of atoms from the trap. To avoid this, a uniform field can be added parallel to the wire, turning the zero of the field into a non-zero minimum. Losses can still occur, for example because of current noise caused by thermal fluctuations, though these can be controlled by a suitable choice of material and film thickness [28]. The lithographic process involved in creating the wires makes it possible to create complex patterns in a highly precise, repeatable manner, which in turn guarantees the scalability of these components. This means that in principle, an array of clocks, magnetometers or quantum-information-processing units can be produced on the surface of the chip by virtue of the microfabrication techniques implemented. Wires patterned using UV-lithography have edges with a feature size of less than 100 nm and with a surface roughness of less than 10 nm, creating a uniform trap for the atoms. It has been possible to trap, transport and Bose-condense atoms above the surfaces of atom chips, both with current-carrying structures and with permanently-magnetised devices [29, 25]. It is possible by these means to control the position of atoms to within a few nanometers. The regions of highest field strength in microcavities of our type are on the order of tens of nanometers, as detailed in the following subsection. Atom chips are therefore ideally suited for the delivery of atoms to microcavities on their surface.

1.4.2 Microcavities for atom chips

As mentioned earlier, microcavities can be used to detect atoms as well as to manipulate their internal state, and atom chips can trap, cool and guide atoms with high accuracy. It is clearly desirable to combine all these features in one device. Broadly, there are two types of microcavity which are being developed for this purpose: whispering-gallery-mode (WGM) resonators and Fabry-Pérot-type resonators. WGM cavities can provide large coupling values given their minute mode volume and narrow linewidth [5, 30]. However, because the intense part of the field is confined within the solid material of the resonator, atoms can only couple to the field through the weaker evanescent field outside the device. This decreases exponentially with distance from the resonator surface, with a decay constant of order $\lambda/2\pi$. For an atom to interact perceptibly with the resonator mode it must

therefore be placed very accurately, i.e. to within a small fraction of a wavelength, in close proximity of the resonator surface, where the attractive Van der Waals force on the atom becomes considerable. A number of WGM devices have been proposed as candidate systems for the detection and manipulation of atoms. Fused-silica microspheres are not easily included in the production of atom chips, as they would have to be positioned on the surface and attached to the atom chip using procedures separate from the standard etching and coating steps used in the manufacture of semiconductor chip devices. Microtoroids [5] are more natural candidates for integration as they can be produced using standard microfabrication techniques, and still offer very high quality factors. Strong coupling between single atoms and the field of a microtoroid resonator has in fact been demonstrated [30], albeit with atoms passing through the evanescent field in free-fall. The challenge of reliably positioning atoms in the evanescent field with the required accuracy has yet to be surmounted. By contrast, FP resonators give atoms direct access to the region of highest field strength of the cavity mode, leading in practice to higher values of g that are more readily reproducible. Furthermore the requirements on positional accuracy of the atoms within the mode are less stringent because the intensity varies with a standing wave spacing of $\lambda/2$ and a mode waist of 3-10 μm. For these reasons, the efforts of several research groups are currently geared towards including this type of resonator on atom chips. In the group of J. Reichel, the strong coupling of a magnetically transported, ultracold cloud of Rubidium atoms has recently been demostrated [31]. The resonators used there are made of two fibres, the tips of which are laser-machined to a concave shape with a low surface roughness of ~ 0.2 nm, coated to achieve a finesse of 35000. However, the fibres are fabricated and incorporated into the chip surface using many manual steps, a clear hindrance to the scalability of this design.

1.4.3 Our microcavities

The cavities developed during the course of this thesis are shown schematically in Figure 1.3 (b), and a microscope image of one such device is shown in Figure 1.3 (c). They were designed with the aim of combining the advantages of microfabrication, i.e. inherent scalability and integrability with atom-chip fabrication, with the advantages of fibre-coupling, namely the collection of photons in a well-defined mode and the possibilities offered by fibre-optic networks. To this end, a microfabrication procedure was sought which would allow the production of concave mirrors.

Isotropic etching of silicon is a well-developed technology [40], and after some optimisation it was possible to produce mirror substrates on silicon chips with sufficient quality to produce high-finesse microcavities. The silicon surfaces were coated with multilayer dielectric films. Using these mirrors, we have been able to achieve a reflectivity of over 99.9 % at our wavelength. Using microfabrication furthermore allows us to produce mirrors with small radii of curvature. As a consequence, the $1/e^2$-intensity radius of our cavity mode can easily be on the order of $3 - 5\,\mu$m, which is an order of magnitude smaller than that of standard Fabry-Pérot cavities used in atom-cavity experiments. This gives us a smaller mode volume and therefore a larger coupling constant g. Currently, our damping rates are still larger than the coupling rate, but improvements in the microfabrication procedure will amend this (see Chapter 8). The second mirror of the cavity is the tip of a single-mode fibre coated using a transfer procedure (see Chapter 3). This enables us to couple light in and out of the cavity directly via the fibre, without the need for any further coupling optics. These features show that the cavities are well-suited for both scalable integration and networking.

1.4.4 Thesis Outline

The rest of the thesis is dedicated to the development and first experimental results collected using these devices. Chapters 2 and 3 describe the optical features and the physical characteristics of the microcavities. Chapters 4 and 5 discuss how atoms will interact with the mode of such a resonator, and what we expect to see in our measurements. The results of the latter are shown in Chapter 7. The thesis ends with an outlook on the future of these devices.

Chapter 2

Optics

The fundamental tools used to describe the microcavities developed for our experiment are given in this chapter.[39, 38] The aim is to supply the definitions of quantities commonly used in this thesis. In our microcavities, the stable modes can be described using a complete, orthonormal set of solutions to the paraxial wave equation, for which the Hermite-Gaussian set is chosen. The mode exiting the fibre which is used to drive and measure the cavity is a Bessel beam, but can also be approximated with very high accuracy by a Gaussian beam. The operation of optical resonators will be described in the general case, and in the specific case of a plano-concave geometry. The equations provided in this chapter allow an in-depth analysis of the measured characteristics of our fibre-coupled resonators.

2.1 Gaussian Beams

Despite their small size, the modes formed in our resonators will in general still have a transverse extent a few times the wavelength. This is also true for the mode in the optical fibres used for these devices. The expansion due to diffraction caused by this transverse confinement is slow enough to allow the use of the paraxial approximation to the Helmholtz equation. The latter has a complete set of orthonormal solutions of the form

$$E_{h,v}(x,y,z) = E_0 e^{-\mathrm{i}kz} E_r(x,y,z) H_h\left[\frac{\sqrt{2}x}{w(z)}\right] H_v\left[\frac{\sqrt{2}y}{w(z)}\right] \Phi_z^{h,v} \Phi_r \ . \tag{2.1}$$

Here, E_0 is the electric field strength at the origin. The envelope of the electric field strength decreases in all directions from the origin with

$$E_r(x,y,z) = \sqrt{\frac{2}{\pi}} \frac{1}{w(z)} e^{-\frac{x^2+y^2}{w(z)^2}}, \tag{2.2}$$

The radius of the beam, defined as the radial distance from the beam centre at which the electric field strength has decreased to E_0/e, and its intensity to I_0/e^2 (see Fig. 2.1 (b)), is given by w_0 at the origin, and increases with distance as

$$w(z) = w_0\sqrt{1 + \left(\frac{z}{z_R}\right)^2} \tag{2.3}$$

with $z_R = \frac{n\pi w_0^2}{\lambda}$, where n is the refractive index of the material in which the field is propagating. This is the distance in z at which the $1/e$-field radius has increased to $\sqrt{2}w_0$, which is known as the Rayleigh length of the beam. The nature of the solution allows for higher-order transverse field modulations in the x, y-plane. These are given by the Hermite polynomials[1]

$$H_m(u) = (-1)^m e^{u^2}\frac{d^n}{du^n}\left(e^{-u^2}\right), \quad \text{with} \quad n \in \mathbb{Z}^+ \ . \tag{2.4}$$

For the fundamental mode, in which $h, v = 0$, Equation 2.1 reduces to the well-known $TEM_{0,0}$ mode. The main properties of this simplest solution are shown in Figure 2.1.

The beam expansion is shown in Figure 2.1 (a) as a dashed line. The divergence of the beam tends to a maximum of $\theta_{max} = \lambda/(\pi w_0)$, as shown in Figure 2.1. The phase varies transversely with

$$\Phi_r = exp\left[-\mathrm{i}\frac{k(x^2+y^2)}{2R_z}\right] \ , \tag{2.5}$$

giving the beam a spherical wavefront with a radius of curvature of

$$R(z) = z + \frac{z_R^2}{z} \ , \tag{2.6}$$

which reaches its minimum at z_R. The evolution of the curvature of the wavefront is shown on the right side of 2.1 (a).

With higher-order modes, the dependence of the field on the transverse coordinates is additionally determined by the Hermite polynomials of the appropriate

[1]The Hermite-Gaussian set of beam propagation modes is not the only complete set of orthonormal modes. Another set of solutions is given by Laguerre-Gaussian (LG) polynomials, which possess radial symmetry and can be a more convenient choice for the description of some systems. Of course these two descriptions are equivalent, and each mode of one basis can be described as a linear superposition in the other. HG modes have transverse momentum, while LG modes have orbital angular momentum. They can be seen in analogy to the linear and circular polarisation bases, which describe the internal oscillations or spin of the field excitation. They are furthermore identical to the modes of the 2D quantum simple harmonic oscillator.

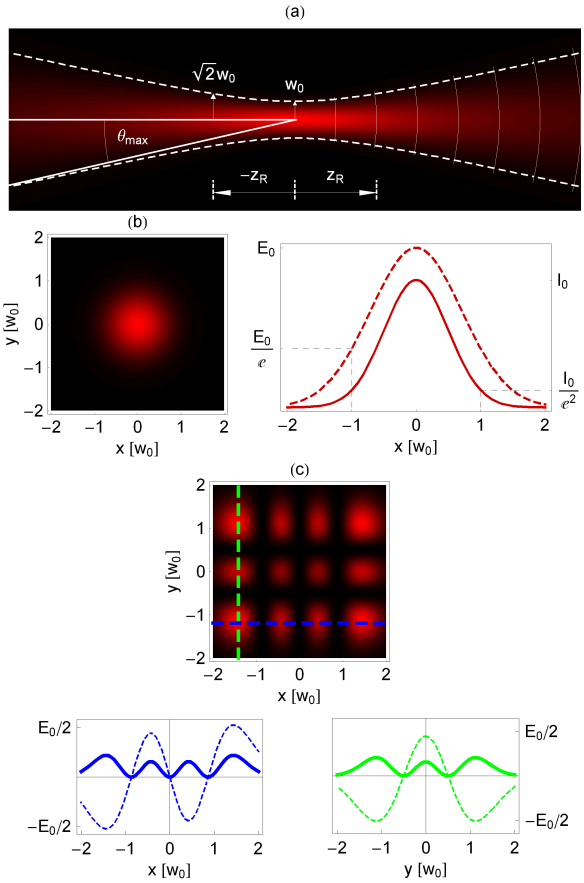

Figure 2.1: (a) Main features of the fundamental Gaussian beam (see text). (b) Intensity distribution in the $x, y-$ plane of the fundamental mode, and the field (dashed line) and intensity (solid line) along a line through the origin. (c) Intensity distribution of a $TEM_{3,2}$ mode at the waist, and field (dashed) and intensity (solid) along the dashed green and blue lines in the contour plot, shown in the respective colour.

order. An example of a higher-order mode is given in figure 2.1 (c). The phase variation with z for any mode (h, v) is given by

$$\Phi_z^{h,v} = exp\left[\mathrm{i}(1+h+v)\tan^{-1}\left(\frac{z}{z_R}\right)\right] \ , \tag{2.7}$$

These equations give the magnitude of the electric field for all points in space. The electric field vector is parallel to the wavefront at all points of the field, while its orientation is given by the polarisation of the light.[2]

Elliptical beams can also be described by using the set of solutions in Equation 2.1. A field with waists w_0^x, w_0^y is given by the product of the solutions calculated separately for each axis.

2.2 Resonators

We now consider the propagation of light when it is confined by opposing mirrors. This leads to repeated propagation and constructive or destructive interference, depending on the boundary conditions of the resonator. For a plane wave of amplitude E_0 impinging upon a resonator, the light circulating inside the resonator results in a field given by the sum

$$E_{circ} = t_1 E_0 \sum_{m=0}^{\infty} (r_1 r_2 e^{\mathrm{i}\phi})^m = E_0 \frac{t_1}{1 - r_1 r_2 e^{\mathrm{i}\phi}} \ , \tag{2.8}$$

where ϕ is the round-trip phase shift of the cavity. For a plane wave in a resonator with plane mirrors it is given simply by $\phi = 2nkL$, where n is the refractive index. The resulting circulating intensity is

$$I_{circ} = |E_{circ}|^2 = I_0 \frac{T_1}{|1 - \sqrt{\rho_1 \rho_2} e^{\mathrm{i}\phi_c}|^2} \ . \tag{2.9}$$

Here L is the length of the resonator, and $r_j\,(\rho_j)$ and $t_j\,(T_j)$ are the amplitude (intensity) reflection and transmission coefficients of each mirror. This leads to the presence of fringes in both the reflection and transmission signals of the resonator (see Fig. 2.2 (a)). In the overall phase term $\phi_c = \phi + \phi_0$, ϕ_0 denotes an additional phase shift which depends on the properties of the mirror surfaces, and is given by $\phi_0 = \arctan[(Im\{r_1 r_2\})/(Re\{r_1 r_2\})]$. From this, the transmitted and reflected

[2]Having their origin in the paraxial approximation, these equations maintain validity only insofar as $w(z)$ varies slowly with respect to the phase, i.e. negligibly over one wavelength. This is the case for $z_R \gg \lambda$. With light propagating in free space with a wavelength of $\lambda \sim 780\,\mathrm{nm}$, it is therefore safe to use this approximation for beam waists $w_0 > 2\,\mu\mathrm{m}$, such that the Rayleigh range extends over 20 wavelengths.

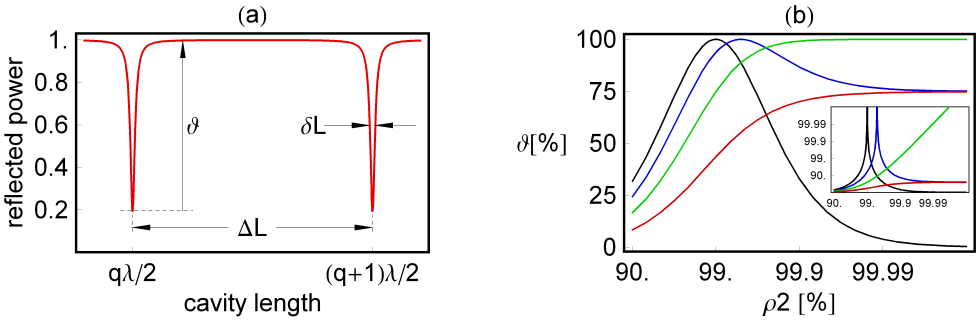

Figure 2.2: (a) The power reflected by a plane-plane optical resonator reaches minima at resonator lengths of $(q+n)\lambda/2$, with a contrast of ϑ and a width δ_L. Together with the fringe separation Δ_L, here $\lambda/2$, this gives the finesse, $F = \Delta_L/\delta_L$. (b) Reflection fringe contrast for a resonator with input-mirror reflectivity $\rho_1 = 99\%$, plotted for internal losses of $L_1 = 0$ (black),$L_S/2$ (blue), L_S (green) and $3L_S/2$ (red), where $L_S = 1 - \sqrt{\rho_1}$. The inset shows the same curves on a logarithmic scale.

amplitudes and intensities can be calculated. While the transmitted intensity is simply $T_2 I_i$, the cavity reflection must be calculated from the addition of the initial back-reflection from the input mirror and the backward leakage from the resonator,

$$E_r = t_1 r_2 e^{i\phi_c} E_{circ} - r_1^* E_0, \quad \text{therefore} \quad I_r = I_0 \rho_1 \left| \frac{-1 + \left(1 + \frac{T_1}{\rho_1}\right)\sqrt{\rho_1\rho_2}e^{i\phi_c}}{1 - \sqrt{\rho_1\rho_2}e^{i\phi_c}} \right|^2 . \quad (2.10)$$

The depth of the reflection resonance troughs is given by the fringe contrast,

$$\vartheta = 1 - \frac{I_{min}}{I_{max}} = 1 - \left(\frac{(\sqrt{\rho_2}(1-L_1) - \sqrt{\rho_1})/\xi}{(\sqrt{\rho_2}(1-L_1) + \sqrt{\rho_1})/(2-\xi)} \right)^2 \quad \text{with} \quad \xi = 1 - \sqrt{\rho_1\rho_2}. \quad (2.11)$$

The quantity ξ is instantly recognisable as the round-trip field loss of an empty cavity. Figure 2.2 (b) shows the effects of increasing internal losses L_1 in the input mirror. For an input mirror with internal losses $L_1 = 0$ (black curve), the contrast reaches 1 for $\rho_2 \cong \rho_1$. For $L_1 < 1 - \sqrt{\rho_1}$, the contrast reaches 1 at increasing values given by $\rho_2 = \rho_1/(L_1 - 1)^2$. An example is given with $L_1 = (1 - \sqrt{\rho_1})/4$ (blue). If $L_1 < 1 - \sqrt{\rho_1}$, the destructive interference can no longer be complete, as shown by the red curve with $L_1 = 3(1 - \sqrt{\rho_1})/2$. However, in the special case $L_1 = 1 - \sqrt{\rho_1}$ (green), the fringe contrast improves indefinitely with increasing ρ_2.[3] When the

[3]This may become a useful tool in creating high-contrast resonators in future cavity generations. However, it will requires some testing and a number of coating trials to achieve the desired transmittance. It is of course not helpful to decrease the transmittance when the application is the collection of cavity photons.

losses in the mirrors are negligible, i.e. when $T_i \simeq 1 - \rho_i$, the maximum reflected intensity will be

$$I_{max} \simeq 1 \text{ for } \xi < 0.1. \tag{2.12}$$

It shall henceforth be assumed that the amplitude reflection coefficients of the mirrors are real, that the refractive index within our resonators is $n = 1$, and that condition (2.12) is valid. The minimum reflected intensity is then

$$I_{min} = \left(\frac{\sqrt{\rho_1} - \sqrt{\rho_2}}{\xi} \right)^2 \text{ so that } \vartheta = 1 - I_{min} = 1 - \left(\frac{\sqrt{\rho_1} - \sqrt{\rho_2}}{\xi} \right)^2 . \tag{2.13}$$

This approximation of ϑ gives a relatively simple measure of the difference between the reflectivities of the two mirrors. For a fixed cavity length, the periodicity of the reflection fringes is of the cavity's free spectral range, $FSR = \Delta_\omega = \pi c/L$ for a plane-mirror resonator, in angular frequency. For sufficiently high reflectivity, the reflected intensity close to a resonance is excellently approximated by a Lorentzian. In terms of frequency, the half-width at half maximum $\kappa \equiv \xi c/2L$ results simply from the round-trip field losses per round-trip time in this approximation. κ is therefore the amplitude decay rate of the cavity, in units of angular frequency. Then

$$\frac{I_r(\Delta_{CL})}{I_0} = 1 - \vartheta \frac{\kappa^2}{\kappa^2 + \Delta_{CL}^2} , \tag{2.14}$$

where the detuning of the driving light from the cavity is given by Δ_{CL}=$\omega_{light} - \omega_{cavity}$. The same is true for the cavity length at a fixed wavelength: the fringes of a plane-mirror resonator have a periodicity of $\Delta_L = \lambda/2$ in cavity length, and the reflection around one resonance is

$$\frac{I_r(L)}{I_0} = 1 - \vartheta \frac{(\delta_L/2)^2}{(\delta_L/2)^2 + L^2} . \tag{2.15}$$

It is now possible to characterise the cavity by measuring its finesse

$$F = \frac{\Delta_{CL}}{2\kappa} = \frac{\Delta_L}{\delta_L} = \frac{\pi \sqrt[4]{\rho_1 \rho_2}}{\xi} \approx \frac{\pi}{\xi} , \tag{2.16}$$

where δ_L is the full width at half-maximum of the fringe. The final approximation is sufficiently accurate for our high-reflectivity mirrors and with it, the cavity decay rate is given by $\kappa \simeq \pi c/2LF$. The finesse of the cavity can now be measured by scanning the cavity length through two adjacent resonance fringes. From this value, the geometric mean of the mirror reflectivities can be calculated. By measuring finesse and contrast it is therefore possible to determine the reflectivity of each mirror, by making an assumption as to which mirror has the higher reflectivity.

The plane-plane configuration for which the above is valid is a so-called unstable geometry. This is to say that, unless the input plane wave and the mirrors are of

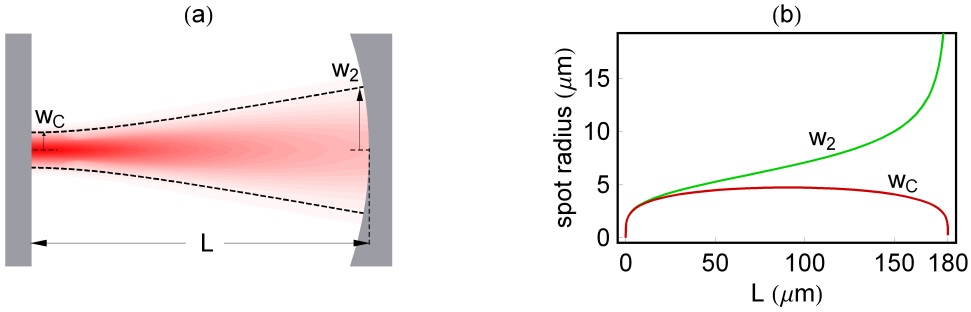

Figure 2.3: (a) A plano-concave resonator has its mode waist w_C on the surface of the plane mirror. The spot size on the curved mirror, w_2, increases with cavity length because of diffraction. (b) Spot radii on the surfaces of a plano-concave resonator with a mirror curvature of 180 μm.

infinite transverse extent, the light will diffract and part of the energy of the input beam will be lost as it propagates beyond the edges of the mirrors. To create a stable resonator, at least one of the mirrors must be concave to re-focus the light so that the propagation is identical in each round-trip. It is possible to determine whether or not a cavity geometry is stable with the equations in Section 2.1, simply by applying the condition that there exists a cavity mode which has exactly the same beam waist and curvature after one round-trip.

For the case of spherical mirrors, this leads to the stability condition

$$0 \leq G_1 G_2 \leq 1\,, \quad \text{where} \quad G_i = 1 - \frac{L}{R_i} \tag{2.17}$$

and R_i are the radii of curvature of the cavity mirrors. Solutions of the type given in 2.1 are readily found by straightforward algebra. The G-factors can now be used to calculate the spot sizes on the cavity mirrors and the cavity waist:

$$w_1 = \sqrt{\frac{L\lambda}{\pi}} \sqrt[4]{\frac{G_2}{G_1(1-G_1G_2)}}, \quad w_2 = \sqrt{\frac{L\lambda}{\pi}} \sqrt[4]{\frac{G_1}{G_2(1-G_1G_2)}}$$
$$\text{and} \quad w_C = \sqrt{\frac{L\lambda}{\pi}} \sqrt[4]{\frac{G_1G_2(1-G_1G_2)}{(G_1+G_2-2G_1G_2)}} \tag{2.18}$$

The discussion until this point has allowed for a wide range of possible resonator shapes. For our experiment, the special case of a plano-concave resonator, i.e. a cavity with a plane mirror and a concave mirror with a radius of curvature R, is discussed. In this case, $G_1 = 1$ and $G_2 = 1 - L/R$ so that the stability condition 2.17 reduces to $0 \leq L \leq R$. The beam waist in such a resonator is then found on

the plane mirror, so the spot sizes on the mirrors, indicated in Figure 2.3 (a) are given by

$$w_1 = w_C = \sqrt{\frac{\lambda}{\pi}} \sqrt[4]{RLG_2} \text{ and } w_2 = \frac{w_1}{\sqrt{G_2}} \, . \tag{2.19}$$

Their length-dependence for cavities of our type is shown in Fig. 2.3 (b). The cavity field can take the shape of any superposition of the Hermite-Gaussian modes (2.1). However a round-trip of the cavity will, in general, cause a different phase shift for modes of different order, as given by Eq. 2.7. A mode of order (h, v) will therefore only be resonant when the cavity length satisfies

$$L_{q,h,v} = \frac{\lambda}{2} \left[q + \frac{h+v+1}{\pi} \arccos\left(\sqrt{G_2}\right) \right] \tag{2.20}$$

Armed with the formulae and definitions given in this chapter, it is possible to examine the behaviour of a plano-concave resonator coupled to a single-mode fibre. In the following chapter, the development of high-finesse resonators at the Centre for Cold Matter will be described, and the results from the measurements performed on these devices are analysed using the framework given in this Section.

Chapter 3

Devices

In this Chapter, the development of the fibre-coupled microcavities used in the experiment is described. Both mirrors used in our devices are custom-made, and their features are described in Section 3.1. The particular characteristics of our devices require the simple theory in Chapter 2 to be extended to allow for the discontinuity in mode structure at the interface between the cavity and the coupling fibre. While a complete description of these systems can only be achieved by numerical means, most of their features are encompassed by two limits, which are described in Section 3.3. With this type of microcavity, finesse values in excess of 5000 were achieved by increasing the reflectivities of the mirror coatings. These results are shown in Section 3.4.

3.1 Building the microcavities

The microcavities in use at CCM are intended for integration with atom chips (see Chapter 1). They have a plano-concave geometry, the plane mirror being a dielectric coating attached to the tip of a single-mode fibre, while the concave mirror is formed by coating an isotropically etched silicon surface. The latter renders the integration with existing atom chip technology particularly simple, as the necessary etching steps can be included without difficulty in the standard silicon fabrication procedure. The plane mirror is attached to the fibre tip using a so-called transfer procedure.[1] Initially, the mirror is formed by multilayer evaporation onto a specially prepared glass substrate. The preparation consists in coating the glass surface with a saline solution, to which the multilayer film adheres with variable strength depending on the concentration of the solution. The adhesion furthermore depends on the number of layers in the coating, because the internal tension in the dielectric

[1] manufacturer: O. I. B. Jena GmbH, Göschwitzer Str 22 Jena D-07745, Germany.

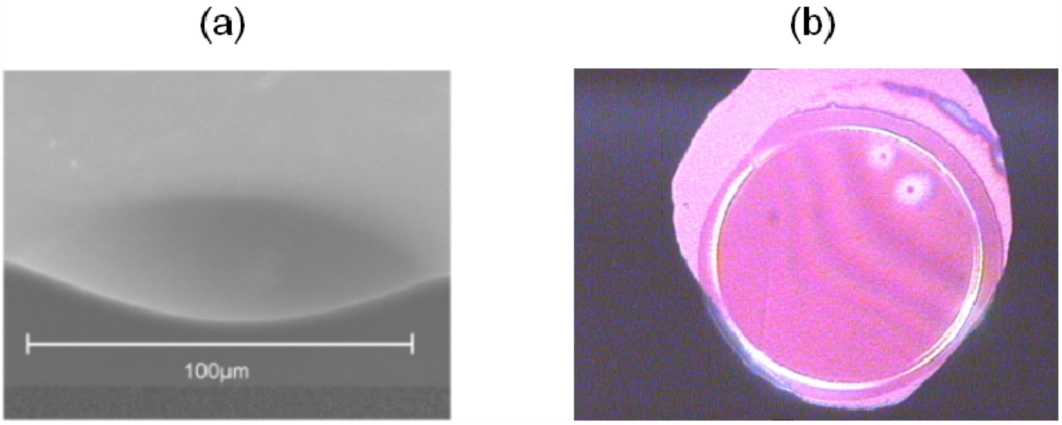

Figure 3.1: (a) SEM image of a silicon mirror template cleaved close to its centre. (b) Microscope image of a dielectric coating glued to the tip of a single-mode fibre.

multilayer structure increases with the number of layers. This is important in practice because the reflectivity of the multilayer film depends on the number, thickness and material of the dielectric layers, so that for each desired reflectivity, the correct concentration of the solution must be found empirically. The goal is to find a concentration which will hold the film firmly enough to the glass substrate, but weakly enough to be detached using the transfer procedure. The transfer procedure is performed as follows:

The single-mode fibre is cleaved with a 90° cut using a precision cleaver. The resulting surface is smooth enough to be used as a weak mirror. The fibre is then angularly aligned to the coated glass surface by maximising the fringe contrast at a large distance (in our case $\sim 300\,\mu$m), where the precision in angular alignment has a much greater effect on the contrast than a small change in position. This is measured by scanning the position of the fibre tip over a small range, i.e. a few wavelengths. It is possible to both move the fibre over a large distance and to scan it over a small range, using a micro-positioning stage onto which the fibre is mounted with a piezo actuator. Once satisfactory alignment has been achieved, the actuator is switched off and a small drop of UV-curing, refractive-index-matched glue[2] is placed on the multilayer film, close to where the fibre tip will make contact. The fibre tip is then dipped into the glue. The quantity of glue now present on the tip is still too large to achieve a strong and precise adhesion in the curing step. The excess glue is removed by making the drop of glue adhering to the fibre touch the multilayer surface gently a number of times. From experience, it appears that the

[2]NOA 88, manufacturer: Norland Products Inc.

ideal quantity of adhesive is present on the tip when the last contact leaves a drop of the same diameter of the fibre on the mirror surface. At this point, the fibre is "pushed" towards the mirror until a maximum is found in the reflected power. The UV-curing lamp is then switched on for $3 \times 300\,\mathrm{s}$, each from a different direction so as to cure the glue all around the fibre tip, and between the tip and the coating. The fibre is then pulled away slowly from the glass plate. This causes the multilayer film to tear around the fibre tip, with a portion of film remaining attached to the tip. The coated tip is then cleaned by dousing with distilled water, so as to remove any remaining saline solution, and blow-dried immediately to avoid the deposition of dust or other airborne particles. A fibre tip coated using this procedure is shown in Figure 3.1 (b).

The concave mirror of the microcavity is formed on a silicon wafer (see Fig. 3.1 (a)). The procedure used to create the mirror templates used for the experiments described in this thesis is the result of an empirical optimisation of the many parameters involved in the etching process. The wafer is wet-etched isotropically through circular apertures in a lithographic mask using a mixture of HF and HNO_3 in acetic acid. The etch bath in which the wafer is immersed undergoes continuous agitation during the etching process, resulting in an approximately spherical surface profile. The temperature, agitation speed, etch time, and etchant concentrations had to be optimised to approach an ideal surface profile. The concave mirror templates used in our experiments were profiled with an atomic-force microscope, displaying a surface roughness of approximately 6 nm RMS. Once the etching process is complete, the entire wafer can be coated with the desired reflective surface to give a concave mirror with the right reflective properties for the application envisioned.

3.2 Experimental setup and first results

The first coating used for the silicon mirrors was gold over chrome. Gold was chosen for its high reflectivity in the near-infrared part of the spectrum (98.6 % at 780 nm), and because it is a readily available coating material. The chrome layer provides the necessary adhesion between the silicon surface and the gold coating. An AFM scan of the gold-coated mirror surface showed that the coated surface was rougher than the bare silicon, with an RMS roughness of $\sigma_{RMS} = 9\,\mathrm{nm}$. The decrease in reflectivity due to scattering caused by this roughness can be calculated by multiplying with a Debye-Waller loss factor so that

$$\rho_2^{DW} = \rho_2 e^{-(4\pi\sigma_{RMS}/\lambda)^2} \quad , \tag{3.1}$$

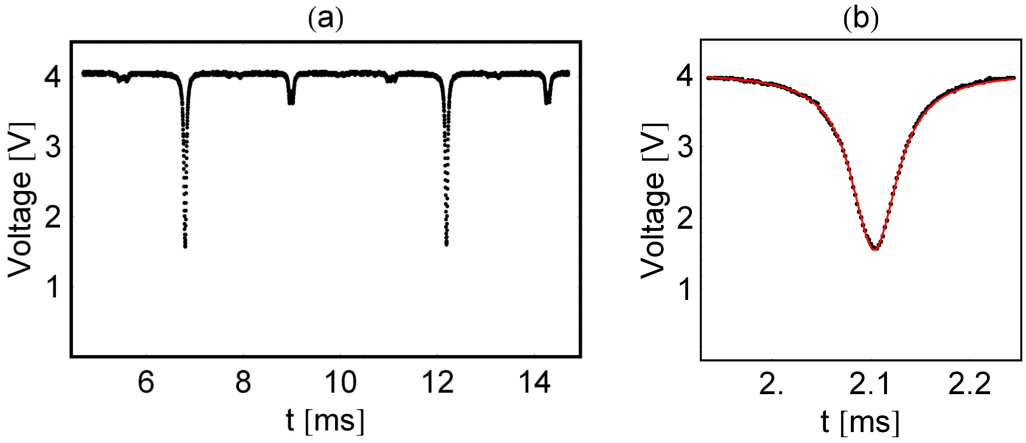

Figure 3.2: (a) Example of a reflection trace, showing two lowest-order fringes and a variety of higher-order fringes. (c)Detail of the first lowest-order fringe with a Lorentzian fit.

leading us to expect a mirror reflectivity of $\rho_2^{eff} = 96.5\%$. The radius of curvature of the mirror surface was also measured using the AFM, resulting in values of $R(a) = 177\,\mu$m and $R(b) = 168\,\mu$m along the two perpendicular axes of the measurement. From the SEM scan, the mirror template is known to have a diameter of approximately $D = 100\,\mu$m. For large spot sizes on this mirror, this will cause an aperture loss, leading to a spot-size dependent reflectivity. By inclusion of the Debye-Waller loss factor, the effective reflectivity of the concave mirror can now be approximated by

$$\rho_2^{eff} = \rho_2 e^{-(4\pi\sigma_{RMS}/\lambda)^2}\left(1 - e^{-2(\frac{D}{w_2})^2}\right) \quad , \tag{3.2}$$

The dielectric mirror transferred to the fibre tip for these measurements was specified by the manufacturer to have a reflectivity of $98\,\% \leq \rho \leq 99\,\%$. The optical fibre used for these experiments[3] was a single-mode, non-polarisation-preserving fibre. The typical $1/e^2$-intensity radius for this model is $w_F = 2.65\,\mu$m. Cavities consisting of these elements were analysed in detail to measure their performance and discover their peculiarities. The cavity characteristics could now be ascertained by measuring the power of light reflected back from the cavity through the input fibre (see Figure 3.2). A grating-stabilised diode laser tuned to 780 nm, passing through a beam splitter, is coupled into the input fibre using a microscope objective. To avoid back-reflection from the cleaved input surface of the fibre, the fibre is set at a small angle to the input beam, excluding etalon effects at the cost of a slight

[3] $SM750$. Manufacturer: Fibercore Limited, Fibercore House, University Parkway, Chilworth Science Park, Southampton, Hampshire, SO16 7QQ, United Kingdom

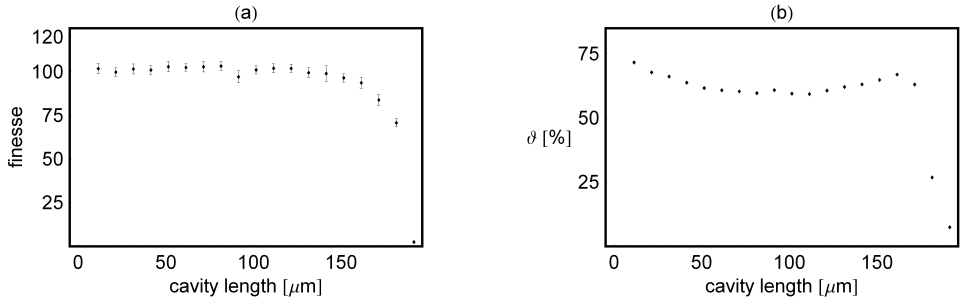

Figure 3.3: (a) Finesse of the cavity as a function of length. Each point shown is the average of 5 measurements. Each error bar is calculated from the statistical uncertainties of the fringe widths and separations. (b) Fringe contrast of the cavity as a function of cavity length. The error bar is given by the statistical spread of the measured values.

reduction in coupling efficiency. Part of the light returning from the cavity through the fibre exits the beamsplitter through the transverse arm, reaching the detector. The chrome+gold-coated silicon chip with the concave mirrors is attached to a piezo stack. The stack is driven through a power supply with a triangle waveform so as to move the mirror periodically with an amplitude of $2\,\mu$m, i.e. through at least four resonances. These are visible as dips in the power reflected from the cavity. The two central dips, shown in Figure 3.2 (a), are then used to measure the fringe visibility and finesse. These fringes are chosen because the piezo acceleration in this region of the scan is small and can be assumed constant. As described in Chapter 2, the finesse is calculated from the measured values as the fraction of the fringe separation divided by the fringe FWHM, Δ_L/δ_L. The values for δ_L are calculated using a Lorentzian fit to each lowest-order fringe, as shown in Fig. 3.2 (b). To average out the acceleration, the mean of the fringe widths of the first and second fringe is taken. To average out the effects of additional noise, five fringe traces are recorded. The contrast in terms of measured voltage is simply $(V_{max} - V_{min})/V_{max}$, as the detector used has a linear response to power in the range of the measurement. Finesse and contrast are measured in this way at multiples of $10\,\mu$m, starting with the two mirrors almost in contact, and ending where the cavity becomes unstable and the fringes disappear. The average of the measured finesse and contrast values are plotted, together with their statistical uncertainties, in Figure 3.3 (a) and (b).

To determine the radius of curvature, the distance between the resonant lengths of the lowest-order modes and the first set of even radial modes (see Figure 3.2 (b)) is determined, after converting the time-voltage data from the oscilloscope into

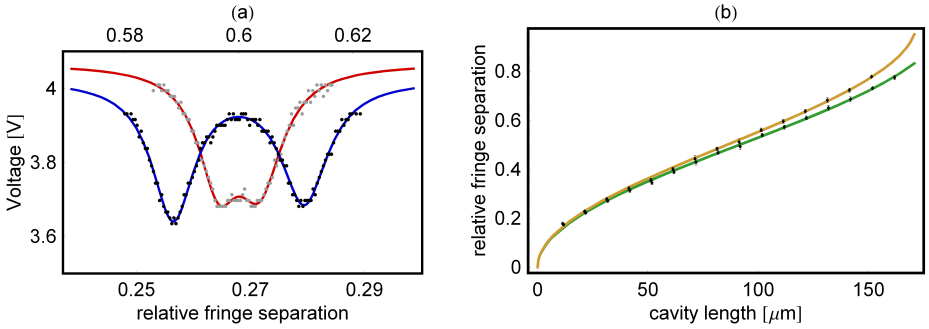

Figure 3.4: (a) Splitting of the second-order radial fringes, $TEM_{q,0,2}$ and $TEM_{q,2,0}$, due to astigmatism. The plots show the voltage detected as a function of distance in terms of the fraction $(L_{q,h,v} - L_{q,0,0})/(L_{q+1,0,0} - L_{q,0,0})$, for cavity lengths of 32 μm (grey dots, red fit curve, lower tick marks) and 112 μm (black dots, upper tick marks, blue fit curve). (b) Separation between the second-order radial fringes and the $TEM_{q,0,0}$ fringe, as a function of cavity length. A least-squares fit gives values of $R_a = (183 \pm 4)\,\mu$m and $R_b = (172 \pm 4)\,\mu$m, and an initial mirror separation of $(12 \pm 3)\,\mu$m.

length-voltage data to take into account the acceleration calculated in the finesse measurement. The resulting fractional displacement is plotted in Figure 3.4 (b). The plot shows a non-degeneracy of the $TEM_{q,0,2}$ and $TEM_{q,2,0}$ fringes, which grows as a function of cavity length. Two examples of the fringe splitting, at cavity lengths of 32 μm 112 μm, are shown in Fig. 3.4 (a). This is caused by astigmatism in the concave mirror. The red line shows a double-Lorentzian fit to the fringes at a cavity length of 32 μm (grey dots, lower tick marks), where the non-degeneracy first becomes evident. The blue line is a fit to the doublet at $L = 112\,\mu$m (black dots, upper tick marks), where the fringes are almost entirely distinct. The fringe traces allow us to deduce radii of curvature of $R_a = (183 \pm 4)\,\mu$m and $R_b = (172 \pm 4)\,\mu$m, and an initial mirror separation of $(12 \pm 3)\,\mu$m. The radii measured in this way are in reasonable agreement with the aforementioned AFM results.

3.3 Interpretation of Results

In the following, a number of approximations will be made to simplify the treatment of the results. The concave mirror will be treated as perfectly spherical, while the fibre mirror will be treated as perfectly flat, infinitely thin and in immediate contact with the fibre output. The repercussions of these simplifications will be taken into

account when discussing the measurements.

As mentioned in Chapter 2, the light exiting the tip of a single-mode fibre is well-described by a Gaussian beam with an electric field function of

$$\psi_F = \sqrt{\frac{2}{\pi}} \frac{1}{w_F} e^{-\frac{x^2+y^2}{w_F^2}} \quad , \tag{3.3}$$

where the normalisation factors have been chosen so that the power in the beam, $\int_{-\infty}^{\infty}\int_{-\infty}^{\infty} |\psi_F|^2 \, dx \, dy = 1$. The excitation of any given cavity mode $\psi_C^{N,h,v}$, where N denotes the longitudinal mode number and h, v denote the horizontal and vertical transverse mode numbers, is then given by the mode overlap

$$\eta_{N,h,v} = \int_{-\infty}^{\infty}\int_{-\infty}^{\infty} \psi_F^* \psi_C^{N,h,v} \, dx \, dy \quad , \tag{3.4}$$

The light exiting the fibre will excite the coherent superposition of cavity modes which it best matches. The resonator field equations must be applied separately for each mode, after which the total circulating, transmitted and reflected fields can be calculated by summation. However, the fibre and cavity will support different sets of modes. The cavity will support the set of Gaussian modes described in the previous Chapter, while the radial variation of the refractive index in the fibre means it will not support the same set of modes.[41] To elucidate this complication, it is instructive to consider what can happen to an excitation of a given mode leaving the cavity. If it exits the cavity via the fibre mirror, it will either

1) excite the single propagating fibre mode, or

2) be rejected by the fibre and re-enter the cavity, or

3) enter the fibre cladding.

The amplitude of option 1) is simply given by the mode overlap of the initial mode and the fibre mode. The repartition of probabilities of options 2) and 3) is not as straightforward. To fully evaluate them requires the calculation of the form of all possible modes of the fibre structure including core, cladding and air modes [41], after which the mode overlap of these with the cavity mode can be calculated. This is a large numerical calculation which goes beyond the scope of this thesis. The system can nonetheless be described with some accuracy by considering the two limits of repartition, i.e.

i) the *reflection limit*, in which all light which does not overlap with the fibre mode is reflected back at the fibre interface, and

ii) the *transmission limit*, in which all light which does not overlap with the fibre mode is lost into the fibre cladding and from there into free space.

It will become evident that the two limits give good approximations when describing

certain situations, and are useful by giving bounds in all others. Here, only the results of the changes to the equations in Chapter 2 for the evaluation of these two limits are given. The interested reader can explore the details of the amendments necessary for the calculation of these limits in Appendix A. The reflection limit will be described first, as it leads to some very simple expressions for the fringe visibility and finesse when a further set of reasonable approximations is made. The system will be described by considering the field of a single cavity mode. The total field can be found by summation as the modes are orthogonal. To further simplify the discussion, losses in the input mirror are neglected[1], and ρ_1 and ρ_2 are assumed to be real. The equations in Chapter 2 must now be modified to take into account the increase in reflection back into the resonator. Given the above, the effective reflectivity and transmission of the fibre mirror become

$$\rho_1^{eff}(h,v) \equiv \rho_1 + (1-\rho_1)(1-\eta_{h,v}^2) = 1 - \eta_{h,v}^2(1-\rho_1) \text{ , and}$$
$$T_1^{eff}(h,v) \equiv 1 - \rho_1^{eff}(h,v). \tag{3.5}$$

If both the cavity mirrors have high reflectivity and the apposite superposition of cavity modes matches all but a negligible part of the fibre mode, we can furthermore assume that the cavity will completely reject light from all non-resonant modes, so the reflected intensity simplifies to that of the general resonator from Chapter 2, with $\rho_1 \to \rho_1^{eff}$. In this approximation, the equations for both finesse and fringe visibility from Chapter 2 can therefore be used with the substitution $\rho_1 \to \rho_1^{eff}$.
In the transmission limit the fraction of light exiting the cavity which does not match the fibre mode is assumed to be lost instead of being reflected back into the cavity, so the finesse is not expected to change in this limit. Equation 2.16 can therefore be used without modification. For the fringe contrast however, this loss needs to be taken into account, together with the rejection of mismatched input light which is again assumed to be complete. This leads to an expected fringe contrast of

$$\vartheta_{h,v}^{TL} = 1 - \left(-r_1^{eff}(h,v) + T_1^{eff}(h,v)\frac{r_2}{1-\sqrt{\rho_1\rho_2}}\right)^2. \tag{3.6}$$

The crucial parameter for both limits is the mode overlap between the fibre and cavity modes. Given the astigmatism of the cavity, the overlap integral for the lowest-order modes is given by

$$\eta_{0,0} = \frac{2w_F\sqrt{w_X w_Y}}{\sqrt{w_F^2(w_X^2+w_Y^2+w_F^2)+(w_X w_Y)^2}}. \tag{3.7}$$

[1] in our measurements, this is an acceptable approximation as the losses in this type of dielectric film heave been measured to be on the order of 6 parts per million[11], while our transmission is larger than 100 p.p.m. in all measurements.

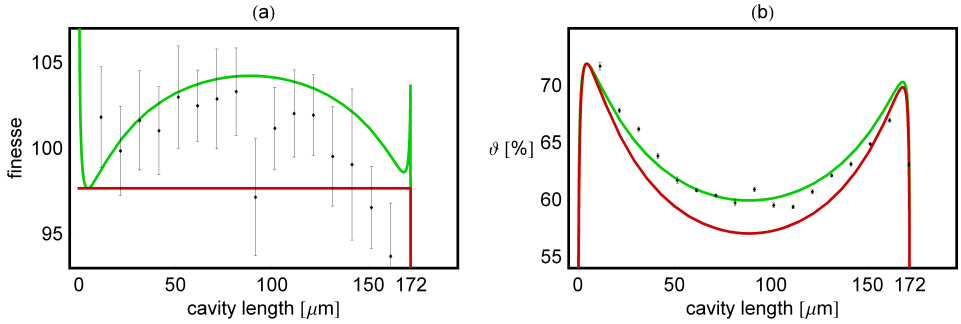

Figure 3.5: Comparison of experimental data and theoretical predictions for finesse (a) and fringe contrast (b). The predictions of the reflection limit (green lines) are, in general, closer to the measured values than those of the transmission limit (red lines). The parameters used for the theory plots are: $\sigma_{RMS} = 9\text{nm}$ giving $\rho_2^{DW} = 96.5\%$, $\rho_1 = 98.5\%$, $w_F = 2.65\,\mu\text{m}$, $R(a) = 183\,\mu\text{m}$, $R(b) = 172\,\mu\text{m}$.

With the measurements for mirror roughness, and the specifications given by the manufacturers for the single-mode fibre and the dielectric coating, these limits can now be compared to the experimental results from Section 3.2. The expected finesse and fringe contrast are plotted together with the experimental data in Figure 3.5. For the aperture loss, the geometric mean of the two spot size radii was used as the spot size, while the aperture itself was taken to be $100\,\mu\text{m}$, as given by the SEM image. Data at lengths greater than $170\,\mu\text{m}$ cannot be compared with the predictions as and the mode is no longer paraxial, and the cavity becomes unstable along one axis beyond $172\,\mu\text{m}$. Until that point however, both contrast and finesse measurements are for the most part encompassed by the two theoretical curves, showing slightly better agreement with the predictions of the reflection limit especially for small cavity lengths. In both cases, the measured value deviates strongly from theory at a cavity length of $92\,\mu\text{m}$. This can be reconduced to an increase of the mode overlap because of the transitional degeneracy of the $TEM_{0,0}$ mode with the $TEM_{0,4}$ and the $TEM_{4,0}$ modes (see Appendix A). The finesse drops more rapidly than expected towards the edge of the stability region, indicating additional spot-size-dependent losses of unknown origin, such as a smaller effective mirror aperture.

3.4 High-finesse microcavities

The results from the gold-coated mirrors showed that cavities constructed using these principles could achieve higher performance values by using higher-reflectivity

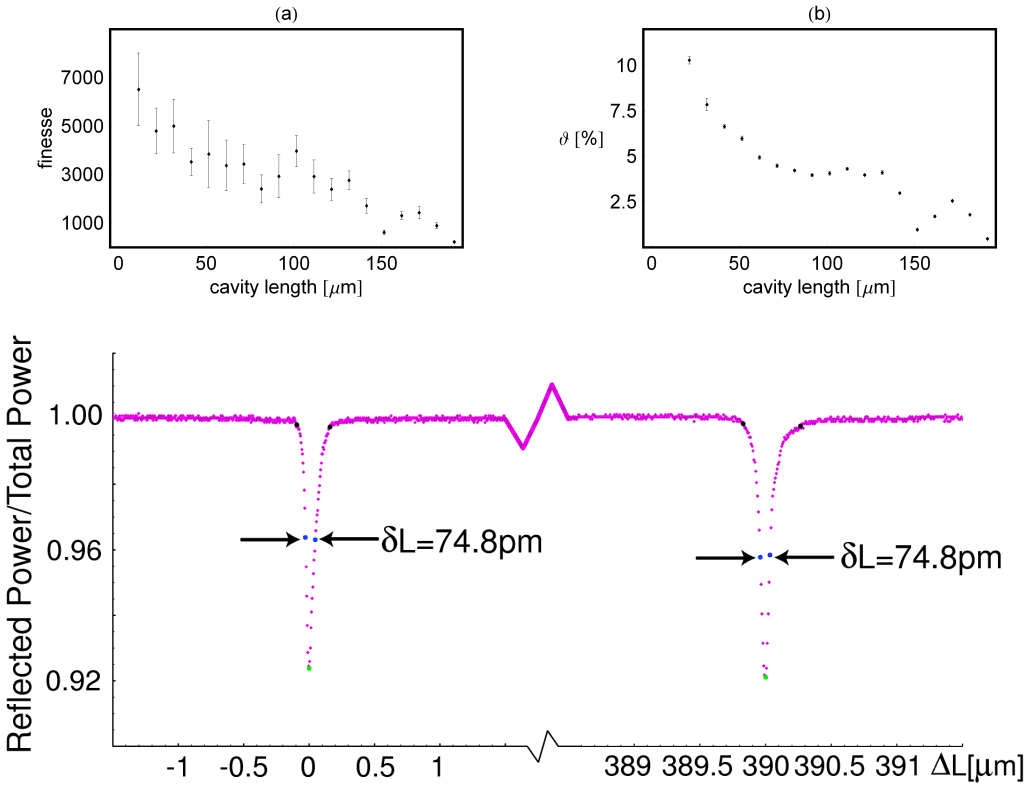

Figure 3.6: (a) Finesse, and (b) fringe contrast measured for different lengths of the high-finesse cavity. Below these, an example of fringes from the high-finesse resonator, displaying a finesse of 5200.

coatings. This was done by using dielectric coatings on both surfaces. However, because of the roughness of the silicon substrate, the reflectivity of the concave mirror is limited to 99.9%. The higher reflectivity nonetheless led to the achievement of a finesse exceeding 5000, as shown in Figure 3.6. The contrast in these measurements was low at only 10% for a cavity length of 30 μm, and decreased rapidly with cavity length, making a complete analysis as performed for the gold mirrors impossible. However, the results were useful in showing that to achieve good contrast, it would be necessary to lower the reflectivity of the input mirror to $99\% < \rho_1 < 99.9\%$. This would still give finesse values of over 500. As explained in Chapter 5, the small mode volume of the cavity should nonetheless make this value sufficient for the reliable detection of single atoms.

Chapter 4

Atoms and Light

This brief chapter introduces the interaction of atoms with light fields. Throughout this chapter, the atom will be treated as a quantum-mechanical two-level system, while the light field is initially treated as a quantum simple harmonic oscillator.[34, 35] In the limit of large excitation number, the treatment can be greatly simplified by replacing the quantised field with a classical wave picture.
The principles listed herein will then be used to treat the combined atom-cavity system in the rest of the thesis.

4.1 Quantum atom-light interactions

In the following, the interaction of light with modes of the radiation field is outlined, which leads to well-known phenomena such as Rabi oscillations and the exponential decay of the atomic excited state. The system is visualised in Figure 4.1. An atom which is not coupled to any external fields is described by the Hamiltonian

$$H_A = \hbar\omega_{eg}|e\rangle\langle e|, \tag{4.1}$$

where the ket $|\ e\rangle$ denotes the excited state of the atom and the energy of the ground state has been arbitrarily set to zero. The light mode is a simple harmonic oscillator,

$$H_L = \hbar\omega_L(a^\dagger a + \frac{1}{2}). \tag{4.2}$$

The interaction between the atom and the light is

$$H_{int}^{full} = \hat{p}.\hat{A} \simeq \hat{d}.\hat{E} = g_{AL}(a + a^\dagger)(|e\rangle\langle g| + |g\rangle\langle e|)\,, \tag{4.3}$$

where the approximation is valid for frequencies ω_L close to the atomic resonance ω_{eg}. By switching briefly to the interaction picture at this point, it can be seen that

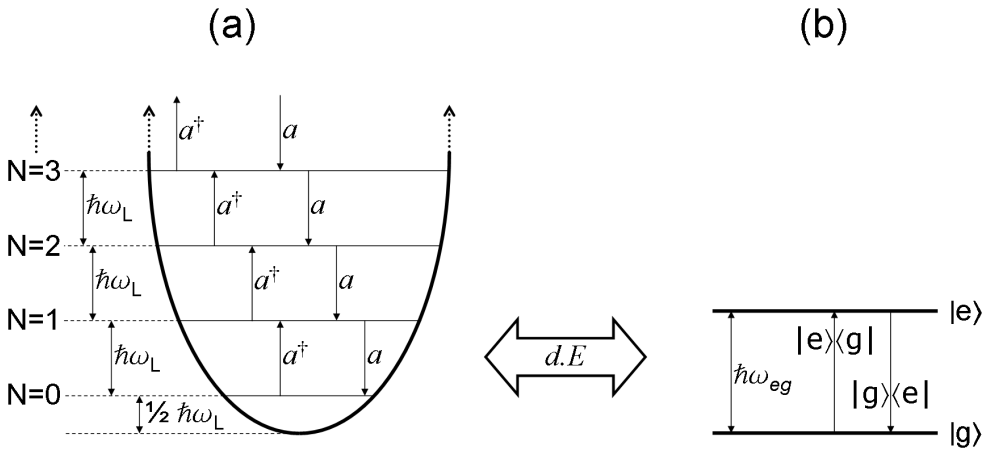

Figure 4.1: Schematic diagram of the system described by the Jaynes-Cummings model. The light field (a) is described as a quantum simple harmonic oscillator, while the atom (b) is assumed to be a closed two-level system. The two interact via the electric dipole interaction.

the terms $a|g\rangle\langle e|$ and $a^\dagger|e\rangle\langle g|$ oscillate at a frequency $\omega_{eg}+\omega_L$. Close to resonance, this will be much greater than that of the two other terms which oscillate at $\Delta_{AL} = \omega_{eg} - \omega_L$. In this limit, the fast-oscillating terms can therefore be neglected. This simplifying step is known as the Rotating Wave Approximation, and will be taken as valid throughout the rest of this thesis. The resulting, simplified interaction Hamiltonian is then:

$$H_{int} = \hbar g_{AL}(|e\rangle\langle g|a + a^\dagger|g\rangle\langle e|) \tag{4.4}$$

This is the famous Jaynes-Cummings Hamiltonian, where the frequency g_{AL} gives the interaction energy of the coupled atom-light system. It is known as the coupling rate or vacuum Rabi frequency of the system. The RMS electric field of the vacuum, $\mathcal{E}_{vac}$, can be found by integrating over the volume of the mode. Thus

$$\frac{\hbar\omega_{eg}}{2} = 2 \times \int \frac{1}{2}\epsilon_0 \mathcal{E}_{vac}^2 dV \qquad \mathcal{E}_{vac}(\omega_{eg}) = \sqrt{\frac{\hbar\omega_{eg}}{2\epsilon_0 V}} \tag{4.5}$$

The initial multiplication by 2 takes into account the equal contributions of electric and magnetic fields to the energy of the mode. For a transition with matrix element μ_{eg}, the interaction energy of the dipole coupling is given by $\vec{\mu}_{eg}.\vec{\mathcal{E}}$, so assuming the dipole is aligned with the field, the coupling frequency will result as

$$g_{AL} = \frac{|\vec{\mu}_{eg}||\vec{\mathcal{E}_{vac}}|}{\hbar} = \sqrt{\frac{\mu_{eg}^2\omega_L}{2\hbar\epsilon_0 V}}\,. \tag{4.6}$$

This gives us the complete Hamiltonian for a two-level atom interacting with a single radiation mode,

$$H = H_A + H_L + H_{int}\,. \tag{4.7}$$

By making the Rotating Wave Approximation in 4.4, only energy-conserving terms have been retained. Consequently, if we depict the system in a basis $|l, N\rangle$, where $l = g, e$ denotes the atomic level and N denotes the number of excitations in the radiation mode, the interaction term only couples states $|g, N\rangle$ to states $|e, N-1\rangle$ and vice-versa. Each such pair of states can therefore be treated as an independent 2-level system. In algebraic terms, the interaction matrix in this basis can be written as

	$\lvert g,0\rangle$	$\lvert e,0\rangle$	$\lvert g,1\rangle$	$\lvert e,1\rangle$	$\lvert g,2\rangle$	$\lvert e,2\rangle$	$\lvert g,3\rangle$	...	
$\langle g,0\rvert$	$\frac{1}{2}\omega_L$	0	0	0	0	0	0	...	
$\langle e,0\rvert$	0	$\frac{3}{2}\omega_L+\Delta$	g	0	0	0	0	...	
$\langle g,1\rvert$	0	g_{AL}	$\frac{3}{2}\omega_L$	0	0	0	0	...	
$\langle e,1\rvert$	0	0	0	$\frac{5}{2}\omega_L+\Delta$	$\sqrt{2}g_{AL}$	0	0	...	$\times\hbar$
$\langle g,2\rvert$	0	0	0	$\sqrt{2}g_{AL}$	$\frac{5}{2}\omega_L$	0	0	...	
$\langle e,2\rvert$	0	0	0	0	0	$\frac{7}{2}\omega_L+\Delta$	$\sqrt{3}g_{AL}$	...	
$\langle g,3\rvert$	0	0	0	0	0	$\sqrt{3}g_{AL}$	$\frac{7}{2}\omega_L$	...	
...	...	...	...	...	...	...	...	...	

The Hamiltonian for each pair of states $|g, N\rangle$, $|e, N-1\rangle$ can then be given by

$$H_{N\neq 0} = \hbar \begin{pmatrix} \left(N+\frac{1}{2}\right)\omega_L + \Delta & \sqrt{N}g_{AL} \\ \sqrt{N}g_{AL} & \left(N+\frac{1}{2}\right)\omega_L \end{pmatrix}. \tag{4.8}$$

The eigenfrequencies of the system are then

$$\omega^{\pm}_{N\neq 0} = \omega_L\left(N+\frac{1}{2}\right) + \frac{1}{2}\left(\Delta_L \pm \sqrt{4Ng_{AL}^2+\Delta_L^2}\right). \tag{4.9}$$

In words, the energy levels of the combined system are doublets on a ladder, apart from the case in which no excitation is present in the system. When $N = 0$, the system has only one eigenfrequency, $\hbar\omega_L/2$.

4.2 Many frequencies: Spontaneous emission

When the atom interacts with a single light mode, the excitation goes back and forth regularly between the field and the particle with an effective Rabi frequency of $\sqrt{4Ng_{AL}^2+\Delta_L^2}$. If instead there is a multitude of electromagnetic frequencies close to the atomic resonance, the same mechanism will apply separately for each as the

polarisation and frequency modes of the electromagnetic field are (by definition) orthogonal. Here, a brief summary is given of how this situation leads to the decay of the excited state of an atom. Recalling that the Hamiltonian for the atom interacting with a single radiation mode is $H = H_A + H_F(\omega) + H_{int}(\omega)$, the system with a set of modes of wavelengths ω is then described by

$$H = H_A + \sum_{\omega} H_F(\omega) + \sum_{\omega} H_{int}(\omega). \tag{4.10}$$

For simplicity it is assumed that in the initial state $\mid i\rangle$, the atom is entirely excited while no excitation is present in any light mode,

$$\mid i\rangle = \mid e, 000...000\rangle \,. \tag{4.11}$$

From the real world, it is known that the system will eventually evolve into a state in which the atom is entirely in its ground state and the excitation is spread over the modes of the field. It will therefore evolve into a superposition of final states $\mid f\rangle_m$ with frequency ω_m,

$$\mid f\rangle_m = \mid g, 000...1_m...000\rangle \,. \tag{4.12}$$

In the interaction picture, the evolution of the system can be described by the state vector

$$\mid \Psi(t)\rangle = c_i(t)e^{\mathrm{i}\omega_{eg}t} \mid i\rangle + \sum_m c_m(t)e^{-\mathrm{i}(\omega_{eg}-\omega_m)t} \mid f\rangle_m \,. \tag{4.13}$$

This gives the equations of motion

$$\dot{c}_i = -\mathrm{i}\sum_m g_{AL}(m)e^{\mathrm{i}(\omega_{eg}-\omega_m)t}c_m(t) \,, \;\; \dot{c}_m = -\mathrm{i}g^*_{AL}(m)e^{\mathrm{i}(\omega_{eg}-\omega_m)t}c_i(t), \tag{4.14}$$

so that

$$\dot{c}_i = -\sum_m |g_{AL}(m)|^2 \int_0^t e^{-\mathrm{i}(\omega_f-\omega)(t-t')}c_i(t') \,. \tag{4.15}$$

After some reasonable approximations initiated by Wigner and Weisskopf, the evolution of the system is given by the simpler differential equation

$$\dot{c}_i = -c_i(t)\sum_m |g_m|^2\pi\delta(\omega_{eg}-\omega_m), \tag{4.16}$$

which has a solution of the form

$$c_i(t) = c_i(0)e^{-\gamma t}, \quad \text{with} \quad \gamma = \pi\sum_m |g_m|^2\delta(\omega_{eg}-\omega_m). \tag{4.17}$$

This indicates that the amplitude of the state will decrease exponentially with a decay rate given by the constant γ, which is found as follows. The sum over the

coupling frequencies is evaluated most easily if the mode volume is assumed to be large, V$\gg \lambda^3$. Then the coupling strength to the vacuum can be found using the density of states per unit frequency at the atomic resonance,

$$D(\omega_{eg}) = \frac{\omega_{eg}^2 V}{\pi^2 c^3}, \tag{4.18}$$

and finding the squared electric field as previously,

$$\mathcal{E}_{vac}^2(\omega_{eg}) = \frac{\omega_{eg}}{2\hbar\epsilon_0 V}, \tag{4.19}$$

to evaluate the electric field strength at this frequency. Averaging over 3 coordinates for a randomly oriented dipole,

$$\gamma = \frac{1}{3}\frac{\mu_{eg}^2}{\hbar} D(\omega_{eg})\mathcal{E}_{vac}^2(\omega_{eg}) = \frac{\mu_{eg}^2\omega_{eg}^3}{6\pi c^3\hbar\epsilon_0}. \tag{4.20}$$

While this quantity is apparently independent of the chosen quantisation volume, it should be noted that this is due to the approximation of the sum to an integral justified by the choice of a 'large' box. In this limit, in crude terms, the vacuum field of each mode decreases with volume but the number of modes in its vicinity, i.e. the density of states, increases giving the independence. In microcavity experiments however, the modes can be made so sparse that the approximation is invalidated. It is nonetheless evident that the transition rate will depend on the strength of the vacuum field at the atomic frequency. The Hamiltonian of an atom in free space can now be re-written to include its natural decay rate as

$$H_A = \hbar\omega_{eg} \mid e\rangle\langle e \mid -i\hbar\gamma \mid e\rangle\langle e \mid . \tag{4.21}$$

4.3 Many photons: The semiclassical limit

Returning to the picture of a single mode coupled to the atom, if this mode is populated with a large number of photons, the system can be treated more succinctly by approximating the light to a classical, continuous variable. The atom is still treated as a quantum-mechanical two-level system. The interaction Hamiltonian in this approximation is given by

$$H_{int}^{SC} = \mu_{eg}\mathcal{E}(t)(|e\rangle\langle g| + |g\rangle\langle e|). \tag{4.22}$$

Neglecting the energy change in the light field, the total Hamiltonian is $H^{SC} = H_A + H_{int}^{SC}$, i.e.

$$H^{SC} = \hbar((\omega_{eg} - \Delta)|e\rangle\langle e| - \frac{\Omega}{2}|e\rangle\langle g| + \frac{\Omega}{2}|g\rangle\langle e|) - \mathrm{i}\hbar\gamma \mid e\rangle\langle e \mid, \tag{4.23}$$

where the Rabi frequency is defined as $\Omega = \mu_{eg}\mathcal{E}_0/\hbar$ for a wave $\mathcal{E}(t) = \mathcal{E}_0 cos(\omega_L t + \theta)$. Once again, the system displays two eigenfrequencies given by

$$\omega^{\pm} = \frac{1}{2}(\Delta \pm \sqrt{\Omega^2 + \Delta^2}). \tag{4.24}$$

The Hamiltonian 4.22 forms the starting point for the semi-classical theory of atom-light interactions which can treat the vast majority of laboratory systems commonly found in atomic physics. In the next Chapter, the semi-classical approximation will be used to calculate the interaction of atoms with strong cavity fields.

Chapter 5

Realistic atom-cavity interaction

Coupling an atom to the field of an optical resonator leads to intriguing consequences, described concisely by cavity quantum electrodynamics (CQED). In this Chapter, this combined system is described using the terminology from Chapter 4. The coupling of an atom to a lossy resonator is treated using the fully quantum-mechanical picture from Section 4.1,[3, 34] and in an approximate semi-classical treatment for the interaction with intense cavity fields.[20] In the last part of this Chapter, the coupling of atoms to a cavity under our experimental conditions is discussed in more detail.

5.1 The quantum cavity

In chapter 4, the interaction between an atom and an electromagnetic field was described in terms of the coupling of a two-level system to a single quantum harmonic oscillator. In this experiment, the oscillator is a single mode of the optical cavity. The size and shape of the cavity determine the properties of the electromagnetic field of its mode, ψ_C. In our cavity the relevant mode is a lowest-order Gaussian of waist w_C, as described in Chapter 2, and its mode volume is given by

$$V_C = \int_0^L \int_{-\infty}^{-\infty} \int_{-\infty}^{-\infty} |\psi_C|^2 dx dy dz = \frac{\pi}{4} w_C^2 L. \tag{5.1}$$

The maximum vacuum Rabi frequency of the cavity is therefore given by

$$g_{AC} = \sqrt{\frac{\mu_{eg}^2 \omega_C}{2\hbar\epsilon_0 V}} \simeq \sqrt{\frac{3c\lambda^2\gamma}{\pi w_C^2 L}}, \tag{5.2}$$

the latter being acceptable when $\omega_{eg}/\omega_C \simeq 1$, as assumed for the rotating-wave approximation. At any point $\vec{r}$ in the cavity, the vacuum Rabi frequency of the cavity mode is then given by $g(\vec{r}) = \psi_C(\vec{r}) g_{AC}$.

In a perfect (lossless) cavity, the supported modes are given by delta-functions in frequency-space. In the case of a real cavity with transmitting (and lossy) mirrors, the modes have a finite half-width of κ, as shown in Chapter 2. The Hamiltonian for the field used in the previous chapter is therefore inadequate for realistic experimental conditions and needs to be modified to include the amplitude decay rate κ such that

$$H_C = \hbar\omega_C \left(a^\dagger a + \frac{1}{2}\right) - \mathrm{i}\hbar\kappa a^\dagger a\,, \tag{5.3}$$

where ω_C is the angular frequency of the cavity field.

The atom will therefore interact with a 'coloured' vacuum in which modes with frequencies close to the resonances of the cavity are enhanced in comparison to free space, while all others are suppressed.

To observe the interaction of an atom with the field, the cavity is driven with a laser beam so that light impinges on the input mirror at a rate of J_{in} photons per second. Comparing the number of photons entering and leaving the cavity per round-trip leads to a circulating photon number of $N_{circ} = J_{in}T_1\eta^2\tau_{rt}/\xi^2$ on resonance. Here η^2 is the coupling efficiency between the guided fibre mode and the lowest-order Gaussian mode of the cavity. The amplitude pump rate ζ is then given by considering that in a steady state the loading rate will equal the loss rate, i.e. setting $\zeta^2 = N_{circ}\kappa^2$, giving an amplitude pump rate of

$$\zeta = \sqrt{\frac{J_{in}T_1\eta^2}{\tau_{rt}}}\,. \tag{5.4}$$

The pumping of the cavity field is then described by the Hamiltonian

$$H_P = \mathrm{i}\hbar\zeta(a^\dagger - a). \tag{5.5}$$

This realistic model of the cavity can now be used to adapt the ideal model from the previous chapter to actual experimental conditions.

5.2 Dissipative dynamics

Recalling that the amplitude of the upper-state population of a two-level system in free space will decay naturally with a rate of γ (Eq. 4.21), the pumped, decaying atom-cavity system is now governed by the Hamiltonian

$$H_{AC} = H_A + H_C + H_P + H_{int}\,, \tag{5.6}$$

where H_{int} is the Jaynes-Cummings Hamiltonian from Chapter 4. By following the same arguments as in the previous chapter, we can calculate the eigenfrequencies of the system. These are now modified by the decay rates to

$$\omega_N^{\pm} = \omega_C \left(N + \frac{1}{2} \right) + \tilde{\omega}_N^{\pm} \,, \tag{5.7}$$

with

$$\tilde{\omega}_N^{\pm} = \pm \tfrac{1}{2} \sqrt{4Ng^2 - (\gamma - \kappa)^2} - \tfrac{\mathrm{i}}{2}(\gamma + \kappa(2N-1)).$$

5.2.1 Quantum intra-cavity field

If the pump amplitude is sufficiently low, all states with more than one excitation can be neglected. This is the case if the atomic excitation probability is low, i.e. if $\zeta \ll g_{AC}$, and the decay rates outweigh the pump rate, $\zeta < (\kappa + \gamma)/2$.
In this case, the state vector can be approximated by

$$\mid \Psi(t)\rangle = c_e(t) \mid e,0\rangle + c_g(t) \mid g,1\rangle + c_0(t) \mid g,0\rangle. \tag{5.8}$$

Given that the pump rate is assumed to be small, the occupation of the unexcited state can be taken as constant, $c_0 \approx 1$. The equations of motion of this truncated system when the cavity is on resonance with the atom are then given by

$$\begin{aligned} \mathrm{i}\dot{c}_e &= -g_{AC} c_g + (\Delta_{CL} - \mathrm{i}\gamma) c_e, \\ \mathrm{i}\dot{c}_g &= -g_{AC} c_e + (\Delta_{CL} - \mathrm{i}\kappa) c_g + \mathrm{i}\zeta. \end{aligned} \tag{5.9}$$

Assuming that a steady state has been reached such that $\dot{c}_g = \dot{c}_e = 0$, the value of c_g gives the amplitude of the cavity light field in the limit of weak pumping:

$$c_g = \mathrm{i}\zeta \frac{(\Delta_{CL} - \mathrm{i}\gamma)}{g_{AC}^2 - (\Delta_{CL} - \mathrm{i}\kappa)(\Delta_{CL} - \mathrm{i}\gamma)} = \frac{\zeta}{\kappa} \frac{\kappa(\gamma - \mathrm{i}\Delta_{CL})}{(\Delta_{CL} - \tilde{\omega}_1^{+})(\Delta_{CL} - \tilde{\omega}_1^{-})} \tag{5.10}$$

leading to an expectation value of the number of circulating photons $N_{circ} = c_g^* c_g$. In essence, the empty-cavity resonance is split into a doublet whose peaks are shifted to $\tilde{\omega}_1^{\pm}$. On resonance, the expression reduces to

$$c_g^{res} = \frac{\zeta}{\kappa} \, \frac{1}{2C+1} = \frac{\zeta}{\kappa} \, \frac{1}{P} \,, \tag{5.11}$$

where the cooperativity parameter $C = g_{AC}^2 / 2\kappa\gamma$, and the Purcell factor $P = 2C + 1$ have been introduced. The significance of the latter will become clear in the following Section, where the evolution of the system is described assuming that the atom is in an excited state while no excitation is present in the cavity mode, and the system is not being driven by an external pump field ($\zeta = 0$).

5.2.2 Intra-cavity decay rate

For experiments leading to the generation of single photons in the cavity and their collection at the end of the fibre, we are interested in the rate at which atoms will emit photons into the cavity mode. Later in this section, the collection efficiency is deduced from the fibre-cavity coupling mechanism discussed in Chapter 2.
By following the ideas of Section 4.2, the decay rate into the cavity can be found by relatively straightforward means. For the free-space decay mechanism described in the previous Chapter, the atom was assumed to couple to a continuum of modes in a large box. For the cavity mode, no such approximations need to be made as the atom will in general be coupled to a single cavity mode. The frequency-dependence of the vacuum field strength in the cavity is quickly found recalling that the lineshape of the cavity is Lorentzian with a half-width κ, so that the normalised vacuum field function is given by

$$\mathcal{E}^2_{vac}(\Delta_{CL}) = \frac{1}{\pi\kappa}\frac{\kappa^2}{\kappa^2+\Delta^2_{CL}}\mathcal{E}^2_{vac}(0). \tag{5.12}$$

With this, as Eq. 4.20, the decay rate for a maximally-coupled atom is given by

$$\gamma_{cav} = \pi\frac{\mu^2_{eg}}{\hbar}\mathcal{E}^2_{vac}(\Delta_{AC}) = \frac{\mu^2_{eg}\mathcal{E}^2_{vac}(0)}{\hbar\kappa}\frac{\kappa^2}{\kappa^2+\Delta^2_{AC}} = \frac{g^2_{AC}}{\kappa}\frac{\kappa^2}{\kappa^2+\Delta^2_{AC}}. \tag{5.13}$$

Here the atomic resonance is chosen as the central frequency as a consequence of the $\delta-$function in Eq. 4.17. This expression is only valid when the cavity field amplitude decays faster than the time necessary for a re-excitation of the atom, i.e. $\kappa \gg g_{AC}$, so that the cavity field population can be neglected. Now the total decay rate of the atom's excited state can be found. The coupling of the atom to the modes of free space will be slightly decreased as the cavity 'obscures' part of these modes, replacing them with its own. However, the solid angle of our cavity is very much smaller than 4π, so the reduction of the free-space decay rate can be neglected. When the cavity is on resonance with the atomic transition, the total decay rate can then be written as

$$\gamma_{tot} = \gamma + \gamma_{cav} = \gamma(1+\frac{g^2_{AC}}{\kappa\gamma}) = \gamma P. \tag{5.14}$$

The same result is found when the evolution of the state vector 5.8 is calculated for the same set of approximations made herein, but the line of reasoning followed here was chosen to underline that the same principle governs both the free-space and the intra-cavity decay process.
Two important facts emerge from this last equation: Firstly, the resonant rate of emission into the cavity will increase with improving cooperativity, and can be

enhanced to surpass the atom's natural decay rate with high finesse and small mode volume. Secondly, the emission of photons into the cavity can be almost entirely suppressed by detuning the cavity from resonance, as the vacuum electric field of the cavity mode can be made to possess negligible amplitude at the atom's resonant frequency.

The rate of photon emission into the cavity is the first step in calculating the rate of photons collected by our cavity fibre. At this point, the reflection- and transmission limits from Chapter 2 yield two different results p_F^r and p_F^t for the probability of collecting a photon from the cavity in fibre. In the reflection limit, a photon can only be transmitted into the fibre or lost via the concave mirror, while in the transmission limit the light can also be lost to the cladding of the fibre. The probabilities for a photon in the cavity mode to enter the fibre mode are given in the two limits by

$$p_F^r = \frac{T_1^{h,v}}{T_1^{h,v} + (1-\rho_2)} = \left(1 + \frac{1-\rho_2}{1-\rho_1^{h,v}}\right)^{-1}$$

and

$$p_F^t = \frac{T_1^{h,v}}{T_1 + (1-\rho_2)} = \left(\frac{1}{\eta^2} + \frac{1-\rho_2}{1-\rho_1^{h,v}}\right)^{-1}. \tag{5.15}$$

For a measured contrast and finesse, the reflectivity of each mirror and the mode overlap must be calculated independently for the two limits with the equations listed in 2. It is nonetheless evident in both limits that for a high collection efficiency, it is desirable to create cavities with $\rho_1^{h,v} < \rho_2$. This demands good mode overlap and low reflectivity of the input mirror. Decreasing the reflectivity of the input mirror however also decreases the cooperativity of the atom-cavity system, and with it the decay rate into the cavity mode. Therefore if a high collection rate, given by $p_f \gamma_{cav}$, is desired rather than a high collection efficiency, the 'bare' reflectivity of the input mirror must be chosen to have the optimum value. The collection rate is plotted for a fixed reflectivity $\rho_2 = 99\,\%$ for mode overlaps $\eta^2 = 0.2$, 0.5 and 0.9. In the reflection limit the optimum value for the 'bare' input mirror reflectivity is $1 - (1-\rho_2)/\eta^2$, while in the transmission limit it is quite simply ρ_2, for all overlap values. In the reflection limit however, the maximum collection rate is independent of the mode overlap η and remains constant at $g_{AC}^2 L/c(1-\rho_2)$.

The equations given in this Section enable the calculation of upper and lower limits for the collection of photons in the cavity fibre if atoms within the cavity mode are prepared in an excited state, when the cavity pump amplitude is zero. The following section briefly discusses the opposite regime, namely one in which the pump amplitude is sufficiently large to justify a semi-classical treatment of the system.

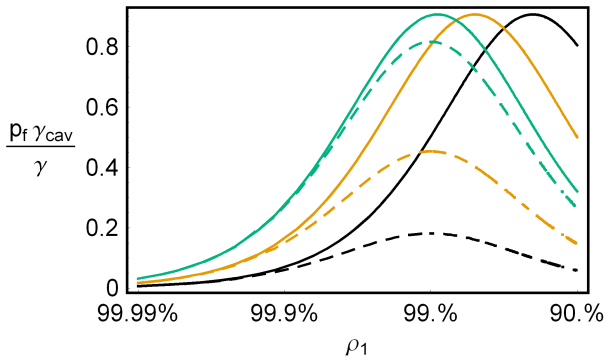

Figure 5.1: Collection rate of photons for a cavity tuned to the atomic resonance with mirror reflectivity $\rho_2 = 99\,\%$ as a function of input mirror reflectivity ρ_1. The rate, given in units of the atomic decay rate $\gamma = 2\pi \times 3\,\mathrm{MHz}$, is plotted for mode overlaps $\eta^2 = 0.2$ (black), 0.5 (orange) and 0.9 (green) in the reflection and transmission limits (solid and dashed lines, respectively). The atom-cavity coupling rate is set to $g_{AC}^2 = 2\pi \times 100\,\mathrm{MHz}$ and the cavity length is chosen as $130\,\mu\mathrm{m}$.

5.3 The coherent cavity field

As noted in the previous chapter, the cavity field can be approximated by a continuous, classical variable while the atom is still treated as a quantum two-level system. This allows analytical calculations in the regime where the excitation is large, as opposed to the purely quantum treatment given above. Including the cavity and atomic decay rates, the rate of change of the amplitude of the light field is given by

$$\dot{\alpha} = (\mathrm{i}\Delta_{CL} - \kappa)\alpha + g_{AC}\rho_{ge} + \zeta \tag{5.16}$$

while the atom's evolution is described by

$$\begin{aligned} \dot{\rho}_{eg} &= -(\gamma + \mathrm{i}\Delta_{AL})\rho_{eg} + g_{AC}\alpha^*(\rho_{gg} - \rho_{ee}), \\ \dot{\rho}_{ee} &= -2\gamma\rho_{ee} + g_{AC}(\alpha^*\rho_{eg} + \alpha\rho_{ge}). \end{aligned} \tag{5.17}$$

If a steady state is reached, the cavity light field is then given by

$$\alpha = \frac{\zeta}{(\kappa + \gamma\rho_{ee}/N) - \mathrm{i}(\Delta_{CL} - \Delta_{AL}\rho_{ee}/N)}, \tag{5.18}$$

where the mean number of photons $N = |\alpha|^2$, and ρ_{ee}, the excited-state population, is given by

$$\rho_{ee} = \frac{N g_{AC}^2}{\Delta_{AL}^2 + \gamma^2 + 2N g_{AC}^2}, \tag{5.19}$$

The two are interdependent, and yet some useful statements can be made about this system without resorting to numerical evaluations of the above equations. With the atom, pump laser and cavity all on resonance, the expression for the field amplitude reduces to

$$\alpha_{res} = \frac{\zeta}{\kappa}\frac{1 + 2Ng_{AC}^2/\gamma^2}{P + 2Ng_{AC}^2/\gamma^2}. \tag{5.20}$$

When the field amplitude is sufficiently low, that is when $N \ll \gamma^2/2g_{AC}^2$, the critical photon number, the simple expression from Eq. 5.11 re-emerges. In general however, the amplitude equation needs to be solved by more tedious means. Fortunately in this "all-resonant" case the field amplitude is always real, i.e. $N = \alpha_{res}^2$, as can be seen by inspecting equation 5.20, so the allowed values are easily found analytically by solving the cubic equation

$$\alpha_{res}^3 - \frac{\zeta}{\kappa}\alpha_{res}^2 + P\frac{\gamma^2}{2g_{AC}^2}\alpha_{res} - \frac{\zeta}{\kappa}\frac{\gamma^2}{2g_{AC}^2} = 0. \tag{5.21}$$

The lengthy expressions of the standard solutions to this equation can be found in mathematics reference books.[42] The properties of cubic equations and their determinants are however useful in determining if and where the system will have more than one real solution, i.e. become bi-stable.

The intra-cavity photon number is plotted for a variety of cooperativity values in Fig. 5.2. It can be shown straightforwardly that the field amplitude will remain single-valued for all pump values as long as $C \leq 4$, and will be given by the first of the three cubic solutions for α_{res}. For higher cooperativity values, the amplitude will have three allowed values for pump amplitudes in the regime between

$$\zeta_{\pm} = \frac{g_{AC}}{4}\sqrt{1 + \frac{10}{C} - \frac{2}{C^2} \pm \left(1 - \frac{4}{C}\right)^{2/3}}\ . \tag{5.22}$$

Now, the first cubic solution ceases to be real at a lower pump value and only the second cubic solution takes on real values in the regime between $\zeta_{1\to2} \leq \zeta \leq \zeta_{-}$, with

$$\zeta_{1\to2} = g_{AC}\sqrt{\frac{3P}{8C^2}}\ . \tag{5.23}$$

For increasing cooperativity values, the system becomes bi-stable at increasing pump values. The smallest pump value at which the system can become bi-stable therefore occurs when $C = 4$ and is

$$\zeta_{min} = \frac{3}{4}\sqrt{3\kappa\gamma}\ , \tag{5.24}$$

where for this cooperativity $\zeta_{min} = \zeta_{1\to2} = \zeta_{\pm}$. Limiting values for the bi-stable range can be found when any two of the three rates (g, κ, γ) are known.

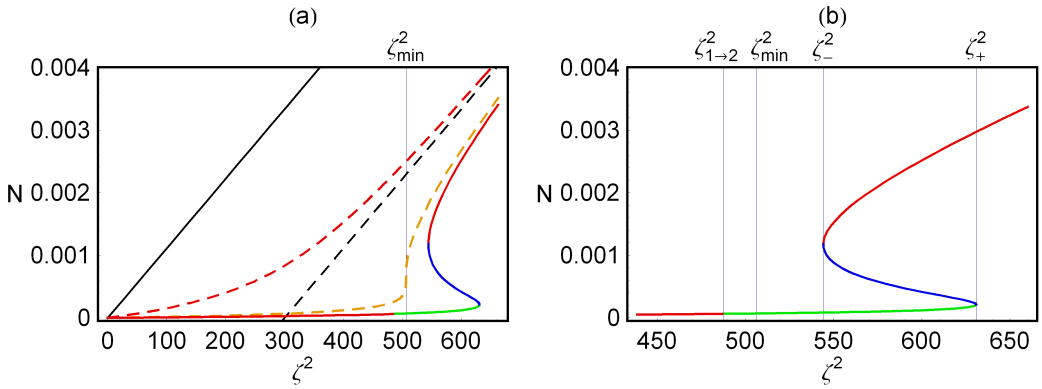

Figure 5.2: Intra-cavity photon number in the semi-classical approximation. For all plots, the decay rates are set to $\gamma = 1$ and $\kappa = 300$. (a) The cavity photon number for cooperativity values of $C = 1$ (dashed red), $C = 4$ (dashed orange) and $C = 6$ (solid multi-coloured line), compared to the empty-cavity photon number (solid black line line). With $C = 4$, the system is on the verge of bi-stability at ζ_{min} (see text). With $C = 6$, the system is visibly bi-stable. This case is shown in more detail in (b), where the solution boundaries given in the text are indicated. For $\zeta \to \infty$, all functions tend towards the dashed black line in (a) described by $N = (\zeta/\kappa)^2 - \gamma/\kappa$.

These equations now allow us to predict the resonant response of an atom-cavity system by entirely analytical means, for any coupling, decay and pump values. For the purposes of our experiment, we are particularly interested in how this response will become visible when we observe the light reflected by the resonator.

5.4 Cavity reflection signal

In Chapter 2, it was shown that the total reflected field A_R is the sum of an initial reflection from the input mirror and the light exiting the cavity through this mirror, i.e.

$$A_R = -A_{in} r_1^{h,v} + A_{cav} r_2 t_1^{h,v}. \tag{5.25}$$

Since we assume the losses in the input mirror to be negligible, the input mirror transmission depends on the mode overlap between fibre and cavity with $t_1^{h,v} = \eta_{h,v}\sqrt{1-\rho_1}$. In the initially reflected amplitude $A_{in} r_1^{h,v}$, $r_1^{h,v} = \sqrt{1-(t_1^{h,v})^2} = \sqrt{\rho_1^{h,v}}$, as defined in Chapter3. $A_{in} = \sqrt{J_{in}}$ is the time-averaged total field of the driving beam (in units of $\sqrt{photons/s}$). Although the cavity field $A_{cav} = \alpha_{cav}/\sqrt{\tau_{rt}}$ is fully described in the coherent limit by solving Equation 5.18, it is less cumbersome in the low-intensity limit to use the result of Equation 5.10, as the two are approximately equal in this regime. On resonance, this once again yields far simpler expressions than in the general case. For cavities of our type, using Eqs. 5.10 and 5.25, the reflected power on resonance becomes

$$J_R^{res} = |A_R|^2 = J_{in}\left(-r_1^{h,v} + \frac{r_2 T_1^{h,v}}{\xi}\frac{1}{P}\right)^2. \tag{5.26}$$

Here only the use of ρ_1 or $\rho_1^{h,v}$ within ξ needs to be chosen depending on whether the reflection or transmission limit is considered. As a simple example, the change in reflected power caused by the presence of a maximally coupled atom is plotted in Figure 5.3 (a) for a perfectly mode-matched cavity. The relative reflected power for the empty cavity is shown by the black line. To calculate the effect of an atom in the cavity, the coupling frequency is set to $g_{AC} = 2\pi \times 100\,\mathrm{MHz}$ and $\gamma = 2\pi \times 3\,\mathrm{MHz}$, while κ is calculated as a function of reflectivity assuming a cavity length of $130\,\mu$m. These yield a cooperativity C shown by the dashed orange line. The modified reflected power resulting from the presence of an atom is shown by the red line. Equation 5.26 can be simplified further if the visibility ϑ of the empty cavity is known. Then, given that $r_1^{h,v} \approx 1$ and $\vartheta = 1 - J_R^{res}/J_{in}$, the value of the

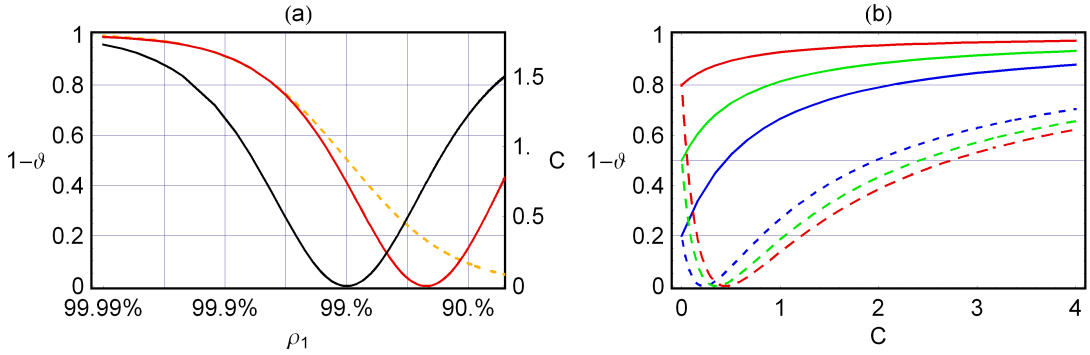

Figure 5.3: Effect of a maximally-coupled atom on the reflected power in the weak-pumping limit. The fibre-cavity coupling is assumed to be perfect. (a) The reflectivity of the input mirror ρ_1 is varied, while ρ_2 is fixed at 99%. The relative reflected power for the empty cavity is shown by the black line. To calculate the effect of an atom in the cavity in this case, the coupling frequency is set to $gAC = 2\pi \times 100$MHz and $\gamma = 2\pi \times 3$MHz, while κ is calculated as a function of reflectivity assuming a cavity length of 130 μm. These yield a cooperativity C shown by the dashed orange line. The modified reflected power resulting from the presence of an atom is shown by the red line. In (b) the reflected power is plotted as a function of cooperativity for empty-cavity relative reflected power values of $1 - \vartheta$ =0.8 (red), 0.5 (green) and 0.2 (blue). The solid (dashed) lines are plots for v^- (v^+).

fraction in Eq. 5.26 is given by

$$v \equiv \frac{r_2 T_1^{h,v}}{\xi} \simeq 1 \pm \sqrt{1-\vartheta} \equiv v^{\pm} \tag{5.27}$$

The minus-sign is therefore taken when the cavity is under-coupled, i.e. $r_1^{h,v} > v$, and the plus-sign for the over-coupled case $r_1^{h,v} < v$.[1] The simplified expression for the reflected light is then

$$J_R^{res} = J_{in}\left(-1 + \frac{v^{\pm}}{P}\right)^2. \tag{5.28}$$

The dependence of this function on cooperativity is shown in Figure 5.3 (b), where the relative reflected power is plotted for both over- and under-coupling, with initial values for $1-\vartheta$ of 0.2, 0.5 and 0.8. It is already clear that the presence of an atom in the cavity will, for increasing cooperativity, eventually extinguish the interference effect of the cavity, thereby bringing the reflected signal towards $J_{in}\rho_1$. However, if the reflectivity of the input mirror is lower than that of the opposing mirror, the reflected intensity will decrease to zero before it increases towards $J_{in}\rho_1$.

The difference between the empty-cavity signal and the signal with an atom in the cavity mode is one of the factors which determine how confidently the passage of an atom can be detected. A further important consideration is the pump rate, as this determines the shot noise of the measurement. The reflection signal for large pump rates can be calculated using the results from Section 5.3 with Eq. 5.25. The dependence on pump rate is shown in Figure 5.4, for cooperativity values of $C = 1$ (a) and $C = 6$ (b), for both under-coupled (solid line) and over-coupled (dashed line) resonators. In both graphs, it is clearly visible that saturation of the atom-cavity system due to the saturation of the atomic transition occurs earlier for over-coupled cavities. This is because the pump rate ζ increases with input-mirror transmission. Figure 5.4 also shows that increasing the pump power has a similar effect to decreasing the cooperativity of the atom-cavity system, once again because of the atomic saturation. For the detection of atoms, this means that the pump power must be chosen carefully so as to minimise the fractional shot noise of the measurement (high pump powers) while maintaining a large ratio between signal of the empty cavity and that caused by the presence of an atom in the resonator mode. Some considerations towards optimising the detection confidence are delineated in the following Section.

[1] For the sake of completeness it is noted that the initially reflected field $-A_{in}r_1^{h,v} \to -A_{in}r_1$ for high cooperativity close to resonance.

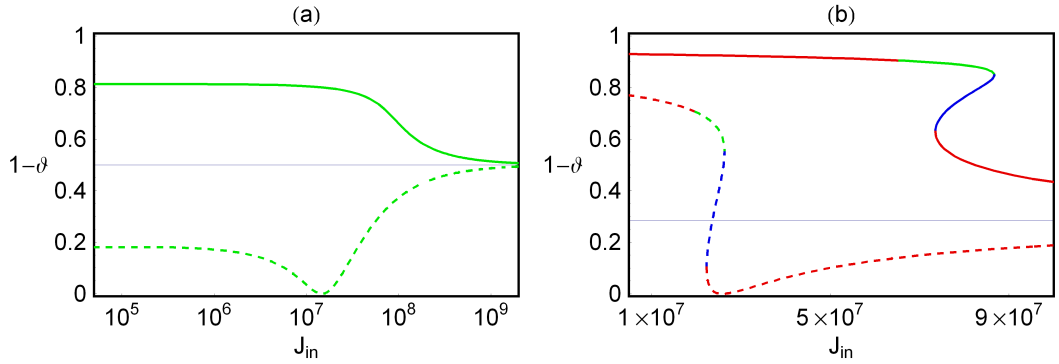

Figure 5.4: Relative reflected power in the semiclassical limit. In both graphs, the chosen cavity length is 130 μm and the coupling frequency $g_{AC} = 2\pi \times 100\,\mathrm{MHz}$ and the mode overlap between fibre and cavity is chosen to be perfect, i.e. $\eta^{h,v} = 1$. (a) Log-linear plots of the relative reflected power for a cooperativity $C \simeq 1$. Solid line: under-coupled case, $\rho_1 = 99.7\,\%$ and $\rho_2 = 98.4\,\%$. Dashed line: over-coupled case, $\rho_1 = 98.4\,\%$ and $\rho_2 = 99.7\,\%$. Both lines converge towards $1 - \vartheta = 0.5$ for high pumping rates as the losses caused by the atom become negligible. In the weak-pumping regime, the values tend towards those of the green lines in Fig. 5.3 (a) at a cooperativity of $C = 1$. (b) $C = 6$. Here the reflectivities are 99.77% and 99.93%.

5.5 Detection confidence

The results from the previous sections can now be used to get an idea of the certainty with which an atom can be detected. The light reflected from the cavity (with or without an atom) will here be assumed to be Poissonian. Then the probability of detecting a number of photons N during the integration time τ_{int} is

$$p_p(N, \tau_{int}, J) = \frac{e^{-J\tau_{int}}(J\tau_{int})^N}{N!}, \tag{5.29}$$

where J is the mean number of photons detected per second. For large $J\tau_{int}$ (30), this is approximately equal to a normal distribution with

$$p_n(N, \tau_{int}, J) = \frac{1}{\sqrt{2\pi J\tau_{int}}} Exp\left[-\left(\frac{N - J\tau_{int}}{\sqrt{2J\tau_{int}}}\right)^2\right]. \tag{5.30}$$

A number of different approaches can be taken to quantify the confidence of the detection of an atom in the cavity, with varying degrees of accuracy and computational simplicity. As both the empty-cavity and the atomic signals are Poissonian, the widths of both distributions should be taken into account as well as their separation. Any calculation involving the discrete Poissonian distribution will be cumbersome, and only leads to significantly different results when the mean number of photons is small, which is never the case for our measurements. So one could simply mke the normal-distribution approximation and ask how likely it is that an atom will cause a signal which is more than some number of standard deviations away from the empty-cavity mean. This is still computationally intense, as it involves the evaluation of error functions. It is not readily generalised, as it already implies a choice of confidence in the number of standard deviations. Another commonly used value is the signal-to-noise ratio, $SNR = |\sqrt{\tau_{int}}(J_0 - J_A)/\sqrt{J_A}|$. This value however neglects the variance of the empty-cavity signal. This could however be taken into account by using a pooled standard deviation in the denominator. Then a modified ratio can be defined as

$$SNR' = \sqrt{\tau_{int}}\frac{|J_0 - J_A|}{\sqrt{J_0 + J_A}}. \tag{5.31}$$

This is equal to the t-value from a "Student's t-test", used in significance testing in standard statistics, for a sample size of 1. An intuitive, generally applicable and easily calculable measure of confidence can be defined by calculating the normalised overlap integral of the two normal distributions. This calculation reveals instantly how different the empty-cavity output distribution is from that expected for the combined atom-cavity system:

$$\text{confidence}(J_0, J_A, \tau_{int}) = 1 - \sqrt{2\pi\tau_{int}(J_0 + J_A)} \int_{-\infty}^{+\infty} p_n(N, J_0, \tau_{int}) p_n(N, J_A, \tau_{int}) dN$$
$$= 1 - Exp[-SNR'^2/2]. \quad (5.32)$$

The normalisation is chosen to yield a confidence equal to zero for complete overlap of the two signals for equal likelihood, i.e. both probability functions in the convolution are normalised to have an integral of 1, but it can be modified to allow for unequal likelihood by an apposite modification of the normalisation. This measure of confidence is convenient as it is easy to calculate, is related in a simple way to the result of a t-test and gives an intuitively clear result. It ranges from 0 for identical distributions to 1 for vanishing overlap of the distributions. The detection confidence is shown for a variety of parameters in Fig. 5.5, following the results of the previous Sections of this Chapter. In 5.5 (a) and (b), the weak-pumping limit is considered for the same parameters as in Fig. 5.3 (a) and (b), with $J_{in}\tau_{int} = 30$. Figure 5.5 (c) shows the value for increasing power for the same parameters as in 5.4 (a). All in all, the plots confirm what could be expected from the previous Sections. It can be noted that there is no correspondence between (c) and the green lines in (a) because with the cavity parameters chosen for (c), the system is not weakly pumped at a rate of 30 photons/10 μs. In (b), it is visible that for a given concave-mirror reflectivity, there are two ranges of input-mirror reflectivity in which the detection confidence is high, one where $\rho_1 \simeq \rho_2$ and one in which $\rho_1 \ll \rho_2$. However, if both atom detection and a high photon collection rate are desired, then the former range is clearly preferable.

With the calculations in this chapter it is now possible to predict how the light collected from an atom-cavity system will behave for a large portion of the parameter space. Conversely, they also provide most of the tools necessary for the interpretation of the data gathered in our experiment, as will be done in Chapter 7. There, a number of further considerations such as the spatial variation of the cavity mode, the fibre-cavity coupling efficiency and the properties of the atomic cloud traversing the cavity will be included to refine and generalise the equations listed above. For a correct understanding of the experimental results it is therefore necessary to take into account the peculiarities of the microcavity used in the experiment, and the surrounding experimental setup. These are described in the following Chapter.

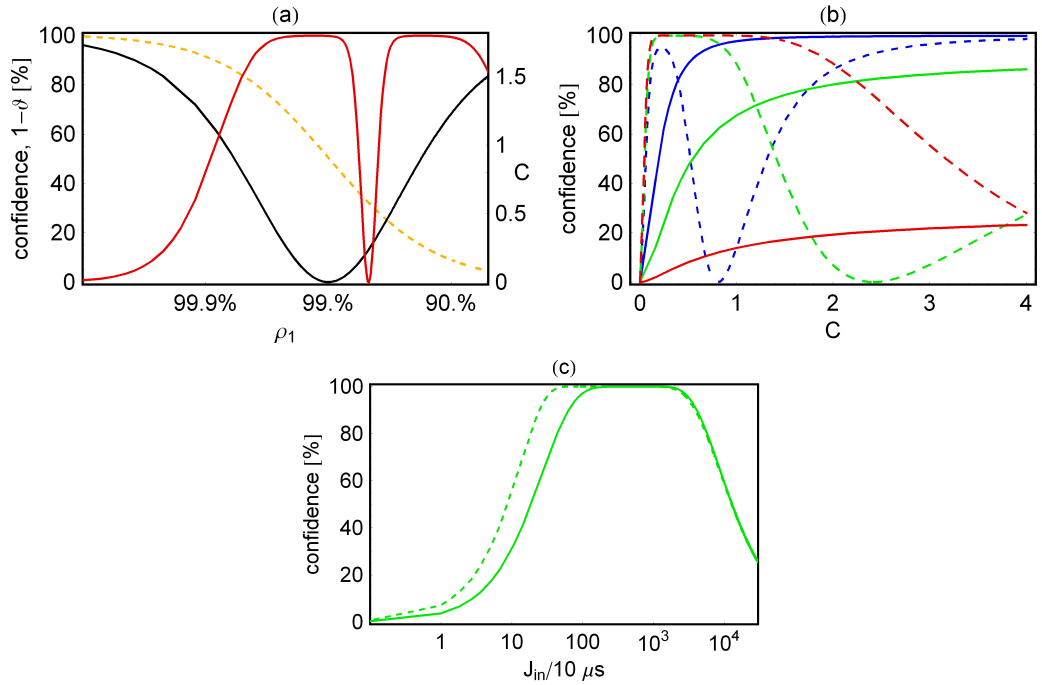

Figure 5.5: Atom-detection confidence for a variety of parameters. (a) and (b) show the behaviour for the same parameters as in Figure 5.3 (a) and (b), but assuming an rate of incident photons of $J_{in}\tau_{int} = 30$. In (a), The plots of cooperativity and empty-cavity visibility are repeated from from Figure 5.3 (a), while the red line now shows detection confidence rather than the modified reflection signal. In (b), each line shows the detection confidence for the line of the same colour as in Figure 5.3 (b). In (c), the detection confidence is plotted versus incident power for the parameters used in Figure 5.4 (a).

Chapter 6

Experimental Setup

The construction of the setup is outlined, as well as its peculiarities. The design of the current setup was geared towards ascertaining simply whether these microcavities could be implemented as as atom detectors. The setup does however allow for more advanced quantum optics experiments such as the generation of single photons by enhanced spontaneous emission.

6.1 Overview

The guiding principle behind the design is to release atoms into a microcavity from a MOT. Although the main aim of the setup is the detection of atoms, a further desired outcome was to detect photons generated by cavity-enhanced spontaneous emission. The magnitude of both signals increases with the density of atoms in the resonator. The intra-cavity density of a cloud of atoms released into free fall from a MOT decreases rapidly with dropping height, so that this height should be minimised. In a later stage, we intend to create a moving standing-wave dipole trap with an opposing beam. This will enable us to transport atoms from the MOT into the microcavity in a controlled manner.

The core of the setup is shown schematically in Figure 6.1 (a). The atoms are initially trapped in a reflection MOT on a gold-coated glass plate of thickness 1.5 mm. The magnetic field is provided by two coils with 60 turns each of 1-mm diameter wire. The four necessary beams are provided by a commercial fibre-coupled setup. From one linearly-polarised input beam, this delivers four beams of 2 cm ($1/e^2$-intensity) diameter, each with the required circular polarisation. The MOT is formed above a 1-mm diameter hole in the glass plate, through which the atoms fall to reach the microcavity. The glass plate is glued to a block of low-thermal-expansion quartz, to which all other components are also attached. The block itself

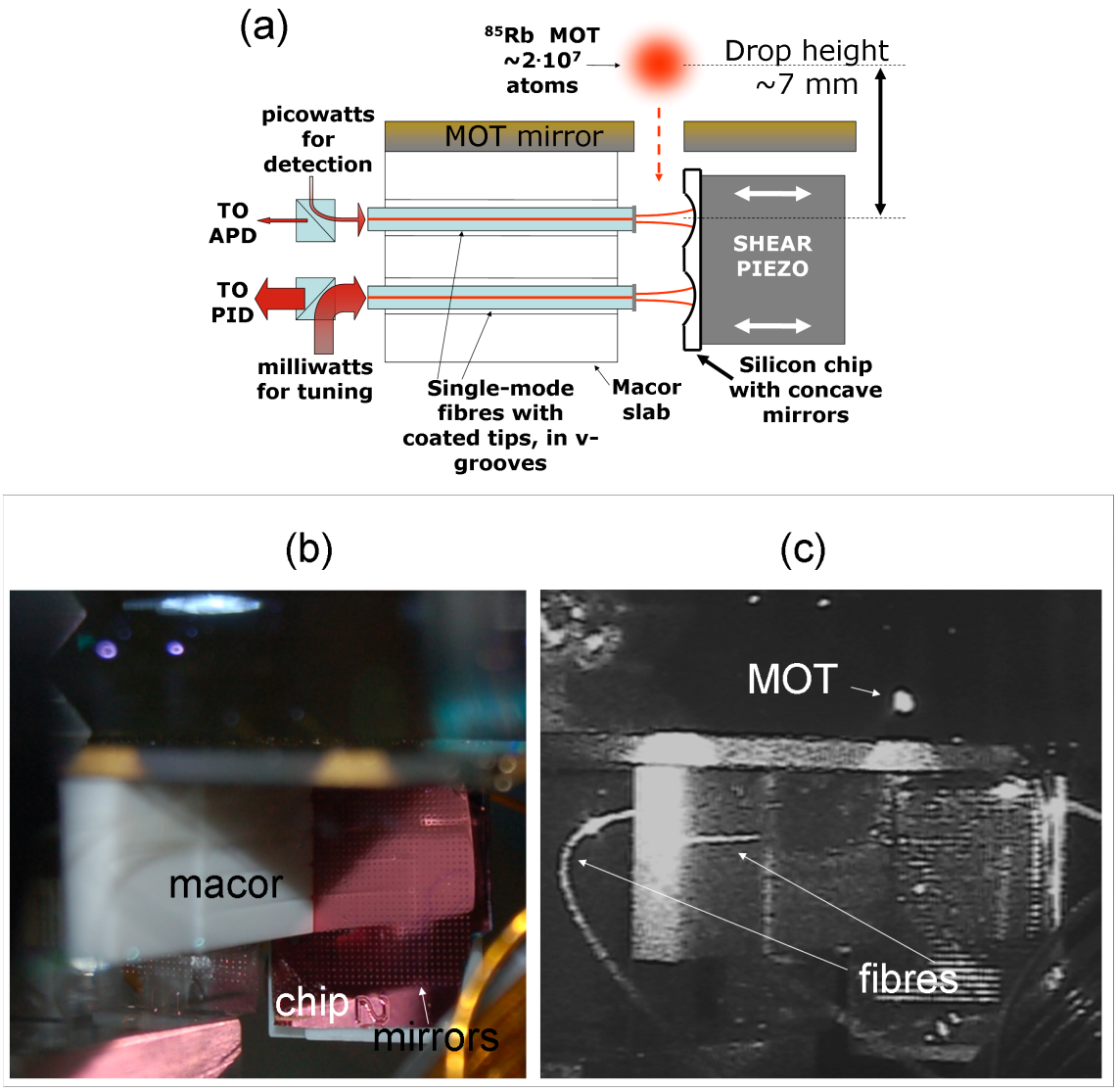

Figure 6.1: (a) The core of the setup consists of two microcavities into which a magneto-optically trapped and cooled cloud of Rubidium atoms is released under gravity. (b) Photograph of the core of the setup showing the Macor slab with v-grooves, and the etched, coated silicon chip. (c) Infrared photograph from a similar perspective showing the position of the MOT. The two fibres are also visible.

is glued into an aluminium support structure. The latter is screwed onto a flange of the vacuum chamber. The same flange also hosts the feed-throughs for fibres and wires. The fibre feed-through consists of a teflon cylinder with two 300 μm-diameter holes through which the fibres enter the vacuum chamber. This diameter is sufficient to accommodate fibres covered with a protective acrylate coating, which have a diameter of 250 μm. The cylinder is tapered at one end so as to fit into a Swagelok® feed-through. The latter is welded into the chamber flange and can be tightened to compress the teflon cylinder until it seals the holes around the fibres. This method is sufficiently airtight for pressure levels below 10^{-9} mBar. The entire setup was designed to fit through one 4.5"-flange opening (2.9"=73.7mm bore) of the vacuum chamber (Kimball 8 Multi-CF Spherical Square, model #:MCF800-SS2040400-A). The assembly of the setup is described in the following Section.

6.2 Setup properties and assembly

The experiment is built around the type of microcavity described in Chapter 3. As shown in Figure 6.1, there are two microcavities of the same type in the setup. The second microcavity can be used to tune the primary cavity as they are solidly connected. The fibres with the transferred dielectric tip-coating are glued into two v-grooves on a piece of Macor. The latter is attached to a block of low-thermal-expansion quartz. The silicon wafer into which the concave mirror forms are etched is the same one used to form the high-finesse microcavities mentioned in Chapter 3. This was the only chip available at the time as the fabrication facility at Southampton University was not operational. Although finesse values of over 6000 had been achieved with this type of microcavity, it was decided to lower this value to the order of 500 in order to improve the fringe visibility and relax the requirements on alignment and stabilisation. As illustrated in Chapter 3, the finesse and fringe visibility of the previous microcavity, built using the same chip, decreased with increasing cavity length. In the previous chapter it was however shown that to achieve both high photon-collection rates and atom-detection confidence, it is desirable to construct a cavity with high visibility and similar reflectivity for both mirrors. Furthermore, increasing the cavity length would also allow more atoms to interact with the cavity field, increasing the cooperativity and therefore the detection signal. The single-atom cooperativity increases with cavity length for a fixed waist size due to a decrease in the cavity decay rate $\kappa \propto 1/L$. Additionally, the waist of our cavities decreases with length when the cavity length is larger than

$R/2$, which further increases the cooperativity for longer cavities. Considering these points, a cavity length of $R/2 < L < R$ was chosen. For these reasons, a variety of fibre transfer-coatings with different reflectivity values were tested with this chip to create a resonator with high fringe visibility and acceptable finesse at a length of approximately 130 μm. Once the most suitable coating had been selected, the apparatus was constructed as follows.

1. **Cleaning:** All items except the cavity and fibres were cleaned using a standard ultrasound de-greasing procedure to ensure their vacuum compatibility. The silicon chip was de-greased manually on the backside and the edges, while the coated surface was left untouched to avoid damage.

2. **Gluing of substructures:** Most components of the setup were glued to form subunits at this stage. Bylapox (Byla 8725, no longer in production) two-component UHV-epoxy was used to join the parts, which were left to set in custom-made alignment holders for 24 hours. The piezo wires (Goodfellow, 0.5 mm diameter, polyimide-insulated) were glued to the piezo contact strips using UHV-compatible two-component conducting epoxy (EPO-TEK® H21D). The subunits and main construction steps are shown in Fig. 6.2.

3. **Screw-mounted parts:** As mentioned, the chip used herein was at the time the last remaining sample. To ensure that it could be removed in case of failure of other components or other undesirable eventualities, it was glued to a Macor carrier which was in turn screwed to another Macor carrier glued to the top of the shear piezo. It was understood that this type of construction would be more susceptible to misalignment and more sensitive to temperature fluctuations than a solidly-glued arrangement. In that original design, each pair of Macor parts joined by screws would have been replaced by a single low-thermal-expansion-glass block. However it was unavoidable at the time of construction to use a non-permanent attachment of the parts given that the lead time for a new batch of chips had been estimated at 6 months. Macor was chosen for its rigidity and low thermal expansion coefficient, but is a highly brittle material, so teflon washers were used to avoid cracking the carriers during mounting, as indicated in Fig. 6.2 (c). At this stage, the upper coil ring was also screwed to the chassis.

4. **Alignment setup:** The cavity-piezo subunit was mounted on two joined 2-axis angular alignment stages to allow for tilt, yaw and roll. The chassis subunit was mounted on an XYZ-alignment stage. Two further XYZ-alignment

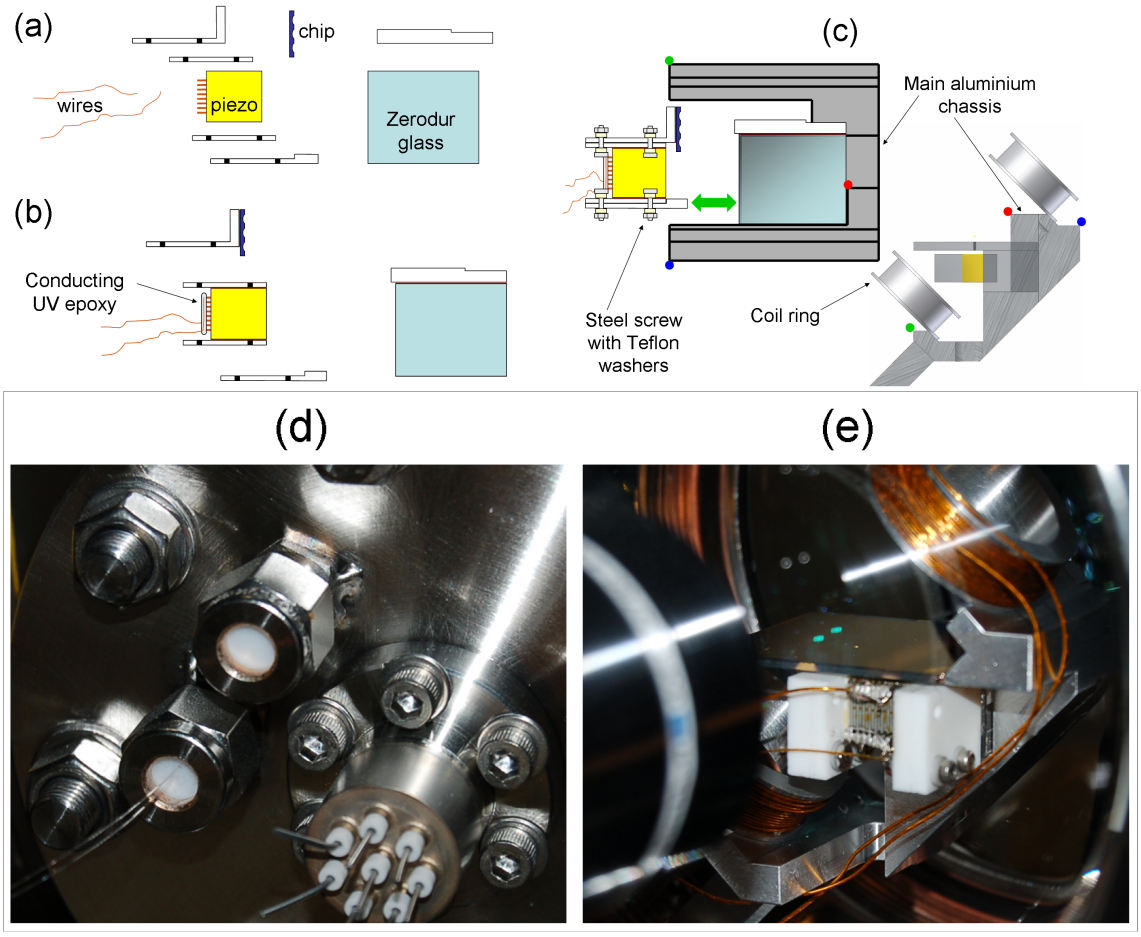

Figure 6.2: Principal components of the cavity setup, viewed from the top of the assembled setup (see text for details). In (a), all white parts are Macor slabs. Dark slots indicate holes for screws. In (b), the components glued together with Bylapox are shown joined. (c) shows the two fully assembled subunits, together with a simplified side view (from the left of this top view) of the full mount. Once the fibres had been prepared and the correct alignment found, the two subunits were glued at the surfaces indicated by the green arrow, and the MOT mirror glued onto the glass block. The red, green and blue dots are used to indicate the same corners in top- and side-views for the purpose of orientation. (d) shows the chamber flange with the electrical and fibre feedthroughs. A photograph of the setup from a similar perspective as in (c) is shown in (e).

stages with attached 2-axis angular alignment stages were set up to accommodate each fibre after coating.

5. **Fibre preparation:** Once the sub-components had been assembled, the two fibres (Fibrecore SM-750 ruggedised, with FC-APC connectors) from which 70 cm of rubber tubing and Kevlar strands had been removed to leave only the acrylate coating, were de-greased by wiping with acetone, passed through the Teflon-Swagelok-feedthroughs, cleaved and coated one after the other using the transfer-coating procedure described in Chapter 3.

6. **Cavities:** Both fibres were brought into position in the v-grooves on the macor support slab, and tested for suitability by scanning the piezo to observe fringes. This required a considerable amount of alignment in all 15 degrees of freedom of the chassis-subunit, both fibres and the piezo-chip subunit to ensure that both cavities had high-visibility fringes. Once a suitable pair of concave mirrors was found, the first fibre was glued into position using UV-curing glue. The fibre for the second cavity was glued into position subsequently after minimal re-alignment of all parts. Once the second fibre had been glued into place, the two subunits were glued together at the surfaces indicated by the green arrow in Fig. 6.2 (c) using UV-curing glue once again. The only purpose of this bond was to provide additional firmness to the alignment during the curing process of the Bylapox glue which was applied immediately afterwards. Small amounts of Bylapox were also distributed over the fibres to strengthen their adhesion to the Macor support slab. The upper microcavity was measured at this point to have a finesse of $F = 555 \pm 47$ and a visibility $\vartheta = (87 \pm 2)\,\%$, and the lower cavity displayed similar quality.

7. **Final assembly:** The second coil was screwed to the chassis; The gold-coated glass plate (MOT mirror) was glued to the Zerodur block; The now-complete chassis was attached to the flange via an aluminium post, bringing the design-position of the MOT at 3 mm above the hole in the MOT mirror to coincide with the centre of the vacuum chamber; All electrical connections (coils, dispenser and piezo) inside the chamber were made. The last addition to the setup was the Rubidium dispenser. These devices are highly sensitive to air exposure so it was mounted last to keep the exposure time to a minimum. The complete setup was then inserted into the vacuum chamber and bolted in.

   At this stage, the cavities were checked to ascertain whether the remaining

steps of the construction had caused a change in performance. This was indeed so, and the fringes were barely visible. Gentle manual re-alignment made the fringes reappear, but the re-alignment was kept to a minimum in order to avoid damaging the setup before even performing any measurements. The cavity was then measured to have $F = 280 \pm 30$, $\vartheta = (44.8 \pm 2.7)\%$, but it is reasonable to believe that further re-alignment will bring it closer it to its original quality.

8. **Pumping:** Following standard procedure, the chamber was then pumped down using a turbo-pump until the pressure reached 10^{-6} mBar. Then the ion pump (Varian: Vacion 20 Diode, with Minima controller) was switched on, and the chamber sealed off from the turbo pump using a gate valve. The chamber was left to evacuate until a pressure of 10^{-8} mBar was reached. The coils were then out-gassed as usual by running increasing amounts of current for increasing durations, until the pressure showed no significant change over 30 minutes when the coils were run with their operating current of 1.6 A. The chamber has since then reached and maintained a pressure of $< 10^{-9}$ mBar, which is the lower readout limit of the controller.

6.3 Microcavity properties

The cavity length and radius of curvature were determined using two lasers, one stabilised at $\lambda_0 = 779.95$ nm (locked to the ^{85}Rb re-pump transition) and one which was tuned to a variety of values. Using the equations from Chapter 2 is possible to determine the approximate cavity length from the dependence of the separation between the lowest-order fringes on the wavelength of the two lasers, by using the relation

$$\begin{aligned}\Delta L_{i,0,0} &= \tfrac{\lambda_i}{2}\left[q_i + \tfrac{1}{\pi}\arccos\left(\sqrt{G_2}\right)\right] - \tfrac{\lambda_0}{2}\left[q_0 + \tfrac{1}{\pi}\arccos\left(\sqrt{G_2}\right)\right] \\ &\approx \frac{\lambda_i q_i - \lambda_0 q_0}{2},\end{aligned} \tag{6.1}$$

where it is assumed that $q_{0,i} \gg 1$ and $\lambda_0 \approx \lambda_i$. Given that $L \simeq \lambda_0 q_0/2$ is constant for all q_i,the cavity length is

$$L \approx \frac{\lambda_i q_i}{2} - \Delta L_{i,0,0} \tag{6.2}$$

If only one fringe of the tunable laser lies between the first and second fringes of the fixed wavelength, i.e. $\mathrm{q}_0\lambda_0 < q_i\lambda_i < (q_0+1)\lambda_0$, then $q_i = \lceil q_0\lambda_0/\lambda_i \rceil$. Then the approximate cavity length can be found by a least-squares fit, which for all

three fringe sets in the recorded traces indicates that $q_0 = 341$. This remains true even when the entire possible range of values of the *arccos*-term is explored, so $L_{est} = 133\,\mu$m. This 'estimated' value is sufficiently accurate to determine the cavity waist and decay rate as needed for our purposes, but of course it is possible to solve Equation 6.1 more accurately by including low-order terms of the neglected parts, or by using numerical methods.

The concave-mirror radius is then determined by measuring the fractional separation of the radial fringes from the fundamental fringes for each wavelength. This yields a radius of $R = (185 \pm 3)\,\mu$m. Re-inserting this value together with the estimated length and the calculated longitudinal mode index $q_0 = 341$ into the original equation from Chapter 2 gives a cavity length of $L = (133.1071 \pm 0.0016)\,\mu$m. A numerical solution using only R and q_0 gives a length greater by 0.1 nm. While this level of accuracy is not required, given that the cavity expands over 5-10 fringes when the MOT-coils heat up, the method will be useful in cavity generations to come, and at least gives one fixed cornerstone for the less accurately determined quantities in this experiment. Furthermore, the finesse of the cavity can also be determined more accurately by this method.

As no astigmatism was observed on this mirror, the cavity waist is $w_C = (4.54 \pm 0.06)\,\mu$m, which together with the length gives a mode volume $\mathrm{V}{=}\pi w_0^2 L/4 = 2.15 \times 10^{-15}\mathrm{m}^3$. This gives a maximum atom-cavity coupling frequency of $g_{AC} = 2\pi \times (100.0 \pm 1.3)\,$MHz. The finesse of the cavity was measured at $F = 280 \pm 30$, giving a cavity decay rate of $\kappa = 2\pi \times (2.01 \pm 0.11)\,$GHz. The expected maximum single-atom cooperativity is then $C_{max} = 0.8$.

The cavity length, together with the finesse and visibility before and after misalignment, allow an estimate of the two mirror reflectivities. It is herein assumed that the cavity length did not change by a significant fraction of R in the course of the misalignment. This assumption is consistent with the (less precise) measurement of the original cavity length based on the radial fringe positions. Then, assuming that the alignment was originally close to perfect, the values for ρ_1 and ρ_2 before misalignment can be found by using the relations from Chapter 2. The 'bare' reflectivity of the input mirror should not be affected by the misalignment, so the change in finesse and visibility allows the calculation of the transverse misalignment of the fibre mode with respect to the cavity mode, as well as the decrease in reflectivity of the concave mirror due to increased aperture- and roughness losses. It is therefore possible to calculate the range for the reflectivities ρ_1, ρ_2 and the coupling η^2 before and after the misalignment. These values are tabulated below for reference.

parameter	before	after
F	555±47	280±30
ϑ	(82±1)%	(44.8±2.7)%
reflection limit		
ρ_1	(99.57±0.05)%	same
ρ_1^{eff}	(99.67±0.04)%	(99.71±0.04)%
η^2	75.8%	(68±7)%
ρ_2	(99.19±0.08)%	(98.05±0.21)%
transmission limit		
ρ_1	(99.57±0.05)%	same
ρ_1^{eff}	(99.67±0.04)%	(99.71±0.04)%
η^2	75.8%	(68±7)%
ρ_2	(99.31±0.05)%	(98.2±0.3)%

These values indicate that the most damaging effect of the misalignment was to lead to a reduction of the concave-mirror reflectivity, ρ_2. This may be due to aperture losses, if the spot of the cavity mode was shifted towards the edge of the mirror, or to an increase of the scattering loss if the spot was shifted to a rougher part of the concave mirror.

6.4 The MOT

The MOT for this experiment was designed to achieve the highest possible density of atoms in the cavity mode in the shortest possible time. While the inclusion of more elaborate loading schemes, using dipole-force and magnetic guides or atomic beams were foreseen for the future of the setup, gravity was chosen as the transport mechanism for these preliminary experiments as it is readily available. The MOT was therefore placed above the optical cavities. A mirror-MOT configuration was chosen as it involves the smallest amount of glass machining, and a vast amount of experience with this configuration had been accrued on other experiments within CCM. Furthermore, it allows the MOT to be closer to the cavity mode than a six-beam MOT with the same beam diameters. The required optical setup is less simple than that of a pyramid MOT, for which only one, circularly polarised beam is necessary, but simpler than the six beams needed for a traditional MOT setup. To avoid this complication, a commercial setup (Fiber Port Cluster 1 to 4 for 780 nm, Schäfter+Kirchhoff GmbH) was purchased which requires only one linearly polarised input beam to produce all necessary trapping beams. This beam is coupled

into a polarisation-maintaining single-mode fibre feeding into an enclosed, modular set of $\lambda/2-$waveplates and polarising beamsplitters, where it is split into four equal beams. Each beam is then coupled into a further single-mode, polarisation-maintaining fibre which leads to a beam expander. Each expander contains a $\lambda/2$-waveplate and a telescope setup to create a circularly polarised Gaussian beam with a $1/e^2$-intensity diameter of 2 cm. For an input power of 50 mW measured before the first fibre, the maximum power achieved at the output of each expander was 4.5 mW. This relatively low throughput-efficiency of 36 % can possibly be improved by better input mode-matching, but is in any event a small price to pay for the ease of implementation of the device. The device is furthermore extremely compact compared to most self-built MOT-beam setups. The fibre-coupled beam expanders are also practical as it is possible to mount them on the same carrier structure as the pump and chamber. It is therefore undoubtedly recommendable to consider this option for future experiments. The trapping light for the MOT was provided by a high-power multimode diode laser locked to the ($5^2S_{1/2}$, F=3 - $5^2P_{3/2}$, F=4)-transition by a DAVLL scheme. This light was referenced to a master laser (locked to polarisation spectroscopy) by monitoring a beat note between the lasers on a photodiode with a frequency counter. The re-pump light was provided by a single-mode diode laser locked to the ($5^2S_{1/2}$, F=2 - $5^2P_{3/2}$, F=3)-transition using polarisation spectroscopy. The re-pump light was brought to the trap via a separate fibre.

The MOT achieved after two days of optimisation is shown in Fig. 6.3 (a). The cloud shown in the image consists of 2.2×10^7 ^{85}Rb-atoms. In the region close to the maximum density of atoms, the spatial density profile is well-approximated by a Gaussian with radius $\sigma \simeq 860\,\mu$m.

Once the number of trapped atoms has reached its steady-state value, the atoms are cooled further in a molasses stage with a duration of 10 ms. Here, the magnetic field is switched off and the trapping beams are red-detuned further to -40 MHz. After this stage, the expansion of the cloud with time was measured to estimate the temperature of the atoms falling into the cavity. This was done by releasing the atoms for 10 ms in the dark and then measuring the size of the expanded cloud. This was found to be $\sigma \simeq 1.27$ mm, signifying a temperature of $T < 90\,\mu$K. The temperature value is however only an estimate of the upper limit of this value, since the profile of the cloud before cooling is only approximately Gaussian, and the expansion during the molasses stage is considered negligible.

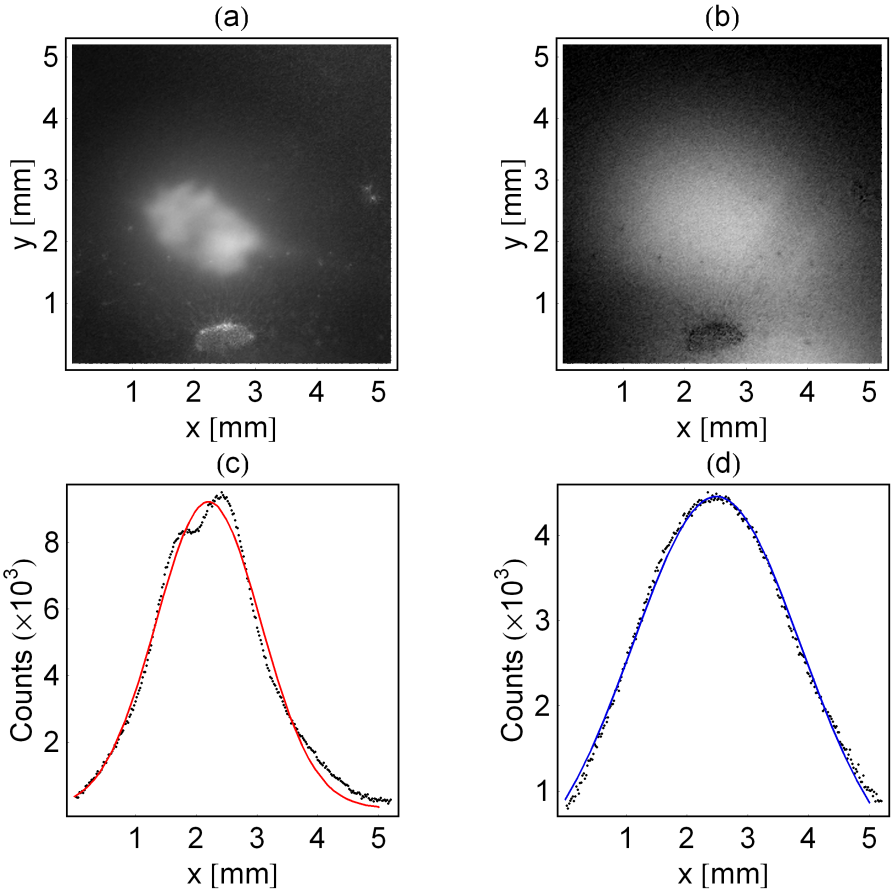

Figure 6.3: Images of the magneto-optically trapped atom cloud. (a) shows the unexpanded cloud, while (b) shows the cloud after a 10-ms molasses stage followed by 10 ms of expansion. The background has been subtracted from this brightened image. The oval shape near the bottom of each image is the circular hole in the MOT-mirror through which the cloud passes to reach the microcavity. Summation over the horizontal lines reveals an approximately Gaussian density profile for the unexpanded cloud (after background subtraction), shown in (c), and a near-perfect Gaussian profile for the cooled, expanded cloud in (d). The solid lines indicate Gaussian fits. The summation in (c) begins with the horizontal line at $y = 1\,\mathrm{mm}$, while in (d) only lines above $y = 2.1\,\mathrm{mm}$ are summed to avoid the image of the cloud reflected in the MOT mirror.

6.5 Expected number of atoms in the cavity

From the measured atom number, cloud radius and cloud temperature it is possible to estimate the maximum atom density which can be expected when the cloud reaches the cavity. A MOT with a Gaussian energy distribution with mean temperature T, and a Gaussian density profile with an initial radius σ_0, will expand during its fall through a height h to a radius of

$$\sigma(h) = \sqrt{\sigma_0^2 + \frac{k_B T}{m} \times t_{fall}^2} = \sqrt{\sigma_0^2 + \frac{2k_B T}{mg} \times h} \; . \tag{6.3}$$

Here $g = 9.81\,\mathrm{m/s^2}$ is the gravitational constant, $m = 1.41 \times 10^{-25}\,\mathrm{kg}$ is the mass of a ^{85}Rb atom and $t_{fall} = \sqrt{2h/g}$ is the duration of the fall. Two assumptions can now be made to find a simple relationship, namely that the expansion is slow compared to the time it takes the cloud to traverse the cavity, and that the initial cloud volume is much smaller than the expanded size so that it can be neglected. These approximations lead to inaccuracies of opposite effect and similar magnitude in our regime. The peak density for a cloud with N_A atoms is then given approximately by

$$D_{max} \approx N_A \left(\frac{2}{\pi \sigma^2(h)} \right)^{3/2} \approx N_A \left(\frac{mg}{\pi k_B T h} \right)^{3/2} . \tag{6.4}$$

For the values given above, and assuming a MOT height of 7 mm from the cavity, this results in a maximum density of $D_{max} \approx 2.5 \times 10^{14}/\mathrm{m^3}$. While this number may sound large, the number of atoms in the minute cavity mode volume $V = 2.15 \times 10^{-15}\,\mathrm{m^3}$ is only $D_{max}V \approx 0.54$. Given the approximations made here and in the MOT-temperature measurement, this must also be considered a lower bound. The total cooperativity of the system $C(N_A) = \sum_{n=1}^{N_A} g_{AC}^2(\vec{r}_n)/\kappa\gamma$ depends on the position $\vec{r}_n$ of each atom in the cavity mode, and on the alignment of its magnetic dipole with respect to the polarisation of the pump light. Both these factors lead in general to a total cooperativity $C(N_A) < N_A \times C_{max}$. These points will be discussed further in Appendix C.

6.6 The Detector

The choice of detector was based on the desire to measure both a change in the reflection signal of the cavity during the passage of atoms and the collection of photons from the cavity-enhanced spontaneous emission process. The detector selected for this purpose is a Perkin-Elmer SPCM-AQR-15 avalanche photodiode (APD). The photodiode sends out a 5V TTL signal each time a photon is detected. These

pulses are then collected by the National Instruments I/O computer interface. The photodiode is stated to have a dark-count rate of $< 100\,\text{counts/s}$, a typical dead time of $\tau_D = 50\,\text{ns}$ and a quantum efficiency of $\eta_Q = 60\,\%$ at $\lambda = 780\,\text{nm}$. The dead time is an important parameter for our reflection measurements as it gives the saturation curve of the photodiode in the range used for our measurements. It was therefore measured by observing the ratio of the variance σ^2_{Det} to the mean number of detected photons N_{Det} per integration time τ_{int}, for a range of count rates, as shown in Fig. 6.4. For detectors of our type this gives a dependence

$$\frac{\sigma^2_{Det}}{N_{Det}} = \left(1 + \frac{N_{Det}\tau_D}{\tau_{int} - N_{Det}\tau_D}\right)^{-2} \quad \text{or} \quad \tau_D = \tau_{int}\frac{1 + \sigma_{Det}/\sqrt{N_{Det}}}{N_{Det}}\,. \tag{6.5}$$

From the variation of the variance-to-mean ratio, a dead time of $\tau_D = 44\,\text{ns}$ was calculated. For count rates greater than $5 \times 10^6/\text{s}$, this dead time is expected to increase due to self-heating, according to the manufacturer, but no significant deviation from the original trend is visible in our measurements even at higher count rates (see Fig. 6.4 (a)). The dark time and quantum efficiency lead to a dependence of the detected counts on the true number N_{true} of incoming photons per integration time which, as stated in the photodiode manual, is given by

$$N_{Det} = \frac{\eta_Q N_{true}}{1 + N_{true}\tau_D/\tau_{int}} \tag{6.6}$$

This dependence is shown as a red line in Fig. 6.4 (b). The photodiode counts are evaluated by the computer control unit both to measure the absorption and fluorescence of atoms in the cavity, and for the stabilisation of the cavity length by an iterative algorithm. This stabilisation method is able to counteract slow drift and to correct slowly for short disruptions such as those caused by shutter noise. However the iteration steps have a duration of 100 ms, so that enduring acoustic noise cannot be handled by this method. A more elaborate stabilisation scheme will be implemented to counteract vibrations at these higher frequencies.

6.7 Setup summary

Now that the relevant features of the main components have been listed, an overview of these components is given in the context of the full experiment in Figure 6.5, where a highly simplified diagram of the setup is shown. The output beams of the MOT and reference lasers can be blocked by shutters 1 and 2. These are home-made shutters made from tweeter speakers to which a plastic lip is attached, and can be opened and shut with a 5V signal from the computer control. The reference

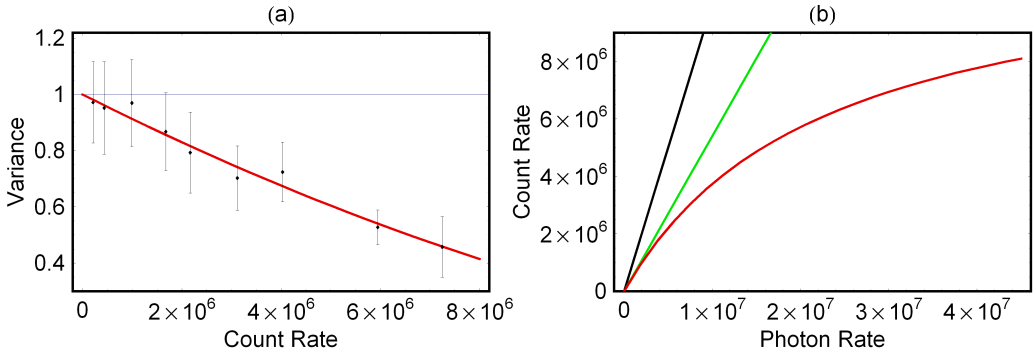

Figure 6.4: (a) Measurement of the APD dead time by the dependence of the variance -to-mean ratio on the mean number of detected photons. The red line shows the least-squares fit indicating a dead time of 44 ns. (b) shows the detected photon rate as a function of the rate of photons exiting the cavity fibre. Perfect detection (1photon = 1 click) is shown as a black line. The green line takes into account 10% losses at the APD beamsplitter and the quantum efficiency of 60%. The red line includes the measured dead time of the detector.

laser and re-pump laser are combined at a beamsplitter and focussed into a fibre to drive the atoms in the cavity from the side. This combined beam is controlled with a commercial shutter (Newport Oriel 76992 200 Hz, 6 mm Aperture Shutter, 0.5 ms rise-time, with 76995 Shutter Controller). All fibre couplers shown in green are Thorlabs F240APC-B couplers with a specified output $1/e^2-$beam waist of 0.74 mm.

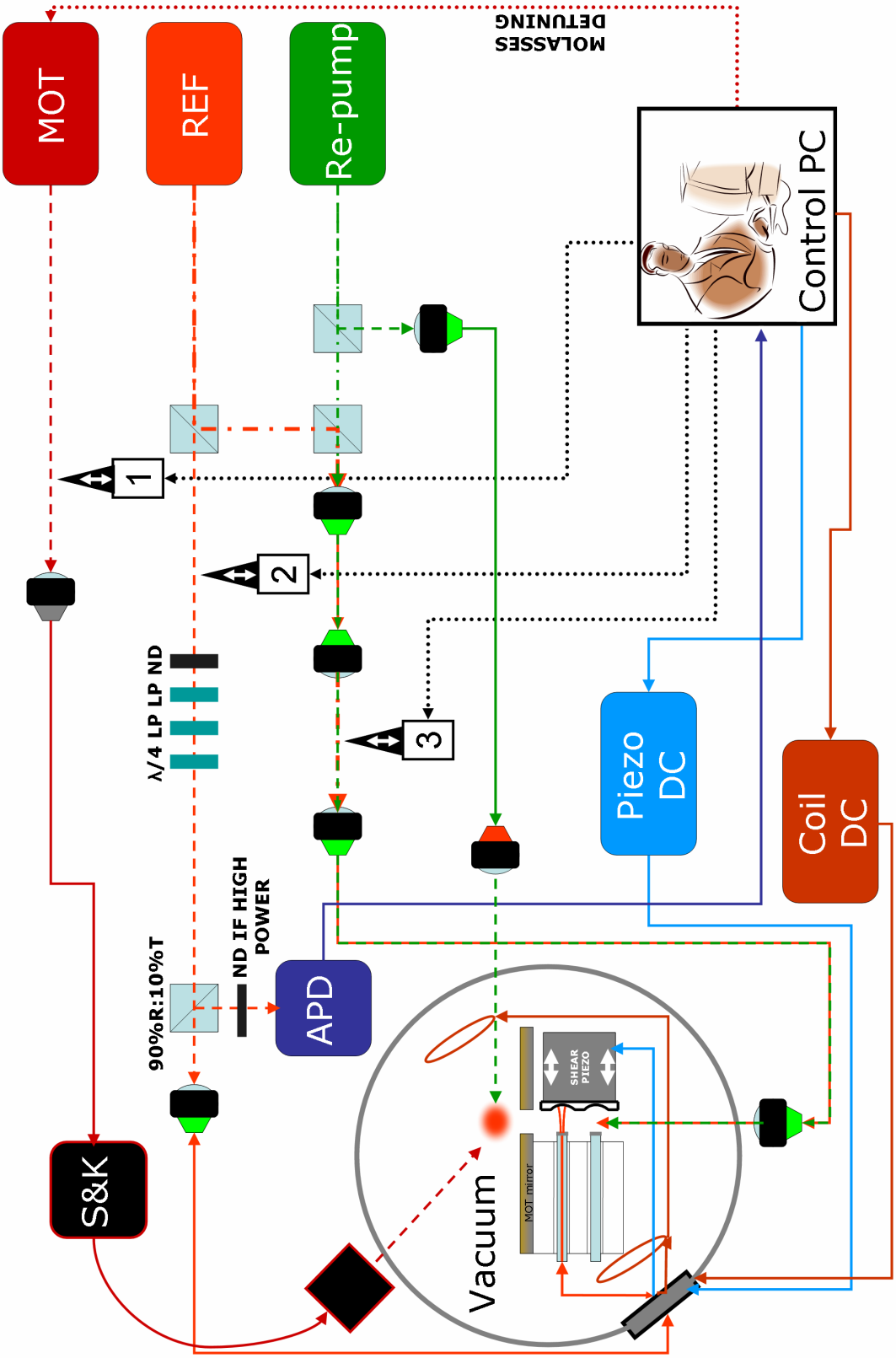

Figure 6.5: Principal components of the full setup. LP: linear polariser; ND: neutral-density filter; $\lambda/4$: quarter-wave-plate.

Chapter 7

Results

The cavities built for this work have been used to detect the presence of atoms in their field as well as to collect photons from enhanced spontaneous emission into the cavity. The measurements show that the cavity is suitable for the detection of single atoms, and that it is possible to collect photons from the atoms in the cavity directly via the cavity fibre. In this Chapter, the experimental procedure for both types of measurement are described, and results from these early measurements are presented.

7.1 Reflection signal

Data has been collected to ascertain how the atoms affect the reflection signal of the cavity. The variation in the reflection signal caused by the presence of atoms was tested for a range of values for pump detuning and intensity. A variation of the number of atoms was given naturally by the passage of the Gaussian MOT cloud. These explorations of the parameter space have shown that the cavity is suitable for single-atom detection.

7.1.1 Experimental procedure

The cloud of atoms is trapped, cooled further and then dropped into the cavity mode as described in the previous chapter. This is repeated as often as deemed necessary to confidently measure the average response of the resonator. The sequence of the events which take place during a full measurement run is shown in Figure 7.1 (a). The Figure shows the raw photodiode counts for the first 32 seconds of a measurement run, and the main steps of the procedure are indicated along the trace. The passage of atoms is clearly visible even before averaging the atomic

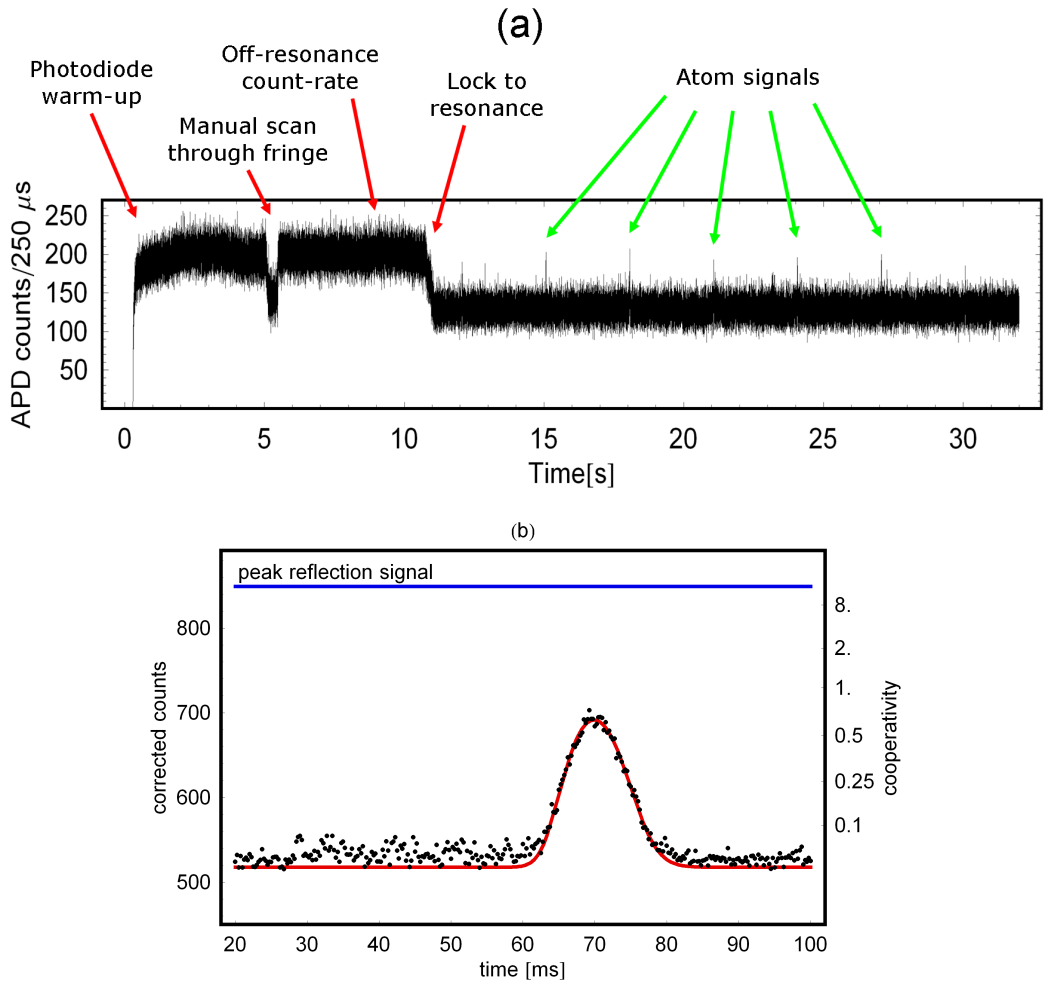

Figure 7.1: (a) A typical signal trace from one of our experiments. The graph shows the number of counts recorded on the avalanche photodiode, and along it the sequence of events which take place during one experimental run is indicated. The photodiode is left to warm up for 3 s. After that, the cavity is tuned manually, by varying the piezo voltage, to find a resonance. Once a resonance is found, the cavity is tuned slowly towards it to allow the locking mechanism to react. This brings the cavity reflection signal towards its minimum. A MOT is loaded and released every 3 s. Once the cavity is locked, the passage of the atoms is evident at these intervals, even in the raw (not averaged) data shown here. (b) average signal of all traces recorded during a measurement run. At t =27 milliseconds, after 10ms of molasses cooling, the MOT is released when the trap laser is switched off by shutter 1 (see Figure 6.5). The vibrations caused by the shutter are clearly visible in the cavity reflection signal at this time.

signals. The average of 34 measurements (taken from a different run) is shown in Figure 7.1 (b). At $t = 20\,\text{ms}$ the magnetic field is switched off, and at $t = 23\,\text{ms}$ the detuning is shifted to $-40\,\text{MHz}$ for the molasses stage. The atoms are finally released by blocking the MOT beam with shutter 1 (see Fig. 6.5) at $t = 27\,\text{ms}$. In this trace, the counts are corrected for a dark time of 44 ns. The shutter takes approximately 3ms to close, and the maximum atom density in the cavity is reached at $t \sim 69\,\text{ms}$. This corresponds to a fall-time of $t_{fall} = 39\,\text{ms}$, in agreement with a height of 7.3 mm. The values for these switching times were found by iterative maximisation of the atomic signal.

7.1.2 Weak pumping on resonance

When the atoms fall through the cavity, the reflection signal increases as expected. The trace in Figure 7.1 (b) shows an average of 34 measurements for an integration time of 250 μs. The increase in reflected light allows us to measure the cooperativity of the system from the fractional decrease in visibility from

$$J_R(\delta_\kappa) = J_{in}\left(-1 + \frac{v^-}{P}\right)^2 . \tag{7.1}$$

Here we use $v^- = 1 - \sqrt{J_R^{min}/J_R^{max}}$, as given earlier in Chapter 5, since our cavity is under-coupled. From this equation we expect the contrast of the reflected light to decrease for increasing cooperativity. This is indeed the case, and a reasonable agreement with the data is found by fitting the expected response of the cavity to the passage of a Gaussian cloud with a temperature of approximately 40 μK. This is shown as a red line in Figure 7.1 (b). No assumption is made about the atom number for this fit, but it is assumed that the average cooperativity is linearly dependent on atom number. The peak of the trace corresponds to an average cooperativity of $C_{tot} = 0.60 \pm 0.05$. The floor of the trace is calculated from the lowest points in the reflection signal, giving a visibility of 42 %, in agreement with the measurements from the previous Chapter. However it is also visible that the cavity is rarely tuned exactly to the resonance with the pump light, indicated by the red line in the absence of atoms, because of audio-frequency noise. This is caused in part by the MOT-beam shutter, and by other as of yet unknown sources. These vibrations modulate the cavity length, and are not compensated for by the locking mechanism, which is not active during the passage of the atoms. Therefore the atoms interact in general with a slightly off-resonant system. This effect is straightforwardly included using the relations from Chapter 5, and leads to a modification of the expression

for the fraction of reflected light given by

$$J_R(\delta_\kappa) = J_{in}\left|-1+\frac{v^-}{P}\frac{1}{1-\mathrm{i}\delta_\kappa/P}\right|^2, \tag{7.2}$$

where $\delta_\kappa = \Delta_{CL}/\kappa$. The measurements indicate that on average, the visibility just before and just after the passage of the atoms is 96.8 % of the maximum visibility in this measurement sequence, so that $\delta_\kappa = 0.18$, corresponding to an excursion of only 125 pm from the resonant length. Including this shift leads to a better fit to the data, shown in Figure 7.2 (a) as a green line. The cooperativity deduced from this fit, $C_{tot} = 0.597 \pm 0.046$, is very close to that calculated neglecting the shift. Conversely, this similarity indicates that at this cooperativity, the reflected intensity at the peak of the atom signal will vary weakly with shifts of the cavity length of this magnitude. In other words, light intensity fluctuations caused by length jitter are compressed. This amounts to a suppression of intensity noise of this origin, as detailed in Appendix B. From this cooperativity we can now estimate a number of atoms effectively coupled to the cavity, as shown in Figure 7.2 (b).[1]

7.1.3 Weak pumping with off-resonant light

Using the expressions from Chapter 5, the response of the cavity to weak pump light can be found. Here the laser is detuned from the atomic resonance by a fraction $\delta_\gamma = \delta_{AL}/\gamma$ of the atomic linewidth. In addition, the cavity is also shifted from its resonance, on average by a fraction of the half-width $\overline{\delta_\kappa}$, as before. This situation is illustrated in Figure 7.3 (a) and (b), where an exaggerated example of the effect of the detuning from both the atom and the cavity is given. The expected dependence of the reflected power is calculated from equations 5.18 and 5.19 in the weak-pumping limit, giving

$$J_R(\delta_\gamma, \delta_\kappa) = J_{in}\left|-1+\frac{v^-}{P}\frac{(1+\mathrm{i}\delta_\gamma)}{1+\delta_\gamma\overline{\delta_\kappa}/P+\mathrm{i}(\delta_\gamma+\overline{\delta_\kappa})/P}\right|^2. \tag{7.3}$$

[1] This is only an estimate, and is always an over-estimate, because asymmetries around the mean intensity value are neglected. The only rigorous method to extract the true value is to analyse the distribution of counts at the peak of the cloud signal, and iteratively extract the underlying set of Poissonian count distributions using an expectation-maximisation algorithm.[43] This underlying set then gives a direct mapping to the distribution of cooperativity values present, which would allow the extraction of both the number of atoms and the peak single-atom cooperativity of the system. For the data available here it is however more difficult to extract a precise value, because of the small sample size and because of the presence of non-negligible technical noise, which modifies the distribution in a manner that has not yet been fully quantified.

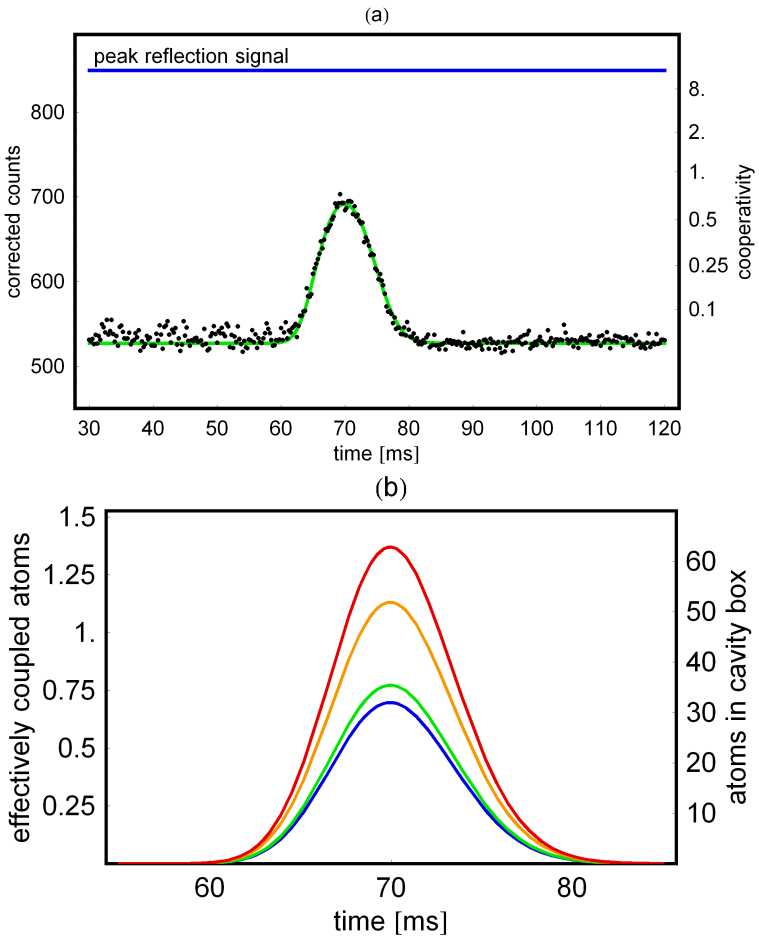

Figure 7.2: (a) A better fit for the drop data is found when the offset of the cavity length from the resonance with the pump laser is included (see text). (b) The cooperativity corresponding to the peak intensity level can be used to estimate a number of atoms in the cavity using the considerations from Appendix B. The lines shown are for : maximum finesse and transition dipole moment (blue); central finesse value and maximum transition dipole moment (green); central finesse value and minimum transition dipole moment (orange), and minimum finesse and dipole moment (red line).

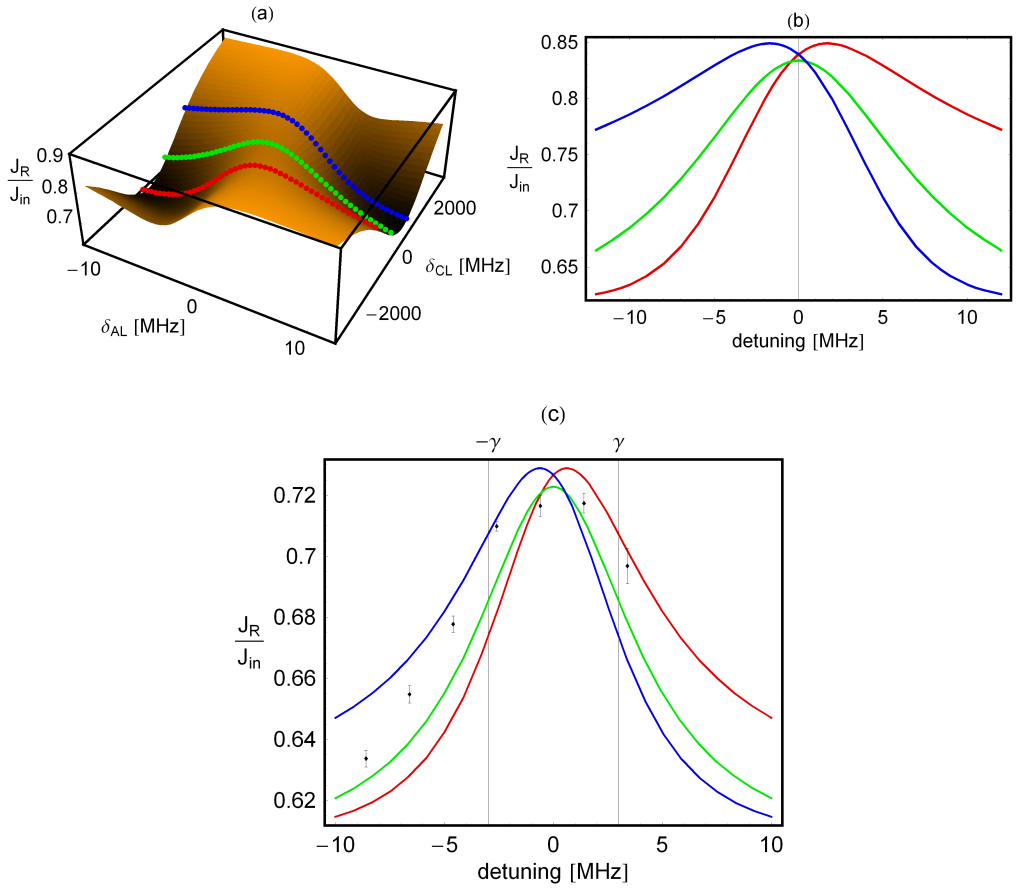

Figure 7.3: Effect of the detuning of the pump light from the atomic and cavity resonances. (a) This plot shows the spectrum along both detunings. The lines traced by the red, blue and green dots are repeated in (b) in the same colours, and are calculated for a large $\overline{\delta_\kappa}$ =-0.3, +0.3 and 0, respectively. (c) shows the experimental data, together with calculated lines for the measured $\overline{\delta_\kappa} = \pm 0.18$ (blue and red), and the resonant spectrum (green) for a cooperativity of C =0.25.

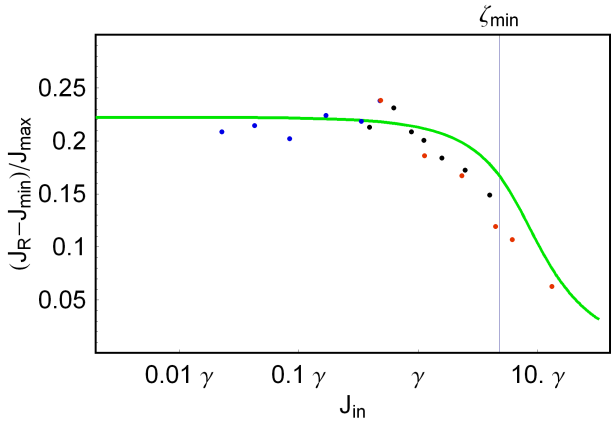

Figure 7.4: reflection signal versus intensity. The green line shows the closest agreement with the data allowed by the measured cavity parameters (see text). The blue points are the result of measurements without a neutral-density filter, while the black and red points were measured using filters with reduction factors 1:4 and 1:25, respectively. The value above which bi-stablilty can occur, ζ_{min}, is shown as a blue line.

The cavity offset for these measurements was found as previously, and for these traces a value of $\overline{\delta_\kappa} = 0.18$ was measured. The laser detuning was varied between $-8.6\,\mathrm{MHz}$ and $+3.4\,\mathrm{MHz}$, limited by the scan range of the reference laser. The points in Figure 7.3 (c) are calculated by averaging the ten points closest to the peak in the average trace for each detuning value. The figure shows that the data is encompassed by curves calculated for the measured $\pm\overline{\delta_\kappa}$, shown in blue and red, respectively. The green line shows the expected curve for a stably resonant cavity. All three curves are plotted for a cooperativity of $C = 0.25$, and the central value for the cavity half-width $\kappa = 2\pi \times 2\,\mathrm{GHz}$ is assumed. This experiment is a direct confirmation of the Purcell effect. The measurements show a broadening of the linewidth of the combined atom-cavity system, compared to the bare atomic spectrum, consistent with the inferred cooperativity which gives $2\gamma_{tot} = 1.5 \times 2\gamma$.

7.1.4 Strong pumping on resonance

The last parameter to be varied in this set of reflection measurements was the pump power, ζ. Once again simplifying the expressions from Chapter 5, the reflected intensity on resonance will depend on the pump rate with

$$J_R(\zeta) = J_{in}\left|-1 + v^{-}\frac{\kappa}{\zeta}\alpha_{res}(1)\right|^2, \tag{7.4}$$

where $\alpha_{res}(1)$ is the first cubic solution to the full-resonance equation given in Chapter 5, and for our cavities, $\zeta = \sqrt{J_{in}T_1\eta_{h,v}^2/\tau_{rt}}$. At the higher intensities used to achieve saturation of the atom-cavity system, the APD had to be shielded with neutral-density filters. From Section 5.4, we expect the effect of the atoms on the cavity signal to decrease for increasing intensities because of the saturation of the atoms. This is clearly visible in Fig. 7.4, where the data taken without ND-filter is shown as blue dots, while points measured with ND-filters of reductions 1 : 4 and 1 : 25 are shown in black and red, respectively. Since the round-trip time of the cavity is well-known, and this is in essence a measurement of the quantity $t_1^{eff} = \sqrt{T_1\eta_{h,v}^2}$. The closest agreement is found with the limiting value, 63×10^{-3}. This limit is given by the maximum mode overlap and minimum reflectivity, indicating that the true values of these quantities lie towards that end of their previously measured range. The agreement cannot be expected to be perfect, as the small cavity-length offset has not been taken into account. At high intensities, radial heating of the atoms leading to decreased interaction times may also have occured. This may explain the observation of lower-than-expected signals close to saturation. Furthermore, with the quantities of atoms involved, bi-stability may have occurred for pump values greater than ζ_{min}, indicated by a vertical line in Fig. 7.4, for the high-cooperativity tail of the distribution of cooperativity sums. This would lead to a departure from the expected average signal. This effect, if present, is hidden by the single value of the cooperativity assumed, but is expected to be small given the average cooperativity inferred from the measurements. To determine whether it is present will require a complete analysis of the distribution of the reflected intensity at each pump value. The possibility of losses in the optical path additional to those of the beamsplitter and the quantum efficiency of the APD will also need to be eliminated to extract precise quantities from this measurement.

Nonetheless, once the experiment will have matured with improved stability and more precise characterisation of its properties, this measurement offers the intriguing opportunity to almost reverse the aim of the project, namely to measure the characteristics of the cavity using atoms.

7.2 Enhanced spontaneous emission

The last set of results obtained is perhaps the most explicit demonstration of the atom-cavity interaction, namely the modification of the emission rate of the atoms by the cavity mode.

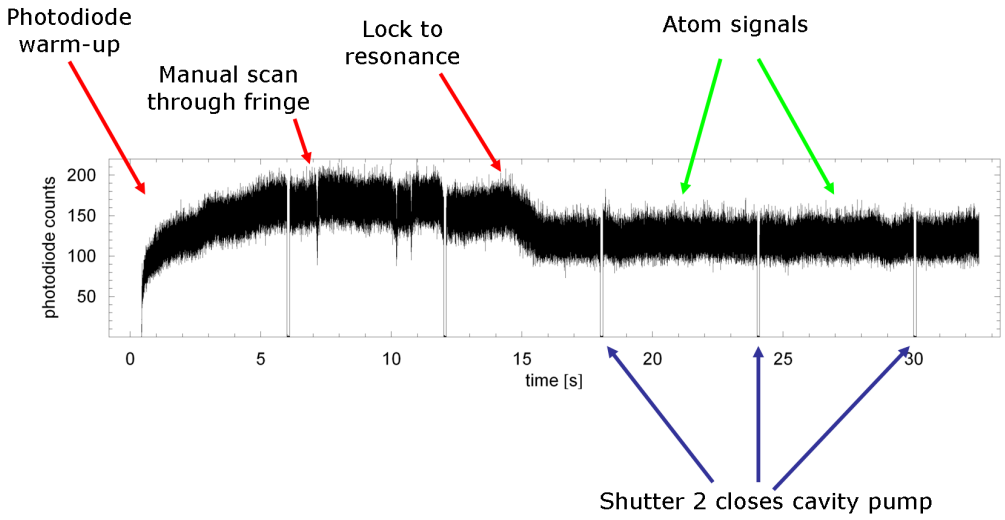

Figure 7.5: Reflected-power counts during a fluorescence measurement run. As in the previous sections, the APD is left to warm up for a few seconds before a fringe is found. A MOT is released every three seconds. Alternatingly, the passage of the MOT is observed by measuring the reflected cavity-pump light or by collecting flourescence photons. To do the latter, the cavity pump light is switched off as indicated by the blue arrows. In both cases, the atoms in the cavity are driven from the side with a resonant beam and a re-pump beam. This allows us to observe the dynamics of the cloud as well as the light emitted into the cavity (see following Figure).

7.2.1 Experimental procedure

The cloud of atoms is trapped, cooled further and then released into the cavity mode as in the previous Section. However, once the atoms reach the resonator, a beam transverse to the cavity axis is applied which excites the atoms. The sequence of the events which take place during a full measurement run is shown in Figure 7.5. A MOT is released every three seconds as before, but now we alternatingly observe the fluoresced photons and the reflected power. Driving the atoms from the side of the cavity leads to an abrupt decrease of the cavity reflection signal, as visible in Figure 7.6 (a). This is due to the heating of the atom cloud during the scattering of pump photons. In the process, the atoms emit photons in all directions. The small mode volume and high finesse of the resonator however lead to the cavity mode being the strongest decay channel for atoms in the intense regions of its mode. The

reflected power just before the arrival of the excitation beam allows an estimate of the cooperativity, which for this run of measurements was $C = 0.25$. This indicates that the atoms are expected to radiate photons into the cavity mode at a rate of 0.5 γ. The excitation light is released through a shutter with an opening time of 0.5 ms for an opening distance of 6 mm. The $1/e^2$-diameter of the excitation beam is 1.48 mm. The power was 150 μW of resonant light and 70 μW of the re-pump light. The intensity of the resonant light was therefore 123 W/cm^2 on average. This is far greater than the saturation intensity of Rubidium even for isotropically polarised light, indicating that the atoms would saturate almost immediately after the shutter was opened. We observe a significant burst in collected photons at precisely the time the atoms are driven with the side beam. This is shown in Figure 7.6 (b), where the photon count rate was measured in bins of 100 μs. On average, almost 1 photon is collected for each drop, and the signal is clearly distigusihable from the background level before the event. After the fluorescence spike, the number of collected photons is slighlty increased, probably because of scattered excitation light, but still far below the level of the collected fluorescence photons. Efforts are currently underway to quantify the collection efficiency and the enhancement factor given by the cavity.

These early results already demonstrate that the devices are indeed suitable for the detection of atoms and the collection of photons from enhanced emission. With small improvements in the stability and some effort towards a more precise characterisation of the setup, it will be possible to determine the quantities measured herein with higher accuracy. In the near future, this experiment will however be replaced by an improved cavity setup which will open up possibilities for more exotic measurements, as described in the next and final chapter.

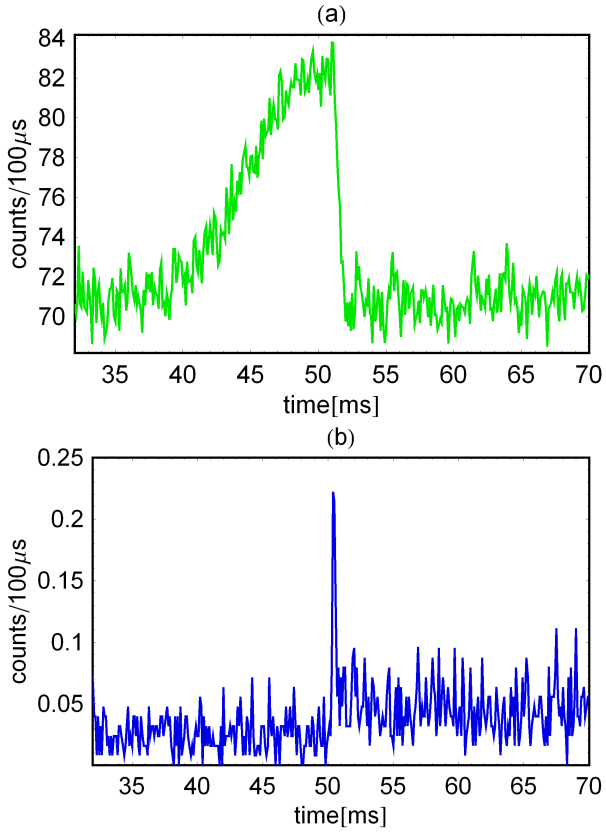

Figure 7.6: Fluorescence collection. (a) When a cloud of atoms passing through the cavity is observed via the reflected pump light, it can be seen that the reflected intensity drops back to the minimum when the shutter is opened, indicating that the atoms are rapidly heated out of the cavity mode. (b) When the cavity pump light is off, the only photons detected are dark counts and from atoms fluorescing in the cavity. The latter appear as an evident burst when the shutter is opened.

Chapter 8

Summary and outlook

8.1 Summary

The microcavities developed for this work have been characterised optically, and their properties are now well-understood. They have furthermore been used successfully to detect small clouds of atoms, with a number of atoms effectively coupled to the cavity of less than 1. Even though the device was not operating at its optimum, it was possible to characterise the response of the atom-cavity system for detuning and pump power, and even to detect vacuum-stimulated photons collected via the cavity fibre. These results indicate that the cavities are ideally suited as atom detectors for atom chips and that future versions of the devices will have sufficiently high quality to produce single photons on demand for applications such as quantum cryptography and quantum information processes. The scalability and integrability of these cavities with existing atom-chip technology is of great importance for these applications. Here the scalabity is given by the fact that the cavity mirrors can be fabricated in large arrays, using process steps that are straightforward to include in the fabrication procedure of an atom chip. The direct fibre-coupling of the cavities is also of importance for these application, as many quantum-information protocols rely on high-efficiency readout of the quantum state of the atom-cavity system. As shown in Chapter 2, the coupling efficiency can be made near-perfect by tuning the cavity length to match the cavity and fibre mode waists. This feature makes the cavities ideal candidates for nodes in a quantum network. Currently the performance of the cavities is limited by the roughness of the etched silicon surface. However, in collaboration with the team in Southampton, we have developed a procedure to improve the surface quality significantly, as shown in the following Section. The rest of this Chapter is an outlook on the promising future of these devices.

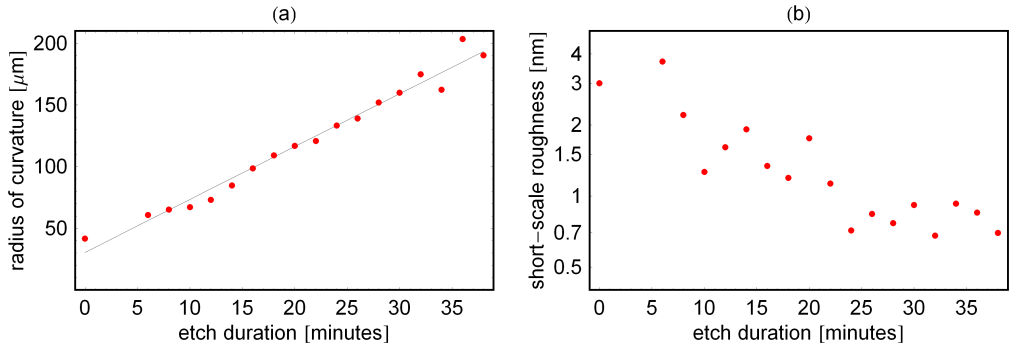

Figure 8.1: (a) Radius of curvature versus etch duration for isotropically ICP-etched silicon. (b) Short-scale roughness as a function of etch duration, measured on line segments of 1.2 microns length.

8.2 Towards strong coupling

Recently we discovered that by a process known as "inductively-coupled plasma etching" (ICP) it is possible to reach sub-nanometer roughness values in our silicon mirror-substrates.[36] This is an improvement by an order of magnitude on our current devices. Our collaborators in Southampton have already used this procedure to fabricate surfaces with a roughness of 0.9 ± 0.1 nm, but it appears possible that this fabrication method may allow us to reach 0.2 nm in future. The latest etch profiles have been analysed with an optical profilometer to measure their shape and roughness as shown in Figure 8.1. It was seen that the roughness decreases with etching time reaching sub-nanometer values after approximately 24 minutes of exposure to the plasma etcher. For longer exposures, the roughness does not show a strong dependence on etching time, but it is thought that these values are close to the resolution limit of the instrument. From the Debye-Waller loss factor (Chapter 3) we can calculate that the current value already allows us, in principle, to reach a reflectivity of 99.97 % on the silicon mirrors, giving a finesse of $F > 12000$ for a cavity in which both mirrors have this reflectivity. This means that with cavities of our dimensions we can enter the strong-coupling regime with $g/\kappa > 1$, as shown in Figure 8.2. By further reducing the roughness, even higher performance can of course be achieved. Some examples are shown in Figure 8.3.

Furthermore, this procedure makes it possible to create mirrors with smaller radii of curvature than our current mirrors, while achieving both lower roughness and a more accurately spherical profile. This will allow us to achieve better mode-matching values while keeping the cavity length further within the stability range of the resonator than with our present mirrors. As stated earlier, good mode-matching

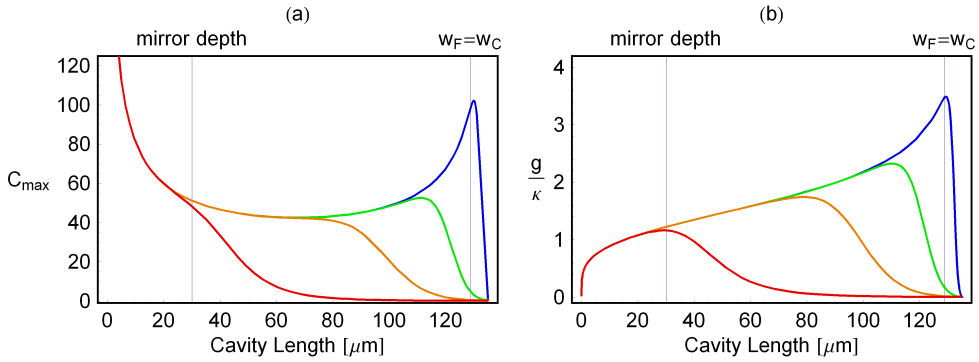

Figure 8.2: (a) Maximum single-atom cooperativity for the best fabricated silicon mirror substrates, with a radius of curvature of 135 μm. The plots assume that the reflectivity is limited by an RMS roughness of 1 nm, and that it decreases due to an aperture of diameter 20 (red), 30 (orange), 40 (green) or 60 μm (blue). The mirror diameter for this etch was $> 100\,\mu$m, but the roughness has currently only been measured for a diameter of $\sim 20\,\mu$m. The finesse is calculated using the (unfavourable) transmission limit. (b) Coupling measure g/κ for the same parameters.

is important for the collection of cavity-stimulated photons. Another important factor in this application is the transmission of the fibre mirror. With improved reflectivity on the silicon mirror it will be possible, by increasing the transmission of the input mirror, to create cavities where this transmission becomes the dominant decay channel for photons, while maintaining large Purcell factors. This brings us into another interesting regime, namely that of over-coupled resonators. In this regime, the effect of a small cooperativity on the reflected power is greater than for under- or critically-coupled resonators at the same cooperativity, if we confine ourselves to the weak-pumping regime. The effect is even larger than if we looked at the transmitted signal as is commonly done. This is shown in Figure 8.4 (a). Furthermore, it is not monotonic as in the other cases. The two regimes before and after the minimum are entirely distinguishable because the phase of the reflected light flips at the transition. This is interesting because with the right parameters, it means that larger numbers of atoms can be counted than with the other types of resonator.[33] This is made evident by Figure 8.4 (b). There the derivative of the normalised detected power is plotted, showing that the change in the reflected signal is larger for the under-coupled resonator everywhere except close to where the reflected power reaches a minimum.

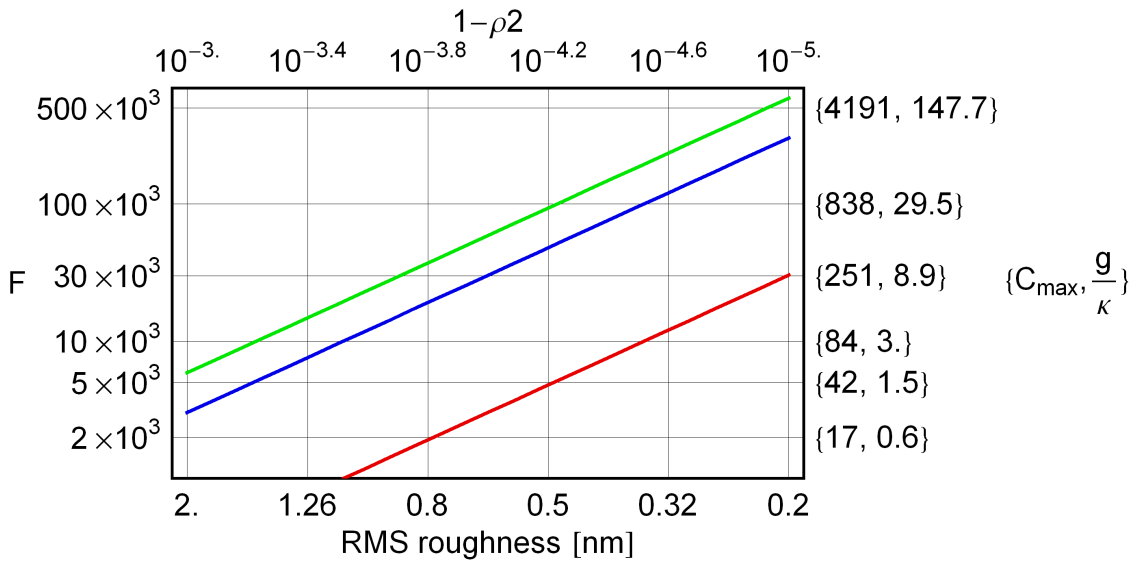

Figure 8.3: Maximum possible finesse (left scale), cooperativity and coupling value (right scale) for a given concave-mirror roughness. The radius of curvature is 135 μm as above. No aperture effect is considered. The resonator length is fixed at 128.8 μm, where the fibre-cavity coupling is perfect. The blue line shows the values for a critically-coupled resonator. The red line is for an over-coupled cavity for which the collection efficiency for photons generated in the cavity is fixed at 95 %. For the green line, the cavity is under-coupled to a visibility of $\vartheta = 0.1$ to achieve higher finesse.
The reflectivities required (top scale) are within reach of currently available coating techniques.

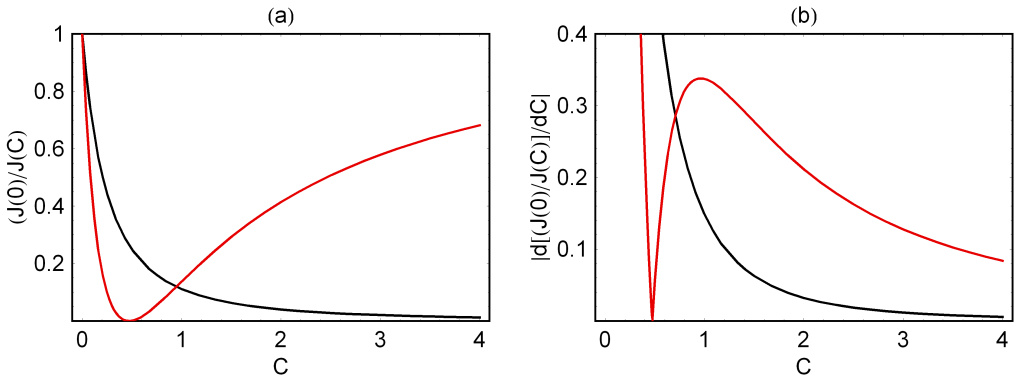

Figure 8.4: (a) Red line: detected power for an over-coupled resonator with a visibility of $\vartheta = 0.9$, normalised to the reflected power of the empty cavity. Black line: normalised detected power when measuring in transmission. (b) derivative of the normalised detected power for the same parameters.

8.3 Design evolution

The next experiment, which is in the final design stages, will consist of at least four, independently tunable cavities, two of which will be critically-coupled and two of which will be under-coupled as described above. Depending on the timing of events in the coming months, some more time may be devoted to including a pair of under-coupled cavities in which some fraction of the visibility is sacrificed to achieve a larger ratio of g/κ. The design is modular so that in principle, the number of cavities is limited only by the chip size. In this incarnation, the fibres will be moved by piezos unlike at present where the chip position is adjusted. One of the current ICP-treated chips will be coated and used in this experiment. This will allow us to perform the same experiments as described in this thesis, but with better-performing cavities. In parallel, efforts will be made to further improve the etching technique. Over the last months, much work has been done to create a better laser system, which will without doubt improve the measurements. Furthermore, the new cavity setup will include better vibration isolation and improved active stabilisation. Optical dipole-force guides will be included in the system once these preliminary improvements have been made. The design also allows for the inclusion of an external magnetic guide, which will eventually be replaced by a wire microfabricated on the mirror-chip.

8.4 Integration

At present, the first chips to include both wires and cavities are being manufactured in Southampton. These can be fitted into the new design, and will be included as soon as available. Other integration opportunities are provided by the micropyramids which are being developed at CCM [44]. Using these, each cavity could be supplied with atoms by its own pyramid MOT.
A further microcavity design which is being developed in collaboration with Southampton is a fully planar device which is tuned by an integrated electrostatic actuator. This can be used to form cavities with concave-tip fibres [31]. An even more scalable setup could be constructed out of these actuated mirrors and a set of microfabricated optical waveguides, provided that either the waveguide tips or the actuated mirrors can be made concave by etching or ablation. A waveguide chip has already been developed at CCM for other projects, and the experience from that project will certainly be of use in this endeavour. Microfabricated waveguides could also be used with the current concave mirrors. This imposes stringent requirements on the accuracy of the fabrication, because of the detrimental effects of lateral misalignment on the fibre-cavity coupling, and thereby on both the contrast and the photon collection efficiency of the devices. It should be possible to test this with the current waveguide chip, as the separation of the waveguides at the edge of the chip was chosen to be 250 μm, half the present micromirror pitch, for this purpose. Should this work, the challenge will be to fabricate a setup in which each cavity mirror can be tuned independently.

In conclusion, the devices first developed and tested in this thesis stand at the very beginning of a highly promising career. Their scalability, the open access to the entire cavity field and their projected performance all indicate that these microcavities have a bright future, in atomic physics and in endeavours towards quantum computation.

Bibliography

[1] P. A. M. Dirac, "The Quantum Theory of the Emission and Absorption of Radiation" , *Proc. Roy. Soc. A*, **114**, 767 (1927).

[2] V. Weisskopf and E. Wigner, *Z. Phys. A (Hadrons and Nuclei)*, Springer Berlin/Heidelberg **63**, 1-2 (1930).

[3] M. Fox, "Quantum Optics: an Introduction" , Oxford University Press (2006).

[4] E.T. Jaynes, F.W. Cummings, "Comparison of quantum and semiclassical radiation theories with application to the beam maser," *Proc. IEEE* **51**, 1 (1963).

[5] K. J. Vahala, Nature **424**, 839 (2003).

[6] Wallraff, A.; Schuster, D. I.; Blais, A.; Frunzio, L.; Huang, R.-S.; Majer, J.; Kumar, S.; Girvin, S. M.; Schoelkopf, R. J.,"Strong coupling of a single photon to a superconducting qubit using circuit quantum electrodynamics", *Nature* **431**, 7005 (2004).

[7] S. Kuhr, S. Gleyzes, C. Guerlin, J. Bernu, U. B. Hoff, S. Deleglise, S. Osnaghi, M. Brune, J.-M. Raimond, S. Haroche, E. Jacques, P. Bosland, and B. Visentin, "Ultrahigh finesse Fabry-Pérot superconducting resonator", *Appl. Phys. Lett.* **90**, 164101 (2007).

[8] H. J. Carmichael, R. J. Brecha, M. G. Raizen, H. J. Kimble, and P. R. Rice, "Normal-mode splitting and linewidth averaging for two-state atoms in an optical cavity", *Phys. Rev. Lett.* **63**, 240 - 243 (1989).

[9] I. Teper, Y.-J. Lin, and V. Vuletiċ, "Resonator-Aided Single-Atom Detection on a Microfabricated Chip", *Phys. Rev. Lett.* **97,** 023002 (2006).

[10] A. Haase, B. Hessmo, and J. Schmiedmayer, *Opt. Lett.* **31**, 268 (2006).

[11] T. Steinmetz, Y. Colombe, D. Hunger, T. W. Hänsch, A. Balocchi, R. J. Warburton and J. Reichel, Stable fiber-based Fabry-Pérot cavity, *Appl. Phys. Lett.* **89,** 11 (2006).

[12] J. A. Sauer, K.M. Fortier, M. S. Chang, C. D. Hamley, and M. S. Chapman, *Phys. Rev. A* **69**, 051804 (2004).

[13] G. R. Guthöhrlein, M. Keller, K. Hayasaka, W. Lange, and H. Walther, *Nature* **414**, 49 (2001).

[14] A. Kreuter, C. Becher, G. P. T. Lancaster, A. B. Mundt, C. Russo, H. Häffner, C. Roos, J. Eschner, F. Schmidt-Kaler, and R. Blatt, *Phys. Rev. Lett.* **92**, 203002 (2004).

[15] E. M. Purcell, *Phys. Rev.* **69**, 674 (1946);

[16] D. Kleppner, *Phys. Rev. Lett.* **47**, 233 (1981).

[17] H. Mabuchi, Q. A. Turchette, M. S. Chapman, and H. J. Kimble, "Real-time detection of individual atoms falling through a high-finesse optical cavity". *Opt. Lett* **21**, 17 (1996).

[18] A. Kuhn, M. Hennrich, and G. Rempe, *Phys. Rev. Lett.* **89**, 067901 (2002).

[19] Trupke, M., J. Metz, A. Beige and E. A. Hinds. "Towards quantum computing with single atoms and optical cavities on atom chips." *J. Mod. Opt.* **54**, 11 (2007).

[20] Peter Horak, Bruce G. Klappauf, Albrecht Haase, Ron Folman, Joerg Schmiedmayer, Peter Domokos, E. A. Hinds, "Possibility of single-atom detection on a chip", *Phys. Rev. A* **67**, 043806 (2003).

[21] "Observation of Bose-Einstein Condensation in a Dilute Atomic Vapor", M. H. Anderson, J. R. Ensher, M. R. Matthews, C. E. Wieman, and E. A. Cornell *Science* **269**, 5221 (1995).

[22] H.J. Metcalf, P. v. d. Straten, "Laser Cooling and Trapping", Springer-Verlag New York, Inc. (1999).

[23] R. Grimm, M.Weidemüller, and Y. B. Ovchinnikov, *Adv. At. Mol. Opt. Phys.* **42**, 95 (2000).

[24] R. Folman, P. Krüger, J. Schmiedmayer, J. Denschlag, and C. Henkel, Adv. At. Mol. Phys. 48, 263 (2002).
E A Hinds and I G Hughes, J. Phys. D: Appl. Phys. 32 (1999).

[25] C. D. J. Sinclair, E. A. Curtis, I. Llorente-Garcia, J. A. Retter, B. V. Hall, S. Eriksson, B. E. Sauer, and E. A. Hinds, *Phys. Rev. A* **72**, 031603 (2005).

[26] S. Knappe, P. D. D. Schwindt, V. Gerginov, V. Shah, H. G. Robinson, L. Hollberg, and J. Kitching, "Microfabricated Atomic Clocks and Magnetometers," presented at International Conference on Laser Spectroscopy, (2005)

[27] "Quantum information processing with neutral atoms on an atom chip", J Schmiedmayer, R Folman, T Calarco, J. of Mod. Opt., Taylor Francis (2002).

[28] M. P. A. Jones, C. J. Vale , D. Sahagun-Sanchez, B. V. Hall, and E. A. Hinds, *Phys. Rev. Lett.* **91**, 080401 (2003).
P. K. Rekdal, S. Scheel, P. L. Knight, and E. A. Hinds, *Phys. Rev. A* **70**, 013811 (2004).

[29] J. Reichel, *Appl. Phys. B* **74**, 469 (2002).

[30] T. Aoki, B. Dayan, E. Wilcut, W. P. Bowenb, A. S. Parkins, and H. J. Kimble, *Nature* **443**, 671 (2006).

[31] Y. Colombe, T. Steinmetz, G. Dubois, F. Linke, D. Hunger and J. Reichel, *arXiv*:0706.1390 (2007).

[32] B. Chron, H. Gilles, J. Hamel, O. Moreau and H. Sorel "Laser frequency stabilization using Zeeman effect", J. Phys. III France 4 401-406 (1994); Kristan L. Corwin, Zheng-Tian Lu, Carter F. Hand, Ryan J. Epstein, and Carl E. Wieman, "Frequency-Stabilized Diode Laser with the Zeeman Shift in an Atomic Vapor", Appl. Opt.**37**, 15 (1998)

[33] J. McKeever, J. R. Buck, A. D. Boozer, and H. J. Kimble, "Determination of the Number of Atoms Trapped in an Optical Cavity", *Phys. Rev. Lett.* **93**, 143601 (2004).

[34] A. Kuhn and G. Rempe, "Optical Cavity QED: Fundamentals and Application as a Single-Photon Light Source", Int. School of Physics Enrico Fermi, Course CXLVIII, (2002)

[35] C. F. Wildfeuer, PhD Thesis, University of Siegen (2003)

[36] Kristian Pontoppidan Larsen, Jan T Ravnkilde and Ole Hansen, "Investigations of the isotropic etch of an ICP source for silicon microlens mold fabrication",*J. Micromech. Microeng.* **15** (2005)

[37] J. Metz, M. Trupke, and A. Beige, "Robust Entanglement through Macroscopic Quantum Jumps", *Phys. Rev. Lett.* **97**, 040503 (2006)

[38] B. E. A. Saleh and M. C. Teich, *Fundamentals of Photonics*, John Wiley Sons, New York, (1991).

[39] A. Yariv, *Optical electronics in modern communications*, Oxford University Press, (1996).

[40] M. J. Madou, "Fundamentals of Microfabrication: The Science of Miniaturization", CRC Press (2002).

[41] Mohanied A. Abdulalim, Khalid F Hussein, and Fatma M. Elhefnuwi, "Coupling between Step-Index Optical Fiber Sections with Different Refractive Indices", *Proceedings, Twentieth national radio science conference*, Cairo, Egypt (2003).

[42] Eric W. Weisstein, "CRC concise encyclopedia of mathematics",CRC Press (1999).

[43] A.P. Dempster, N.M. Laird, and D.B. Rubin. "Maximum-likelihood from incomplete data via the em algorithm". *J. Royal Statist. Soc. Ser. B.*, **39** (1977). Jeff A. Bilmes, "A Gentle Tutorial of the EM Algorithm and its Application to Parameter Estimation for Gaussian Mixture and Hidden Markov Models", Technical Report, University of Berkeley, ICSI-TR-97-021, (1997).

[44] M. Trupke, F. Ramirez-Martinez, E. A. Curtis, J. P. Ashmore, S. Eriksson, E. A. Hinds, Z. Moktadir, C. Gollasch, M. Kraft, G. Vijaya Prakash, and J. J. Baumberg, "Pyramidal micromirrors for microsystems and atom chips", *Appl. Phys. Lett.* **88**, 071116 (2006).

Appendix A

Fibre-cavity coupling

In this appendix, the results presented in Chapter 3 will be discussed in more detail. One novel feature of these microcavities is that they are directly coupled to a single-mode fibre. What makes this arrangement interesting is that the single propagating fibre mode couples to a reservoir of a well-defined set of stable cavity modes. The coupled power will depend on the overlap integral of the fibre and cavity modes,

$$\eta_{N,h,v} = \int_{-\infty}^{\infty}\int_{-\infty}^{\infty} \psi_F^* \psi_C^{N,h,v}\, dx\, dy\,. \tag{A.1}$$

As an example, the overlap integral of two lowest-order, circular Gaussian beams with waists w_F and w_C is

$$\eta_{0,0} = \frac{2w_C w_F}{w_C^2 + w_F^2}\ , \tag{A.2}$$

and the coupled power is proportional to $\eta_{0,0}^2$. The coupled power and resulting intensity for this case are shown in the Figure below. The fibre is however not fully described by the single mode propagating in the core, there are also propagation modes in the cladding, and decaying "air" modes which couple out into the surrounding medium. These modes require intense numerical methods for their calculation, which are beyond the scope of this thesis. It is nonetheless clear that for light to exit the cavity via these modes, there must be an overlap between the cavity mode and the latter. The treatment here is confined to the limiting cases, where the fraction of light in the cavity mode which does not match the core mode will either couple fully or not at all to these modes. It will therefore be fully transmitted and lost to cladding and air modes (transmission limit), or reflected back into the cavity (reflection limit). The table below shows the entering, circulating and reflected fields for a single cavity mode. We are particularly interested in the fundamental cavity mode, and in being able to compare the measurable quantities,

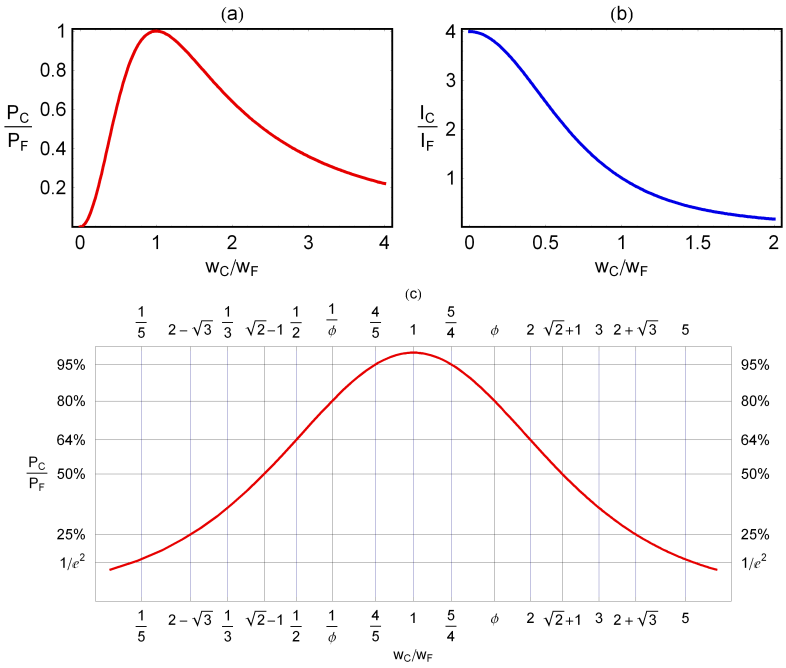

Figure A.1: Coupled power (a) and resulting peak intensity (b) for the overlap of a Gaussian input beam of waist size w_F and a receiving mode of waist size w_C. The power is plotted again in (c) with the x-axis in a logarithmic scale. The indicated crossing values for 25, 50, 64 and 80% are exact. Here, ϕ is the golden ratio.

i.e. contrast and finesse, in the two limits. Simple expressions for the behaviour of a single mode can be found if all other modes are considered to be far from resonance. It is realistic to assume that the cavity modes can, in a suitable superposition, fully describe the fibre mode. In this case, the cavity can be treated as having only two modes $\psi_{h,v}$ and ψ_b, such that $\eta_{h,v}^2 + \eta_b^2 = 1$, and ψ_b is perfectly and perennially out of phase. This simplification leads to the expressions in the second part of the table. By furthermore assuming that the reflectivity of both mirrors is high, the cavity can be treated as completely rejecting light in the out-of-phase modes at the input in both reflection and transmission limits. This final approximation leads to the expressions which are used in Chapter 3, given at the end of the table. Again, both mirrors are lossless and have real reflectance coefficients $r_1 = \sqrt{\rho_1}$ and $r_2 = \sqrt{\rho_2}$. In the following table, the total electric field A and power P are listed for a standard cavity and for a fibre cavity in the reflection and transmission limits. The last line gives the peak circulating intensity for circular Gaussian fibre and cavity modes.

To properly calculate the overlap integral of each mode, the precise knowledge

of the cavity length and mirror radius of curvature is necessary, which were found by measuring the distance between the radial and lowest-order fringes. To extract this value, the time-voltage traces were converted by taking into account the mean acceleration measured from the fringe widths. To limit the number of approximations made, all quantities were calculated as fractions of the lowest-order fringe separation at each length, $\Delta_L^{rel} = L_{q+1,0,0} - L_{q,0,0}$. For astigmatic resonators, the round-trip phase shift needs to be calculated separately for each axis. This results in the resonance condition

$$L_{q,h,v} = \frac{\lambda}{2}\left[q + \left(h+\frac{1}{2}\right)\frac{\arccos\left(\sqrt{G_2^a(L_{q,h,v})}\right)}{\pi} + \left(v+\frac{1}{2}\right)\frac{\arccos\left(\sqrt{G_2^b(L_{q,h,v})}\right)}{\pi}\right], \tag{A.3}$$

where G_2^a and G_2^b are calculated the two radii of curvature of the mirror $R(a)$ and $R(b)$. The main complication of this quantity, i.e. the length dependence of G_2^a and G_2^b, can be neglected if the measurement is not taken close to the limits of stability so that these quantities vary negligibly between adjacent modes. To calculate $R(a)$, for example, the measured quantity reduces to

$$\frac{L_{q,h,0} - L_{q,0,0}}{\Delta_L^{rel}} = \frac{h}{\pi}\arccos\left(\sqrt{G_2^a(L_{q,h,0})}\right) \tag{A.4}$$

A plot showing all detected radial fringes is shown in Figure A.2. Here, all fringes were treated as possible doublets, the minima of which are shown in blue and red. The points are on top of each other when no splitting is detected. The figure shows good qualitative agreement in all modes with the radii of curvature calculated from the $(q, 2, 0)$ and $(q, 0, 0)$ modes which cross the centre of the plot. The dashed lines are the antisymmetric modes of the cavity. These do not couple to the fibre mode when the core of the fibre is well-centred, and are therefore rare occurrences in the figure.

Quantity	standard	reflection limit	transmission limit
A_{in}	$A_0 t_1$	$A_0 t_1 \eta_{h,v}$	$A_0 t_1 \eta_{h,v}$
A_{circ}	$A_0 t_1 \sum_{n=0}^{\infty} (r_1 r_2)^n e^{i\phi}$ $= A_0 \frac{t_1}{1-r_1 r_2 e^{i\phi}}$	$A_0 \frac{t_1 \eta_{h,v}}{1-r_1^{h,v} r_2 e^{i\phi(h,v)}}$	$A_0 \frac{t_1 \eta_{h,v}}{1-r_1 r_2 e^{i\phi(h,v)}}$
A_R	$-A_0 r_1 +$ $A_0 t_1 \frac{r_2 t_1 e^{i\phi}}{1-r_1 r_2 e^{i\phi}}$ $= -r_1 A_0 +$ $A_0 \frac{T_1 r_2}{e^{-i\phi}-r_1 r_2}$	$-r_1 A_0 +$ $A_0 \frac{T_1^{h,v} r_2}{e^{-i\phi(h,v)}-r_1^{h,v} r_2}$	$-r_1 A_0 +$ $A_0 \frac{T_1^{h,v} r_2}{e^{-i\phi(h,v)}-r_1 r_2}$
A_R^{total}	A_R	$-r_1 A_0 +$ $A_0 \sum_{h,v=0}^{\infty} \frac{T_1^{h,v} r_2}{e^{-i\phi(h,v)} - r_1^{h,v} r_2}$	$-r_1 A_0 +$ $A_0 \sum_{h,v=0}^{\infty} \frac{T_1^{h,v} r_2}{e^{-i\phi(h,v)} - r_1 r_2}$
		two-mode approximations	
$A_R^{total} \approx$		$-r_1 A_0 +$ $A_0 \frac{T_1^{h,v} r_2}{e^{-i\phi(h,v)}-r_1^{h,v} r_2} +$ $A_0 \frac{T_1^b r_2}{-1-r_1^b r_2}$	$-r_1 A_0 +$ $A_0 \frac{T_1^{h,v} r_2}{e^{-i\phi(h,v)}-r_1 r_2} +$ $A_0 \frac{T_1^b r_2}{-1-r_1 r_2}$
		high reflectivity	
$A_R^{total} \approx$		$-r_1^{h,v} A_0 +$ $A_0 \frac{T_1^{h,v} r_2}{e^{-i\phi(h,v)}-r_1^{h,v} r_2}$	$-r_1^{h,v} A_0 +$ $A_0 \frac{T_1^{h,v} r_2}{e^{-i\phi(h,v)}-r_1 r_2}$
quantities of interest			
Finesse	$\frac{\pi \sqrt[4]{\rho_1 \rho_2}}{1-\sqrt{\rho_1 \rho_2}}$	$\frac{\pi \sqrt[4]{\rho_1^{h,v} \rho_2}}{1-\sqrt{\rho_1^{h,v} \rho_2}}$	$\frac{\pi \sqrt[4]{\rho_1 \rho_2}}{1-\sqrt{\rho_1 \rho_2}}$
$1-\vartheta$	$\left(\frac{\sqrt{\rho_1}-\sqrt{\rho_2}}{1-\sqrt{\rho_1 \rho_2}}\right)^2$	$\left(\frac{\sqrt{\rho_1^{h,v}}-\sqrt{\rho_2}}{1-\sqrt{\rho_1^{h,v} \rho_2}}\right)^2$	$\left(-r_1^{h,v} + T_1^{h,v} \frac{\sqrt{\rho_2}}{1-\sqrt{\rho_1 \rho_2}}\right)^2$
$P_{circ}^{resonant}$	$\frac{P_0 T_1}{(1-\sqrt{\rho_1 \rho_2})^2}$	$\frac{P_0 T_1^{h,v}}{(1-\sqrt{\rho_1^{h,v} \rho_2})^2}$	$\frac{P_0 T_1^{h,v}}{(1-\sqrt{\rho_1 \rho_2})^2}$
$I_{circ}^{resonant}$	$\frac{I_0 T_1}{(1-\sqrt{\rho_1 \rho_2})^2}$	$\frac{w_C^2}{w_F^2} \frac{I_0 T_1^{h,v}}{(1-\sqrt{\rho_1^{h,v} \rho_2})^2}$	$\frac{w_C^2}{w_F^2} \frac{I_0 T_1^{h,v}}{(1-\sqrt{\rho_1 \rho_2})^2}$

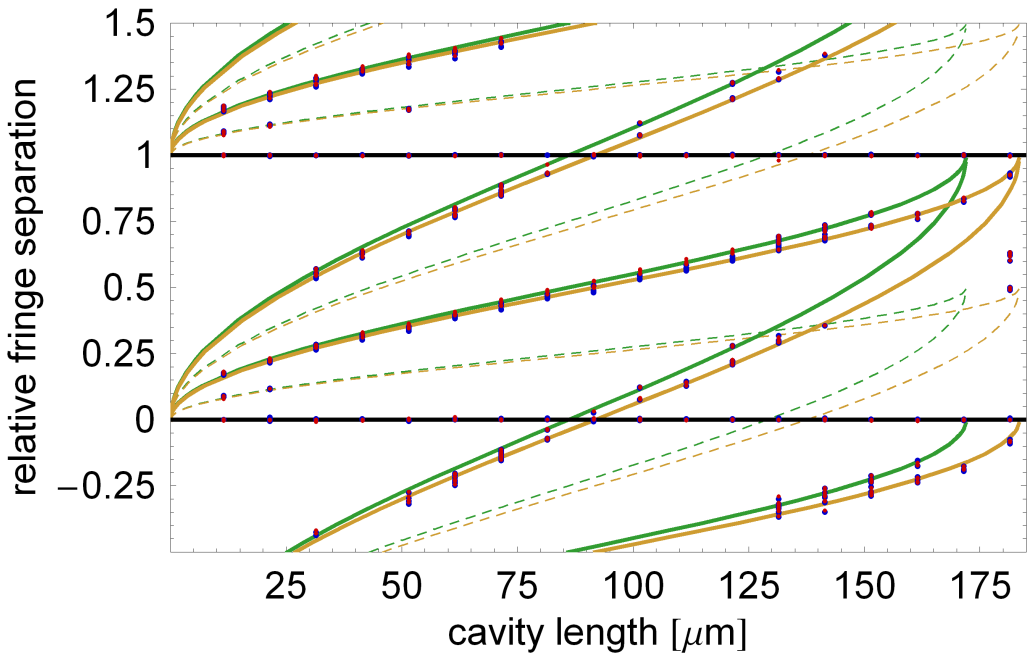

Figure A.2: Plot of relative fringe position versus cavity length for all detected fringes, together with the expected fringe separation for the three lowest-order odd (dashed lines) and even modes (solid lines) for the radii calculated in Chapter 3. The cavity astigmatism leads to a splitting of the curves, shown in gold for the smaller and green for the larger radius of curvature.

Appendix B

Damping of technical noise

As seen in Chapter 7, the cavity was not fully stabilised during the measurements performed for this work. This results in an effective offset from the cavity resonance, but the cavity length fluctuates because of acoustic noise causing noise in the reflected intensity. It was noticed that the presence of the atoms coincides with a decrease of this noise. A simple explanation to at least a part of this smoothing is given by the additional damping of the cavity by the atoms. While no aimed study has been performed to quantify this effect, it was noticed during the course of many experimental runs. This subsection is intended to provide a simple, qualitative description of this mechanism. To give a picture of the effect of the atoms on the intensity fluctuations, the simplifying assumption is made that the cavity moves at random about the mean position given by $\overline{\delta_\kappa}$ in such a way that it leads to intensity fluctuations with Gaussian statistics. Then the amplitude of its excursion can be calculated from the standard deviation of the light intensity when the cavity is empty, with

$$\frac{\sigma^2_{light}}{\overline{N_{true}}} = \frac{\left(\sqrt{\overline{N_{true}}} + s_{light}\overline{N_{true}}\right)^2}{\overline{N_{true}}} . \tag{B.1}$$

In other words, it is hereby assumed that the cavity fluctuates asymmetrically in length on only one side of the fringe in such a way as to create Gaussian noise.

This is a close approximation to the case of symmetric oscillations about the resonant length. It is also assumed that all super-Poissonian noise is caused by this effect. Here the true number of photons absorbed by the detector is found using the detector correction as detailed in Section 6.6, but $\overline{N_{true}}$ must also be corrected for detector efficiency and other losses, while the variance-to-mean ratio is corrected for the beamsplitter transmission η_{BS} and the quantum efficiency of the APD η_{QE}

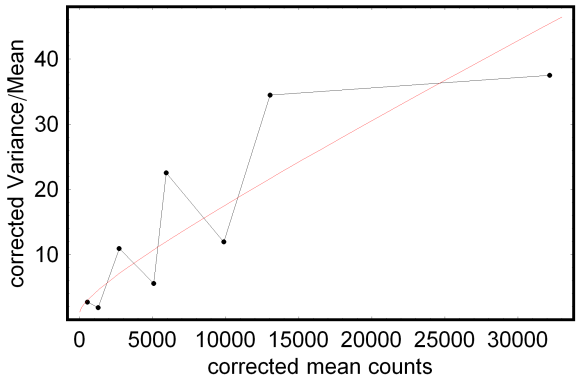

Figure B.1: The corrected variance-to-mean ratio as a function of power broadly follows the behaviour expected from Eq. B (red line).

with

$$\frac{\sigma^2_{light}}{\overline{N_{true}}} = 1 + \left(\frac{\sigma^2_{measured}}{\overline{N_{true}}} - 1 \right) / (\eta_{BS}\eta_{QE}). \tag{B.2}$$

Figure B.2 (a) shows the average signal of 22 atom clouds, and the green line shows a fit including a mean length-offset of $\overline{\delta_\kappa} = 0.3$.

Then the additional shifts of the cavity from its mean offset $\overline{\delta_\kappa}$ can therefore be calculated from the normalised variance of the empty cavity from the Lorentzian of the empty resonator. From the power spectrum of the fluctuations of the empty cavity (B.2 (c)) it can be seen that the noise is acoustic. The cavity is therefore assumed to travel on average in the range spanned by δ^+_κ and δ^-_κ, given by

$$\delta^\pm_\kappa = \sqrt{\frac{\vartheta\overline{\delta_\kappa} \pm s_{light}(1 - \vartheta + \overline{\delta_\kappa})}{\vartheta \mp s_{light}(1 - \vartheta + \overline{\delta_\kappa})}}\,. \tag{B.3}$$

The inferred flucuations of the cavity length lead to an expected range of intensity fluctuations around the mean offset as indicated by the two black lines in Figure B.2 (b). The normalised variance in the presence of atoms depends on the Purcell factor. The distribution of counts in the presence of atoms is taken to be sufficiently symmetric to be approximated by

$$\frac{\sigma^2_{light}(P)}{J_R(\overline{\delta_\kappa})\tau_{int}} = \frac{(J_R(\delta^+_\kappa) - J_R(\delta^-_\kappa))^2}{4J_R(\overline{\delta_\kappa})}\tau_{int}\,. \tag{B.4}$$

Comparing this to the variance of the empty cavity shows the decrease in noise, as visible in B.2 (d). The semi-classical mechanism described here cannot account for sub-Poissonian statistics, as it only reduces the fraction of super-Poissonian noise caused by cavity-length fluctuations. It is thought that a fully-quantised description, including anti-bunching of the photons scattered by cavity atoms, may provide an adequate explanation for such an event. This will require a more targeted

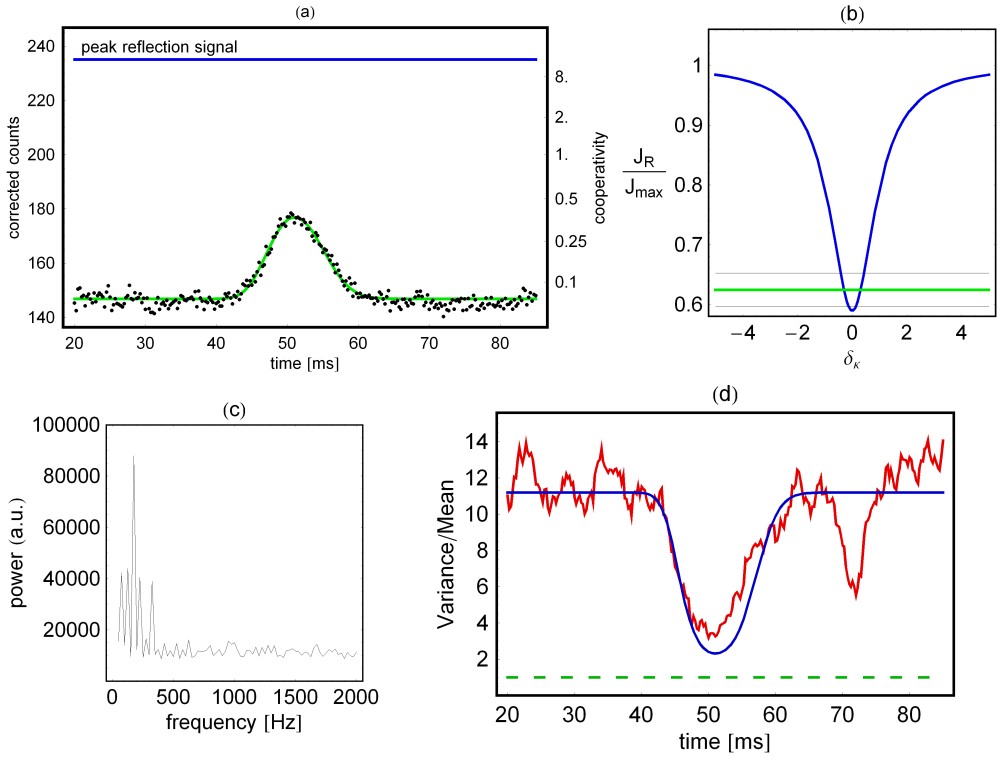

Figure B.2: (a) The averaged signal of 22 runs fluctuates around a mean value given by the green line. From the empty cavity signal the amplitude of the fluctuations can be estimated, as shown in (b). The power spectrum (c) indicates that the noise is acoustic in nature, as it is largely featureless for frequencies above 500 Hz. The passage of the atoms reduces the intensity fluctuations, as visible in the plot of the variance-to-mean ratio shown in (d). This agrees qualitatively with the mechanism outlined in this Appendix, as shown by the blue line.

study, for which it is estimated that the cavity stabilisation will need to be improved to reach sub-picometer accuracy.

Appendix C

Cooperativity distribution

This appendix looks in some detail at the cooperativity distribution of atoms falling through the cavity.

As shown in the previous chapters, the cavity signal will depend on the cavity parameters and on the coupling of the atomic cloud to the light in the resonator. This in turn will depend on the state of the atoms and the alignment of their dipoles, on the polarisation of the light and on the position of the atoms in the mode. As no magnetic fields are applied during the measurements, the atoms are assumed to be Zeeman-degenerate. While efforts were made to pump the cavity with circularly polarised light, this could not be guaranteed in general as the optical fibre is of unknown and varying birefringence. This has not been quantified by measurement, so no assumption is made regarding the light polarisation in the following discussion, other than that it remains constant over the course of a measurement. It is furthermore assumed that the coupling of any atom to the cavity mode depends only on its position therein. This is justified if either: i) The equilibrium Zeeman-sub-level population distribution is reached quickly for all atoms compared to their interaction time with the cavity mode; (ii) all atoms start in the same sub-level population distribution and this changes negligibly over the duration of the interaction with the cavity light. The first case can be excluded a priori because many atoms will enter the cavity mode in a region of low field strength and scatter few or no photons. The second case is certainly more likely, as all atoms have undergone molasses cooling. Given these assumptions, the maximum and minimum single-atom cooperativity can be evaluated from the measured cavity characteristics, wherein the finesse constitutes the largest uncertainty, and the strongest and weakest transition dipole moments. It is thereby confined to the range

$$0.45 < C_{max} < 0.88. \tag{C.1}$$

The position-dependence of the cooperativity is affected by the fact that the atoms can move by a considerable distance during one integration period τ_{int}, both compared to the cavity waist, due to their fall velocity transverse to the mode, and compared to the light wavelength due to heating caused by the scattering process.

Distribution of the cooperativity

Given the above, it is necessary to calculate the distribution of atoms coupling with a given strength to the cavity light mode to correctly interpret the reflection signal of the cavity. The atoms are assumed to fall into all regions of the cavity with equal probability, so that the coupling distribution is equal to the field distribution in space. While the electric field in a given volume is readily evaluated, the inverse of this quantity, i.e. the volume per electric field strength, is not as straightforward to calculate without making harsh approximations such as replacing the radially Gaussian profile of each mode lobe by a cos^2 or vice-versa. The distribution can however be found easily by numerical means. To this end, a million points were sampled at random in a fictitious cavity field within a rectangular "cavity box" spanning the cavity length in the z-direction, and with a width of $6w_C$ in the $x-$ and $y-$directions, using the length and beam waist of our resonator. This distribution is shown as a blue line in Fig. C.1 (a). This box is much smaller than the MOT cloud in all dimensions, so that in our experiment, homogeneous likelihood for the passage of atoms within this volume can be assumed. However it is large in the $x-$ and $y-$directions compared to the cavity waist so that the total electric field outside the box is $< 10^{-3}$ of the total field and of vanishing density, so it can be neglected. To evaluate the coupling distribution for finite integration time, the cooperativity was integrated for the path of atoms falling for a chosen integration time. The green line in Fig. C.1 (a) shows the distribution for an integration time of 10 μs. Even at this short integration time, the distribution is visibly truncated in the high-cooperativity region, since the average cooperativity of the path is always smaller than the peak. As an approximation to the effects of heating, the sinusoidal variation of the cavity field along its axis is replaced by a factor 1/2. Furthermore, coherent scattering processes even heat an atom along this axis at a node of the cavity mode.[20] This is shown by the dashed green line in Fig. C.1 (a), and more dramatic truncation is visible for this line. This will in general be larger than the radial heating, i.e. transversely to the cavity axis, as the transition rate for scattering only along this axis becomes comparable to the free-space scattering rate into all directions when the atom enters this cavity. Given the large sampling volume, most atoms in the

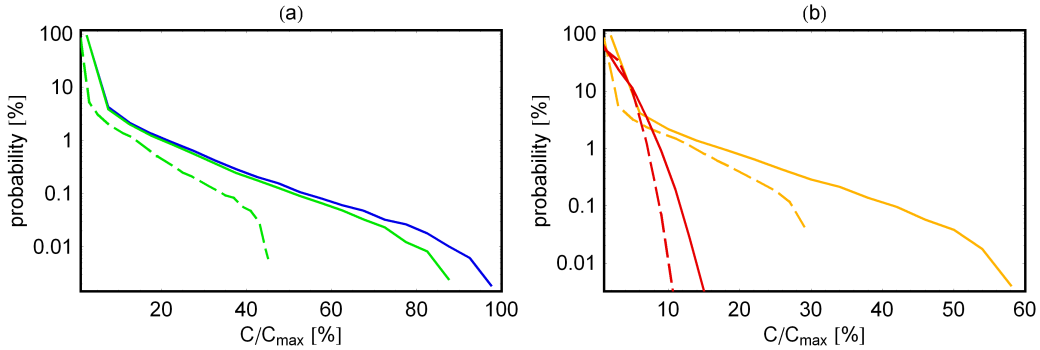

Figure C.1: (a) The distribution of electric field strength within the 'cavity box' (as defined in the text) leads to a probability distribution for the cooperativity of a single atom shown as a blue line. Integrating over 10 μs leads to a decrease in the probability for high cooperativity, as shown by the green line. When heating along the cavity axis is included (dashed green line), the distribution is pushed further downwards still. In (b), the distributions for integration times of 25 μs (orange) and 250 μs (red) are shown, without (solid lines) and with heating (dashed lines).

box will couple weakly to the cavity mode. The average fractional cooperativity for all distributions is equal to the average peak-normalised field intensity, so for these box parameters $\mathrm{C/C}_{max} = 2.18\%$. The total cooperativity of an atom-cavity system with N_A atoms at positions $\vec{r_i}, i = 1...N_A$, is given by

$$C_{tot}(N_A) = \sum_{i=1}^{N_A} \frac{g_{AC}^2(\vec{r_i})}{2\kappa\gamma} \propto \sum_{i=1}^{N_A} \mathcal{E}^2(\vec{r_i}). \tag{C.2}$$

The distribution of these sums was also computed numerically by re-sampling groups of N_A atoms from the distributions above. An example is shown in Fig. C.2, where the peak-normalised distribution of the sums for $N_A = 46$ atoms (for $\bar{C} \times N_A \simeq 1$) is shown without heating in (a) and with heating in (b) for various integration times. From these distributions, it is possible to calculate the distribution of the reflected intensity for a chosen number of atoms in the cavity box. To do this, the distribution of coupling values and the distribution of pumping values due to the Poissonian pump light must be taken into account. For analytical distributions this would be the convolution of the two distributions, while here it is the weighted sum of Poissonians. In other words, if the probability of a cooperativity for a given number of atoms in the cavity box is $p_C(N_A, \tau_{int})$ then the expected reflected-signal distribution on resonance in the weak-pumping limit is

$$p(N) = \sum_{C_i=0}^{N_A C_{max}} p_C(N_A, \tau_{int}) p_n(N, \tau_{int}, J_R^{res}(C_i)) \tag{C.3}$$

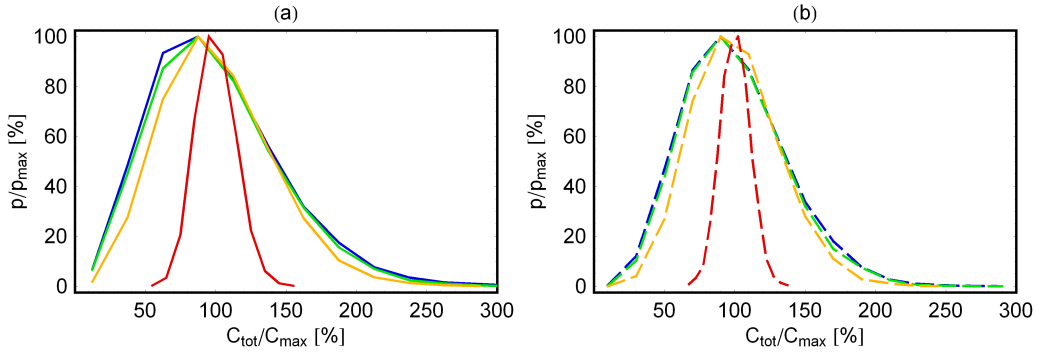

Figure C.2: (a) Cooperativity distribution for 46 atoms in the cavity mode, for integration times of 0 (blue), 10 (green), 25 (orange) and 250 μs (red). In (b), the distributions for the same integration times are shown under the assumption of heating along the cavity axis.

for which p_n and J_R^{res} were given in the previous chapter. Accurate results can of course still be achieved if the cooperativity sum-range is truncated to span most of the distribution. The main feature of this relationship is that for different coupling strengths and atom numbers, radically different count distributions can emerge. To illustrate these effects, a number of contour plots are shown in Figure C.3. In (a) and (b), the probability of detecting a given count rate is shown as a function of the number of atoms in a cavity with the upper and lower limits of our cooperativity range, respectively. In (c), the average atom number in the cavity box is held constant at 1, while the cooperativity is varied. In (d), the average total cooperativity is kept constant at $N_A \times C = 0.88$, so the cooperativity decreases while the atom number increases. This last figure is intended to show that in principle, the distribution of reflected counts can reveal both the atom number and the maximum cooperativity. However, when the atom number is significantly larger than 1, the distributions become effectively indistinguishable. The mean of the distributions also rises rapidly to the level expected for that cooperativity. In all plots, the integration time is neglected and no heating is assumed. Both would lead to a narrowing of the coupling distributions, until only the Poissonian distribution of the light becomes relevant, as made evident by Fig. C.2.

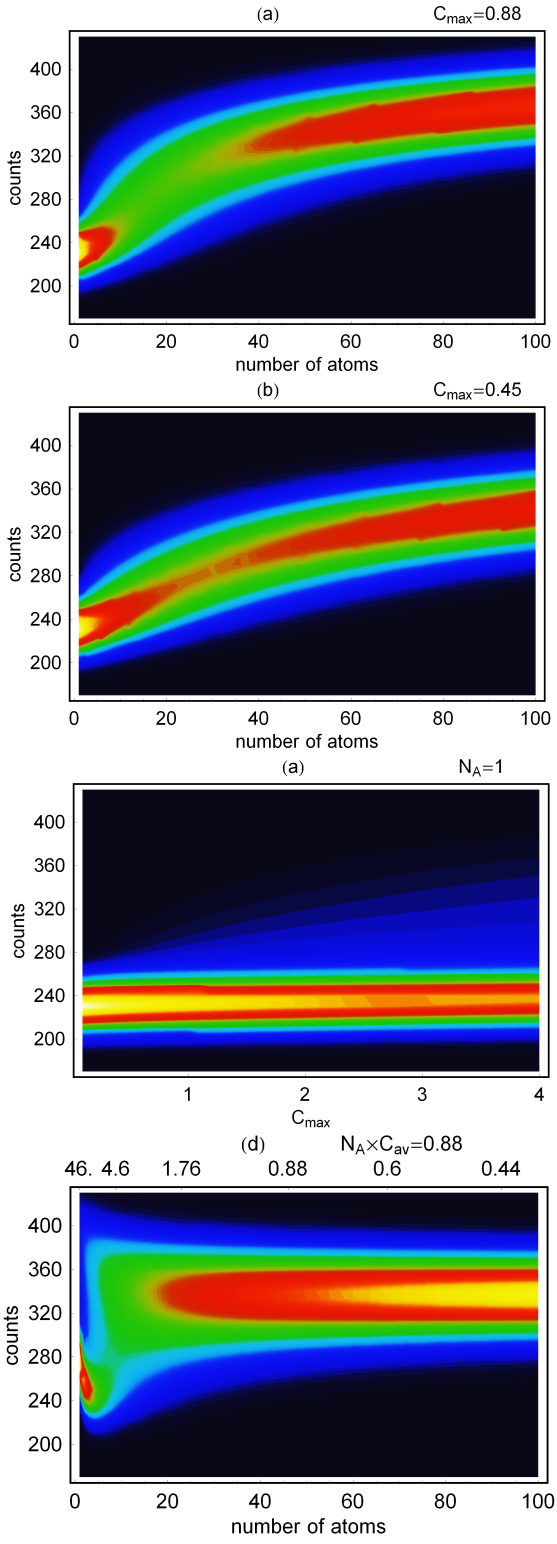

Figure C.3: Distribution of expected counts when varying the following parameters: (a) atom number for $C_{max} = 0.88$; (b) atom number for $C_{max} = 0.45$; (c) C_{max} for $N_A = 1$; atom number for constant $C_{max} \times N_A = 0.88$.